Elaboration and correlation of structure/optical and electrical properties of phase transition oxide materials (VO2, W-doped VO2 and NbO2)

Eduard-Nicolae Sirjita

Eduard-Nicolae Sirjita. Elaboration and correlation of structure/optical and electrical properties of phase transition oxide materials (VO2, W-doped VO2 and NbO2). Electronics. Université de Limoges, 2024. English. NNT : 2024LIMO0005 . tel-04695860

HAL Id: tel-04695860
https://theses.hal.science/tel-04695860

Submitted on 12 Sep 2024

Ph.D. Thesis

University of Limoges
ED653 – Science et Ingénierie (SI)
Laboratory XLIM – UMR CNRS 7252

A thesis submitted to University of Limoges
in partial fulfillment of the requirements of the degree of
Doctor of Philosophy
Information science and engineering

Presented and defended by
Eduard-Nicolae SIRJITA

On the 25th of January, 2024

Elaboration and correlation of structure/optical and electrical properties of phase transition oxide materials (VO_2, W-doped VO_2, NbO_2)

Thesis supervisors:

Alexandre BOULLE, Jean-Christophe ORLIANGES, Aurelian CRUNTEANU

Jury:

Reporters
Mme. Marie-Paule Besland, DR CNRS, IMN, CNRS/ Université de Nantes
M. Vincent Laur, PR, Lab-STICC, Université de Bretagne Occidentale

Examiners
Mme. Aurelie Gentils, CR CNRS, IJCLab, CNRS, Université Paris-Saclay
M. Sebastien Février, PR, XLIM, CNRS/ Université de Limoges
M. Alexandre Boulle, DR CNRS, IRCER, CNRS/ Université de Limoges
M. Aurelian Crunteanu, DR CNRS, XLIM, CNRS/ Université de Limoges

Invited
M. Jean-Christophe Orlianges, MCF, CNRS/ Université de Limoges
M. Richard Mayet, Ingénieur, IRCER, CNRS/ Université de Limoges

To my family.

And here, poor fool, with all my lore I stand no wiser than before.
Johann Wolfgang von Goethe

Acknowledgements

This work would not have been possible without the guidance, support and assistance of many people, too many to mention or who deserve more words than possible in a couple of pages. First and foremost, I would like to express my gratitude to my supervisors Dr. Aurelian Crunteanu, Dr. Alexandre Boulle and Dr. Jean-Christophe Orlianges for their guidance and mentoring. I would like to especially thank Dr. Aurelian Crunteanu for always keeping the doors to his office open, always offering feedback on my work, and always resisting the urge to throw me out of the office when the words coming out of my mouth didn't necessarily make much sense. Dr. Alexandre Boulle I would like to thank for his mentoring and precious insights into the world of XRD and crystallography, and Dr. Jean-Christophe Orlianges for his insights and guidance (and liking me well enough to offer me a job after finishing my doctoral contract). A special thanks to them for promptly answering their emails, a trait which often goes unappreciated.

I would also like to thank Richard Mayet for his help with XRD measurements and fixing my operation mistakes, Cyril Guines for teaching me how to operate in the clean room and, of course, Mrs. Marie-Laure Guillat for having the patience to help me with all the administrative issues. I would also like to thank Maggy Colas and Julie Cornette from IRCER for their help with the Raman measurements. I wish to thank as well Mrs. Marie-Paule Besland for welcoming me in her laboratory in Nantes and helping me with the XPS measurements, which sadly did not make it into the manuscript.

I would also like to thank the other members of the jury Vincent Laur, Aurelie Gentils and Sebastien Février for giving me the honor of judging my work.

My thanks also go out to the National Research Agency, PETACom FET Open H2020 and the Femto-VO_2 Project for funding my research.

I would also like to thank my friends in the open space (Niko, Élisa, Moayad, Ohian, Moha, Benji), the romance languages-speaking community of Limoges (Rosa, Uriol, Christian, Mate, Daniel, Irving, Neus), my friends back home (Goh, Skin, Fron, Angel, Ionut, Vlad), and, of course, my beautiful girlfriend Abigail who even though there is an ocean separating us most of the time, her support has always been with me. Without these people PhD life would've been too dull to continue. If I've missed any names it's because I hate you (I'm joking, it's because I forgot and I am sorry).

A special thanks to Ricardo, Vincent and Nour who have been both the first friends I've made in Limoges, and the best ones. I wish you all the best of luck on whatever dreams you wish to pursue.

Last, but not least, I would like to thank my family for their unconditional love and support throughout my whole life. Without them I would not be where I am today.

Rights

Table of Contents

List of Figures

List of Tables

Introduction

Phase transition materials, more specifically materials that present a metal-to-insulator transition (MIT), are characterized by their ability to undergo an abrupt and reversible change in their physical properties once a critical energy from an external stimulus of high enough intensity is reached. The stimulus can be either electrical, thermal, optical or mechanical in nature and the properties that change are related to the insulating and metallic states. For example, the electrical resistance, the optical transmission or the magnetic properties. By combining these causes and effects in different ways, a plethora of applications utilizing phase transition materials have emerged, ranging from active elements in thermochromic applications to electro-optical switches or neuromorphic computing devices. Indeed, a multitude of cutting-edge technologies that are critical in today's scientific and industrial environments can employ MIT materials. For example, the field of thermochromics that is essential in reducing day-to-day energy consumption of society by keeping the indoors a cooler environment. Reconfigurable antennas, particularly those operating in the high-frequency range, hold significant importance in addressing the current challenges related to bandwidth and available communication frequency bands in the field of telecommunications. Neuromorphic, power efficient, computing based on MIT materials has also triggered increased attraction in the recent years due to the vast new field of applications that came with the artificial intelligence algorithms.

Considering the aforementioned benefits and practical applications of MIT-capable materials, the present manuscript will focus on the following compounds and their extending their possible applications:

i) VO_2, as an archetypical MIT material, due to its close-to-room temperature transition temperature (340K) and its high electrical resistivity ratio between the metal and insulating states.

ii) Tungsten doped VO_2 that allows us to modulate the transition characteristics of pure VO_2 and, in particular, reduce the transition temperature close to room temperature.

iii) NbO_2, which, due to its higher phase transition temperature (~1080K), covers some of VO_2's weaker spots, e.g. operation at high temperatures.

The theoretical aspects and applications of these materials will be covered in **Chapter I** of this thesis, as well as some necessary background information on the epitaxial growth and doping of the materials.

Of course, an important step in connecting the laboratory research to the industrial applications is using a deposition process that is easily scaled up, and in particular being capable of covering large area substrates, while being relatively inexpensive and have a high reproducibility. To this end, reactive DC magnetron sputtering fulfills most of the mentioned conditions and is the main deposition method used during this research.

Chapter II will present the theoretical and practical aspects of the thin film growth by reactive DC magnetron sputtering, as well as the techniques used to characterize the properties and the structure and the obtained films. **Chapter III** is focused on the deposition of VO_2 films on c-sapphire substrates and understanding the influence of the growth and annealing parameters on the electrical, structural and optical parameters of the films. This information is useful for obtaining high quality VO_2 films as a base for integrating them in future devices. **Chapter IV** focuses on tungsten doped VO_2 fabrication using the experience from Chapter III, and incorporating them in simple devices such as electrically-activated large area THz amplitude modulators, a much-needed instrument in THz communication and more. **Chapter IV** focuses on tungsten doped VO_2 fabrication using the experience from Chapter III, and incorporating them in simple devices such as electrically-activated large area THz amplitude modulators, a much-needed instrument in THz communication and more. **Chapter V** is dedicated to NbO_2, a material that lacks much needed research, thin film fabrication and characterization of the thermally and electrically induced transition, with further focus on exploring the electrically induced periodic oscillations. The manuscript will be concluded with a chapter dedicated to exploring further concepts and application perspectives integrating these materials.

Chapter I. General properties of phase transition metal oxides and epitaxial growth

Phase change materials (PCMs) is a general term used for a large group of materials that have the ability to undergo a phase transition between two or more solid states. In many functional devices however, it is of high interest to have a phase change coupled with a major transition of a specific physical property, like for instance the conductivity, as in the case of a metal to insulator transition (MIT). Phase transition materials (PTMs) is a more specific term, that will be used for the purpose of this manuscript, for those PCMs that have a volatile transition between the metallic and insulating states, i.e. the material transitions back to its initial state when the stimulus that triggered the transition is removed. PTMs have been a research topic for decades and, to better integrate the materials into functional devices by reaching a higher understanding of the physical phenomenon underlying the MIT, both experimental and theoretical efforts have been made. Depending on the material in question the MIT can arise either from electron-electron interactions (Mott transition), electron-phonon interactions (Peierls distortion), disorder-induced localizations (Anderson localization), or a combination of these mechanisms [1]. The MIT can be triggered by various external stimuli once a threshold value is reached. These stimuli can be thermal, electrical, optical, or mechanical [2]. Of course, transitioning from an insulator to a metal implies not only changes in resistivity, but also in the optical, mechanical, and magnetic properties.

Materials exhibiting an MIT span a large range of transition temperatures, as indicated in Figure 1, the majority of these transitions occur below room temperature (RT), with a handful around RT, and some above 100°C. As a result, MIT materials may be employed in a multitude of applications operating over a wide temperature range. A quintessential representative for this class of materials is vanadium dioxide (VO_2) due to its relatively close to room temperature transition (~68°C) and its large resistivity variation from the insulating to the metallic state (around five orders of magnitude). Since the initial report on the material's MIT properties by Morin *et al.* [3], VO_2 has been the topic of intense research efforts. The low transition temperature of VO_2 which can be advantageous in some applications, can hinder electronic applications due to Joule heating resulting in undesirable heat-induced errors in circuit operation. Industry standards also dictate stability to temperatures above the transition temperature of VO_2. As such, in parallel to VO_2, different MIT-capable materials have been investigated. Niobium dioxide (NbO_2), an oxide with a similar crystalline structure, has a transition at a much higher temperature of ~1080K (although sources vary) [4] making it more appealing to electronic applications. Its high temperature transition, however, makes it difficult to properly characterize its electrical and optical properties, NbO_2 has thus received less attention in comparison with VO_2.

Approaches used to grow MIT materials have included both physical and chemical methods including, among others, pulsed laser deposition (PLD), sol-gel deposition, magnetron sputtering, e-beam evaporation or molecular beam epitaxy (MBE). A review encompassing the approaches of growing VO_2 was done by Shi *et al.* [5]. Among these, magnetron sputtering stands out due to the advantages of being a semi-industrial method able to grow films over large surfaces at relatively low costs. This method also possesses a simplicity of deposition, high deposition rate and a high repeatability of the experiments. In order to directly achieve metal oxide materials two methods can be used: i. deposition from a metal-oxide target (usually using RF magnetron sputtering) or ii. adding oxygen to the sputtering process (reactive DC magnetron sputtering method) when using a metallic target. Sputtering from a metal oxide (or insulating materials in general) leads to greatly reduced sputtering rates when compared to metallic targets, even when using the RF sputtering technique, a method which is additionally more power intensive than DC sputtering, hence leading to higher operating costs. Furthermore, these kinds of metal-oxide targets are usually done *in-house* which adds a new layer of complexity, or come with a higher cost. Thus, sputtering in an oxygen atmosphere from a metallic target is preferable as it gives the user more control over the oxygen content of the samples without giving up the sputtering rate. Given these arguments, this thesis will employ reactive DC magnetron sputtering from metallic targets in O_2/ Ar atmosphere in order to achieve vanadium and niobium dioxide thin films.

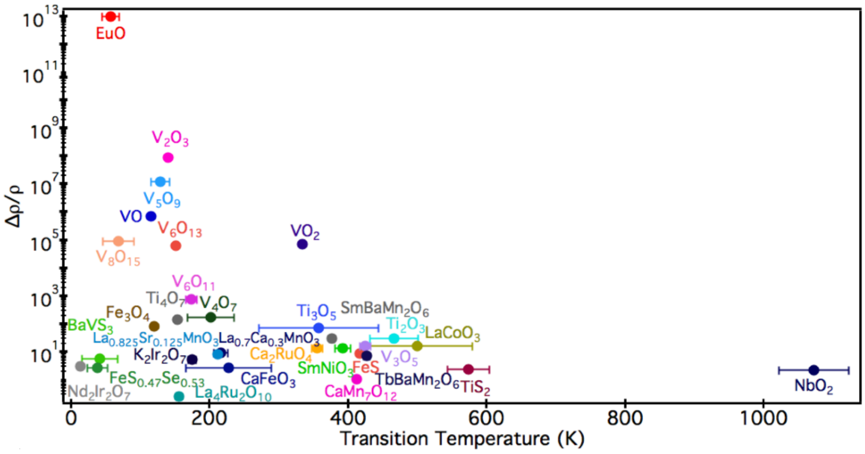

Figure 1. Relative change of electrical resistivity as a function of the transition temperature of MIT materials. [6]

I.1. The metal-to-insulator transition hysteresis

A key feature of the MIT is created by the slight offset between the energy needed for the material to transition to the metallic state and the one needed to transition back to the insulating state. This offset creates a well-known hysteresis which is present in the measurement of multiple types of parameters, such as in the measurement of the optical or electrical parameters. The shape of this hysteresis curve is important in describing the PTMs. Figure 2, for example, represents a typical hysteresis curve of the resistance of a VO_2 film, done while increasing, and then decreasing the temperature of the film. From these measurements, important parameters such as the transition temperature and the hysteresis and transition widths can be obtained. In order to quantitatively extract them from the curves, the first and second order derivatives need to be calculated. The metal-to-insulator transition temperature (T_{MIT}) is defined as middle point of the MIT and corresponds to the average between the temperatures of the inflection points of the resistivity. Those are given by the minima of the first derivative and are denoted T_{up} and T_{down}, for increasing and decreasing temperature, respectively. The hysteresis width (ΔH) is the difference between T_{up} and T_{down}. We use the minima and maxima of the second order derivative to evaluate the overall width of the transition, ΔT. Defining T'_{up} and T'_{down} as the high temperature and the low temperature inflection points of the first derivative, and the transition width ΔT, or the whole temperature range where the transition takes place, is defined as $T'_{up} - T'_{down}$. These values are summarized in Figure 2 below. Occasionally, a curve fitting process with a sigmoidal-type fit becomes necessary to diminish the impact of experimental measurement-induced noise, which could lead to unreliable results.

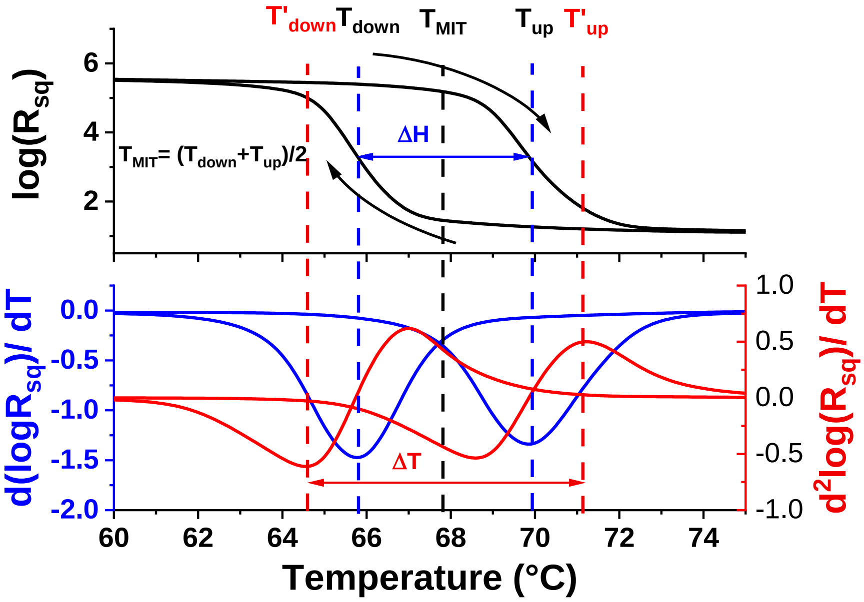

Figure 2. A typical high-quality VO_2 on c-sapphire sample's sheet resistance hysteresis curve and the related first- and second-order derivatives. Top image is the interpolated and smoothed experimental curves.

I.2. Negative differential resistance

Negative Differential Resistance (NDR) is a phenomenon observed in certain non-linear electronic devices where, contrary to the behavior of an ohmic resistance, the current decreases (current sweep/ current control) as the voltage increases, or vice versa (voltage sweep/ voltage-control). This counterintuitive effect has significant implications and applications in various fields, such as relaxation oscillators for neuromorphic computing [7–9]., amplifiers [10], or memristors [11]. NDRs can take two forms: continuous (S-shaped), characterized by a gradual decrease in resistance, or discontinuous (snapback), characterized by a large jump and a hysteretic behavior. In PTMs, this type of NDR is associated with the onset of the MIT. Due to the nature of this transition, these NDRs typically exhibit a snapback behavior and display hysteresis, especially large during voltage control.

During a current-sweep of a VO_2 film the NDR region is usually seen to arise between two regions of instability, thus looks as a combined snap-back and S shaped NDR [7,12]. An example can be seen in Figure 3. Based on a review of existing literature, a direct explanation for this phenomenon has not been identified. It might however be linked to the formation of continuous conductive clusters at a threshold temperature/ current after the NDR [7,13].

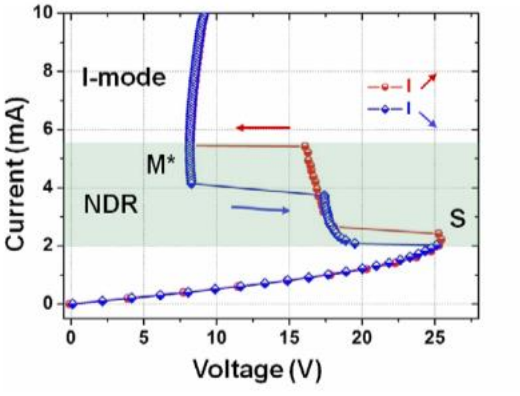

Figure 3. VO_2 NDR showing an S-shape between two regions of instability. [12]

In the case of NbO_2, it was reported that the current-voltage curves exhibit two distinct NDR regions. In NbO_2, especially amorphous NbO_2, one of them is triggered at an equivalent temperature of ~1000K, which was linked to the MIT and exhibits a jump in the current/ voltage (snapback mechanism). The other NDR appears to precede the MIT, exhibits an S-shape NDR and is triggered at an equivalent temperature of ~400K [14]. This has led researchers to describe this S-shape NDR as being initiated by a Joule heating driven thermal runway caused by a non-linear Poole-Frenkel (PF) mechanism [14,15]. Basically, as the current is increased through the circuit, the temperature also increases from the Joule heating effect, which in turn lowers the conductance, which produces further increase in temperature. At a critical current, this positive feedback results in a negative differential resistance. The PF effect is a phenomenon that is often observed in insulating materials. Despite being insulting, these materials present random thermal fluctuations that will give electrons enough energy in order to jump in the conduction bands of the material. This free electron however exists for a short amount of time before it transitions back to the valence bans. The PF effect describes how in a large electric field the thermal requirements for this electron jump is lowered by the pull of the electric field.

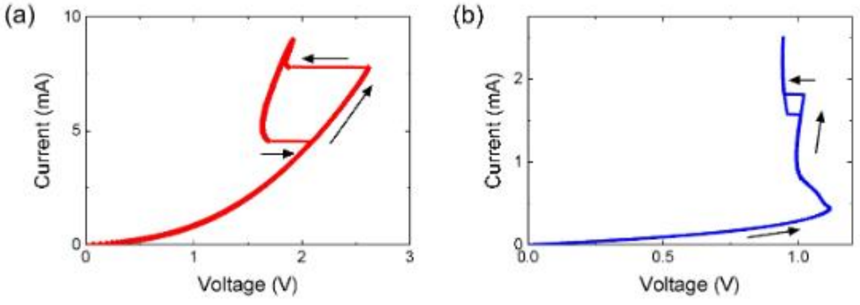

Figure 4. Current-controlled switching in NbO_2 a) NDR related to the MIT and b) two NDRs zones related to thermal runway effect and MIT. [16]

I.3. Transition mechanisms of VO_2 and NbO_2

In the classical band theory, the metallic or insulating behavior of materials stems from the filling of the energy bands. A semiconductor is thus characterized by a gap between the valence band and the conduction band, with an empty conduction band at the Fermi level. An insulator is a semiconductor with a very large gap. In a metal the conduction band is partly filled. Although most materials' behavior may be predicted using this model, it doesn't explain why some materials, mostly transition metal compounds, are still weak conductors or even insulators [17,18]. In the following section we will briefly discuss the mechanisms of phase transitions that regard our choice materials.

I.3.1. Mott transition

Within a hopping conduction mechanism where one electron jumps from one site to another, a Coulomb repulsion between two neighboring electrons of same d orbital can localize the charges leading to an insulating behavior. “Mott insulators” is the name of this class of materials where the conductivity is limited by electron correlation, a phenomenon first described by N. Mott [19] and named in his honor. For the material to transition from an insulating state to a metallic state, the free electron density needs to surpass a theoretical threshold, which is necessary to effectively screen the Coulomb interactions [20,21].

A theoretical description of the Mott transition can be given by a simplified Hubbard model for only a single band of delocalized electrons [22,23] in which the Hamiltonian is described as:

$$H = \sum_{i,j,\sigma} t_{ij} c^{*}_{i\sigma}\, c_{i\sigma} + U \sum_{i} n_{i\uparrow} n_{i\downarrow} \tag{1}$$

Where U is the intra-atomic interaction energy (i.e. the Coulomb repulsion energy), t_{ij} is the probability for an electron to hop from site i to site j, $n_{i\sigma} = c^{*}_{i\sigma} c_{i\sigma}$ represents the electron number operator for site i and spin σ, and $c^{*}_{i\sigma} c_{i\sigma}$ represent the annihilation and creation operators of electrons at site i. Simply put, the first part of the equation is related to a metallic behavior and the second part relates to an insulating one, thus it is expected that a Mott transition would happen once the energy of the system is larger than the one of the Coulomb repulsions.

The ratio U/t (or U/W where W is the bandwidth) is an important parameter as it can describe when the MIT will occur. For example, increasing the external pressure may reduce the lattice constant, thus the bandwidth will increase until a critical value of U when the MIT will take place. This is schematically represented in Figure 5 and is called bandwidth control MIT.

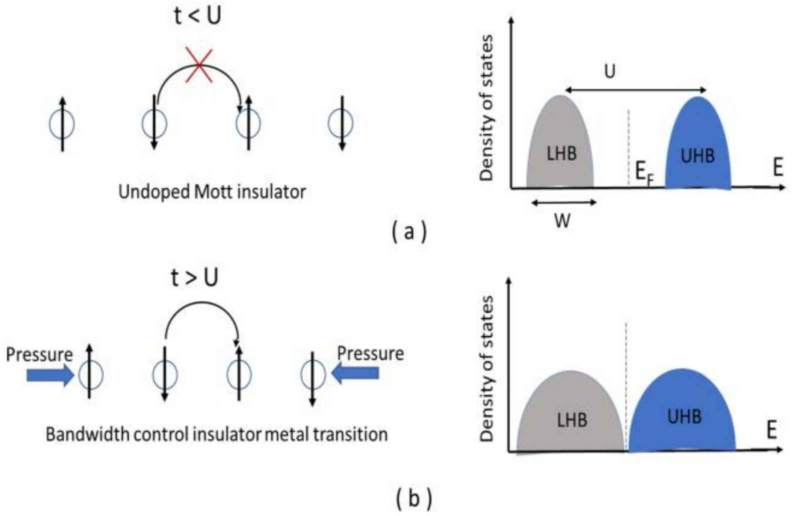

Figure 5. Schematic representation of a) an intrinsic Mott insulator b) MIT through bandwidth control. [24]

The interaction energy U between electrons can also be altered by adding or removing electrons, thus reducing the Coulomb repulsion energy. This is achieved through the filling-control MIT transition, which effectively screens electron-electron interactions. This method is represented in Figure 6.

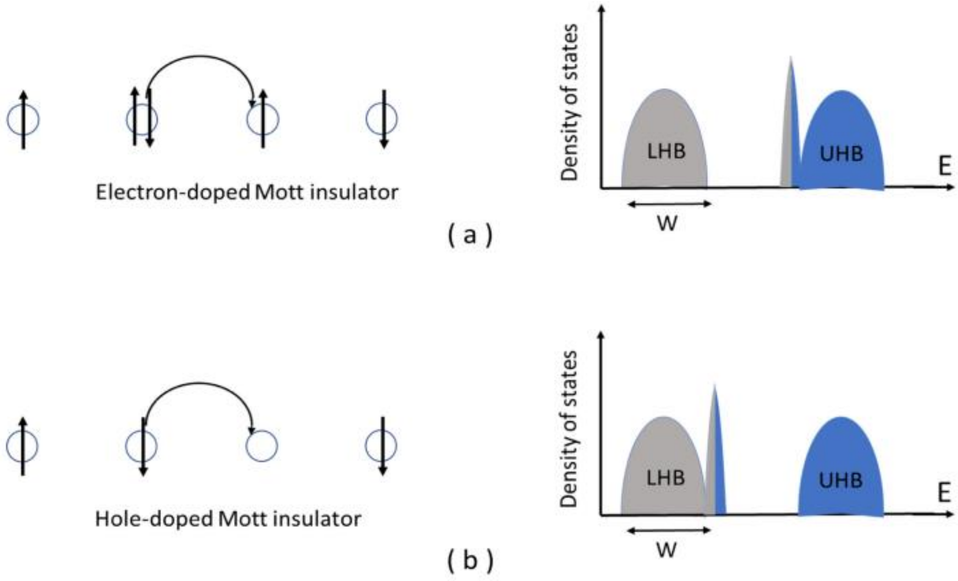

Figure 6. Schematic representation of filling control MIT a) through electron-doping and b) through hole doping. [24]

In the Hubbard model only the 1s orbital is considered for simplicity, while in reality transition metal oxides have partially filled 3d/4d orbitals, however the model gives a qualitative representation of the Mott transition.

I.3.2. Peierls transition

A Peierls transition is described by the interaction between the phonons and the electrons. This transition mechanism is named so as it was first proposed by R. Peierls [25]. If we imagine a 1D periodic lattice with N ions spaced apart by a distance $\boldsymbol{a}$**,** with a total length of $\boldsymbol{L}$, then the energy bands may take the shape of Figure 7 a), where the bandgaps open at the end of the Brillouin zone at $\boldsymbol{k} = \boldsymbol{\pi}/\boldsymbol{a}$, where k is the wavevector. If monovalent atoms are used, the lowest band is only half full, meaning that there are empty positions that electrons can occupy, thus, resulting in a metallic behavior. Now, if we introduce a small distortion $\boldsymbol{\delta}$ and the atoms move closer to each other in a process called dimerization, the periodicity would double to $\boldsymbol{2a}$. This distortion will modify the energy curve E(k) and now the gaps open at $\boldsymbol{k} = \boldsymbol{\pi}/\boldsymbol{2a}$. If this gap opens near the Fermi level, then the lowest band will become completely filled and the upper one will be emptied, giving rise to an insulating state.

Peierls also showed that for small displacements the reduction in the electronic energy of the system is proportional to $-\delta^2\log\delta$ which would finally lead to the 1D atomic chain being unstable even at 0K [26].

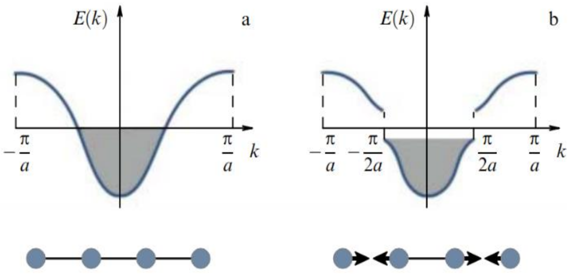

Figure 7. A Peierls transition from an a) undistorted to a b) distorted atom chain, with a bandgap opening at ±k. [27]

I.4. Vanadium dioxide

The first to describe the MIT in VO_2 was F.J. Morin in 1957 [3] and the material has since attracted ever increasing interest because of the large magnitude of the resistivity change (more than five orders) and a T_{MIT} relatively close to room temperature. More precisely, VO_2 has a semiconductor-metal transition, however the term “metal-insulator” is commonly used by the scientific community.

In order to study or exploit the MIT of VO_2, the material has been obtained with a multitude of techniques [5], such as DC-[28] and RF-[29] magnetron sputtering, e-beam reactive evaporation [30], pulsed laser deposition [31], molecular beam epitaxy [32], or sol-gel techniques [33]. Besides its synthesis in the form of nanofilms, VO_2 has also been produced as multiple types of nanostructures such as nanowires [34] and nanowire arrays [35], nanonets [36], nanobelts [37], nanotubes [38] or nanobeams [39].

In VO_2, the change in electrical properties is accompanied by a structural phase transition (SPT) between a low-temperature monoclinic phase and a high-temperature rutile phase, which has led to a debate around the nature of the transition. The question, that is under debate even today (as many theoretical and experimental reports arriving at different conclusions), is if the transition is driven by an electron correlation transition (Mott transition scenario) or is it the result of lattice distortions (Peierls transition scenario)? For example, the insulating phase has been regarded as a Peierls-assisted Mott insulator [40] or, reversely, a correlation-assisted Peierls insulator [41]. Even more complicated scenarios arrive if one additionally considers the intermediary phases between the low and high temperature monoclinic and rutile phases [42].

Seemingly, more and more publications discuss how the two scenarios interact in a cooperatively significant way [31,43], although it’s important to note that experimentally and theoretically, the transitions have been decorrelated. Generally it is accepted that among the external stimuli used for triggering the MIT, the main mode of activation is thermal, and that the electric activation is a form of thermal activation induced by Joule heating from the applied currents [44]. The discussion about photoinduced transitions however remains even more so controversial, especially with the experimental difficulties they pose. In their paper on the optically induced transition, Morrison et al. [45] suggested the existence of two different laser fluence threshold values for the SPT and the MIT. They proposed the presence of a metastable mM phase that retains the monoclinic structure of the material but exhibits metallic behavior. These threshold measurements, however, seem to be affected by heat accumulating during the pump-probe measurements, making accurate determination a challenge [46]. Other theoretical simulations and experiments have proposed that these thresholds are actually the same, and that a metallic monoclinic phase would exist only transiently [47,48]. What is more, the crystallinity, strain, thickness and form of VO_2, whether it's freestanding or patterned, affect the experimental results [45,46,48], thus it is difficult to state on which mechanism has priority when a multitude of factors influences the measurements on the transition mechanism.

I.4.1. Crystal structure of VO_2

Vanadium, classified as a transition metal, exhibits multiple oxidation states (2+, 3+, 4+, 5+) [49]. Upon its reaction with oxygen, various oxides of vanadium are formed, as depicted in the phase diagram in Figure 8. Deviations from the VO_2 stoichiometry leads to two classes of vanadium oxides called Magnéli phases ($V_nO_{2n-1} = VO_{2-1/n}$) and Wadsley phases ($V_nO_{2n+1} = VO_{2+1/n}$) [2]. Magnéli phases are considered to go from V_2O_3 to VO_2(R) and the Wadsley phases from VO_2(B) to V_2O_5 [50]. Most of the existing V-O phases fall in the Magnéli group and within this group the majority of phases present an MIT behavior [49], while in the case of the Wadsley phases, much lower in number, only one does, namely V_6O_{13} [51]. In total, however, most of vanadium oxides have an MIT, with only some of them being either fully insulating or fully metallic. Among the ones that do display an MIT, VO_2 has the highest resistivity ratio, with the T_{MIT} above 0°C.

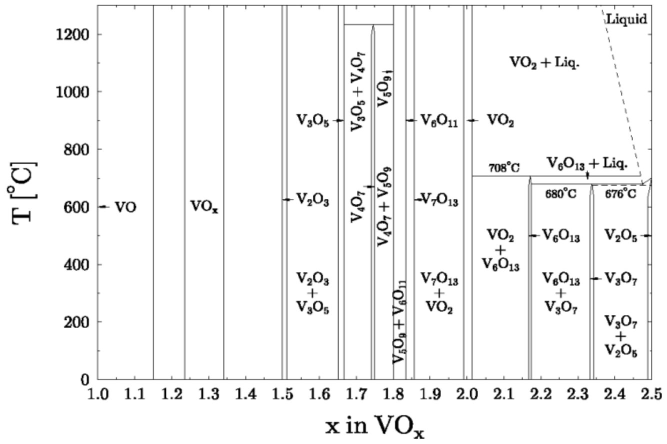

Figure 8. VOx phases. [50]

VO_2 itself has many known phases with different crystalline structures such as VO_2(A), VO_2(B), VO_2(C) VO_2(M_1), VO2(M_2), VO_2(T) VO_2(R), VO_2(D), VO_2(P) [29,52–54] the majority of them being either metastable phases or lacking enough study in order to integrate them in devices. From this list, the low temperature insulating VO_2(M_1) and the high temperature metallic VO_2(R) have the received the most study as they present a first order reversible transformation between them, making these phases interesting for a large number of applications.

The high temperature R phase of VO_2 is of tetragonal symmetry and exhibits a rutile structure, with space group. $P4_2/mnm$. In this structure the V metal atoms are located at (0,0,0) and ($\frac{1}{2}$, $\frac{1}{2}$, $\frac{1}{2}$) and the oxygen ions at $(u, u, 0)$ and $\pm\left(\frac{1}{2}+u, \frac{1}{2}-u, \frac{1}{2}\right)$. The lattice constants and the internal oxygen parameter u were determined experimentally by McWhan *et al.* [55] to be $a_R = 4.5546Å$, $c_R = 2.8514Å$ and $u = 0.3001$ respectively, with other researchers arriving at similar values [56,57].

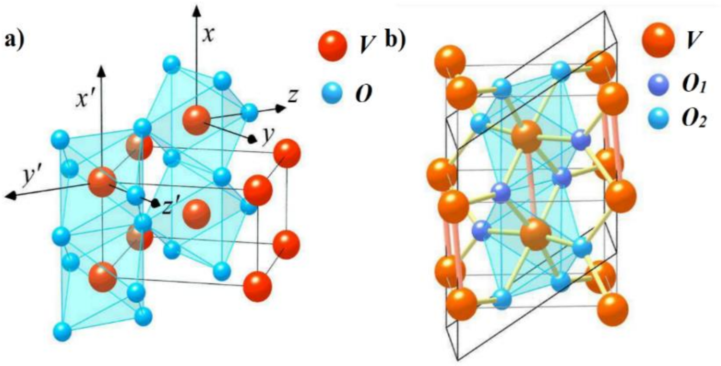

Figure 9. a) Rutile and b) monoclinic structures of VO_2, based on [58].

A decrease of the temperature below the critical temperature of 340K leads to a dimerization between the V atoms along the c-direction of the rutile structure, which is combined with a zig-zag like pattern appearing between the V-V atoms due to dimer rotation around the same axis. A doubling of the unit cell is a result of these modifications, with the lattice constants $a = 5.75, b = 4.53, c = 3.48$ and $\beta = 122.6°$ [59]. The corresponding space group of this monoclinic phase is $P2_1/c$.

Beside the R and M_1 structures, two metastable intermediary phases have been reported which can be stabilized with strain or temperature, according to Figure 10. The monoclinic M_2 phase belongs to the space group C2/m and behaves as an insulator. M_2 has two types of vanadium chains, one where the V atoms are paired with no tilting along the rutile c axis, and one where the V atoms do not pair, but form zig-zag chains perpendicular to the c axis [60]. The triclinic T phase is intermediary between M1 and M_2 and is also insulating, with the M_2 pairs tilted towards their M_1 configurations, and the zig-zag chains gradually dimerizing with lowering the temperature [60].

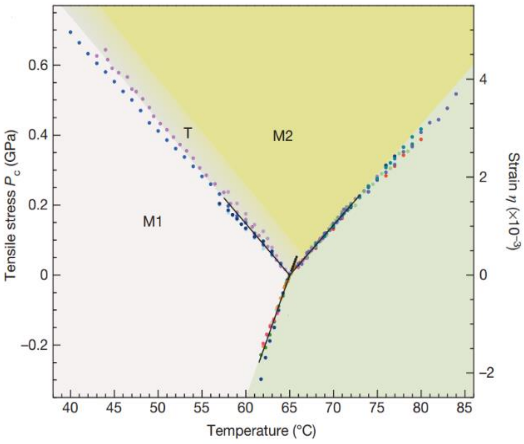

Figure 10. Stress-temperature phase diagram of VO_2. [61]

I.4.2. Band diagram of VO_2

According to J. Goodenough's model [62], which was the first one to describe the electronic structure of VO_2 and whose description has remained mostly consistent with modern theories, in the insulating state the V 3d orbital splits into a twofold degenerate states of e_g symmetry and a threefold degenerate states of t_{2g} symmetry (the letter g in the subscript come from the German word “gerade”, signifying an even symmetry, while t and e stands for triply and doubly degenerate energy levels respectively). The t_{2g} orbitals further splits into two d_{π} orbitals and one $d_{\|}$ orbital, and the e_g orbitals into two d_{σ} orbitals. σ, σ^* bonding and antibonding bands are formed by the σ type bonding between the $2p_{\sigma}$ and the $3d_{\sigma}$ orbitals from the oxygen and vanadium ions. Finally, π bonding and π* antibonding bands are formed by the covalent mixing of a single p_{π} orbital and two $3d_{\pi}$ orbitals. This can be better visualized in Figure 11.

In the conducting state, the $d_{\|}$ and π* orbitals are partly occupied by one electron per V atom and overlap at the Fermi level. In his paper J. Goodenough proposed that the driving mechanism of the MIT is the anti-ferroelectric displacement of the V ions when cooling down under the T_{MIT}, this would increase the p-d hybridization, up-shift the π* level and leave the $d_{\|}$ bands half filled. Finally, the formation of V-V dimers, more energetically favorable for half-filled $d_{\|}$ bands, would double the c_R axis and split the $d_{\|}$ level into an occupied bonding $d_{\|}$ and an empty anti-bonding $d_{\|}^*$ level that decreases the Fermi energy below the π* band. These effects yield a band gap of 0.6 eV.

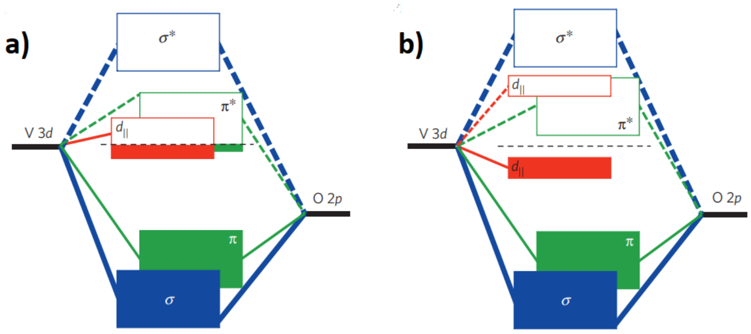

Figure 11. Schematic of the VO_2 band structure in the a) metallic and b) insulating states. [63]

I.4.3. Microstructural parameters affecting the transition

Alongside the controlled means of manipulating the MIT parameters such as strain or doping as will be discussed later, there are several microstructural parameters that may inadvertently affect the transition, which are discussed below.

The transition from the insulating to the metallic phase is said to be heterogenous and to proceed in a non-uniform fashion, relying on structural defects as the source of nucleation sites [64]. Klimov *et al.* [65] proposed that each grain exhibits its own hysteresis loop with parameters controlled by the grain size, strain, etc., thus, a larger number of grains would result in a wider temperature spread. In their proposed mechanism, the formation and growth of a metallic nucleus within an insulating state remains stable if the temperature deviates from the phase equilibrium temperature by a value that is inversely proportional to the square root of the grain diameter. This behavior is also observed during the transition back to the insulating phase. In their paper they also discuss how grain size distributions might affect the shape of the hysteresis, resulting in hysteresis curves with multiple inflection points.

Another type of defects that may influence the transition are point defects, such as oxygen vacancies or interstitials. These defects influence the charge localization, thus affecting the band structure. Indeed, an oxygen interstitial may add two-hole carriers that decrease the insulating resistance, while an oxygen vacancy may add two electrons that ultimately narrow the band gap, also reducing the resistance in the insulating state [66]. As point defects are also nucleation sites for the transformation, they will promote the onset and progress of the transformation.

According to Narayan *et al.* [67], who proposed one of the more complete models of defect influence on the transition, the driving force of the phase transition is:

$$\Delta G_r = \Delta T_r \Delta S_0 \tag{2}$$

Where ΔG_r is the change in the Gibbs free energy associated with the phase transition, ΔT_r is the deviation from the equilibrium transition temperature, and ΔS_0 is the change in entropy between the two phases. This requires a non-zero ΔT_r which is directly related to the ΔH, thus a hysteresis cannot be avoided.

The transition width in their model is defined by:

$$\Delta T = C_t \rho_d \tag{3}$$

Where C_t is a constant and ρ_d is the defect density. The grain boundary defects normally are less important than the other defects (point defects), but play a major role when the grain size is reduced to the nanoscale, increasing the ΔT. The total amplitude of the transition (e.g. the insulating/ metallic resistance ratio) is as well dependent on the defect content, being inversely proportional to it.

The width of the transition is related to the critical size of the stable nuclei and the interfacial energy, that is, as the interfacial energy increases, so does the hysteresis width. This interfacial energy is directly related to the grain boundaries (density and orientation). For example, a polycrystalline film with random orientation will have a large ΔH.

Narayan's model predicts that the hysteresis curve for all types of microstructures: i. high-quality films (i.e. mono-crystalline) with grains separated by low angles (less than 1°) will exhibit large amplitudes, narrow transitions controlled by the defect content and hysteresis widths kept to a minimum through the low angle boundaries ii. textured polycrystalline films with small-angle boundaries will have small transition widths, while the hysteresis width will increase with the misorientation of these boundaries iii. randomly oriented polycrystalline films with large-angle random boundaries will experience an increase in transition width with decreasing grain size, while the hysteresis width will remain constant or increase with grain boundary misorientation, and iv. amorphous films will exhibit a large transition width but a very small hysteresis width due to the absence of grain boundaries, allowing for symmetric propagation during cooling.

Narayan’s model has so far been well corroborated by a number of works, for example Jian et al. [68] in their randomly oriented polycrystalline VO_2 films fabricated on amorphous glass substrates showed that ΔT increases well with increasing grain sizes, while the ΔH remains mostly constant.

Aliev *et al.* [69], in their research, described how at high thicknesses the transversal grain size dictates the transition temperatures, while at low enough thicknesses the deviation from the phase equilibrium temperature required for the phase transition to take place is only dependent on the thickness.

I.4.4. Applications of VO_2

Owing to its MIT and possibility of activation by optical, thermal, mechanical and electrical external excitations, VO_2 has found a place as an active layer in a large number of applications. A well-known field were VO_2 is a popular candidate is called thermochromics, which use phase transition materials as variable optical transmission elements. Thermochromic materials are the backbone of the so called “smart windows” which change the intensity of the transmitted light as an “automatic” response to the change in the local temperature. Indeed, VO_2’s property to regulate the sun’s radiation after the MIT, mostly in the IR spectrum, has proven to be useful as a means to keep indoor temperatures lower during the hot summer days, resulting in lower electricity consumption associated with air conditioning [70]. However, VO_2’s transition temperature is slightly higher than what would be acceptable and needs to be reduced, ideally to around room temperature. An efficient method to achieve this is by doping the VO_2 with different atoms, which will be more deeply described in chapter I.6. One of the most popular dopants is tungsten (W), the $W{:}VO_2$ solid solutions being currently promising candidates for thermochromic layers [71]. Other applications that exploit VO_2’s control over the electromagnetic spectrum (through the modification of its optical or electrical properties) are modulators, switches and polarizers devices in the infrared, microwaves or the terahertz domains [72–74]. The field of THz waves properties control is especially interesting as the technologies for this domain are still not as advanced as the ones for the adjacent domains of millimeter waves and infrared [75].

By applying etching techniques [76] to create various patters, VO_2 can also be used in the form of metamaterials. Metamaterials based devices integrating VO_2 films have attracted significant attention in the last decade due to their ability to efficiently control electromagnetic waves and to possess exotic behaviors that aren’t found in nature, such as negative refractive index. In short, metamaterials are artificial materials with subwavelength dimensions arranged in periodic patterns that are specifically designed to interact with and modulate electromagnetic radiation, heat or sound. Lu *et al.* [75] have recently reported a review encompassing different configurations in which VO_2 can be used to manipulate the electromagnetic properties of THz waves like the amplitude, phase, polarization and beam propagation direction.

Other applications of VO_2 include thermoelectric generation devices [77], IR camouflage and thermal regulation [78,79], micro actuators [80], gas and thermal sensors [81,82], Mott-field effect transistors [83], or infrared shielding layers [84]. Comprehensive reviews of VO_2’s applications have been reported by Liu *et al.* [2] and Shi *et al.* [5]. Another review that encompasses VO_2 and other V-O phases’ applications was recently published by Hu *et al.* [85].

VO_2 has a long list of applications when considering the optical, electrical and thermal activation of the material. The list more than doubles when one considers combining these different stimuli and creating multi-stimuli type devices. These applications have been effectively summarized by Bhuhpathi *et al.* [86] and displayed in Figure 12.

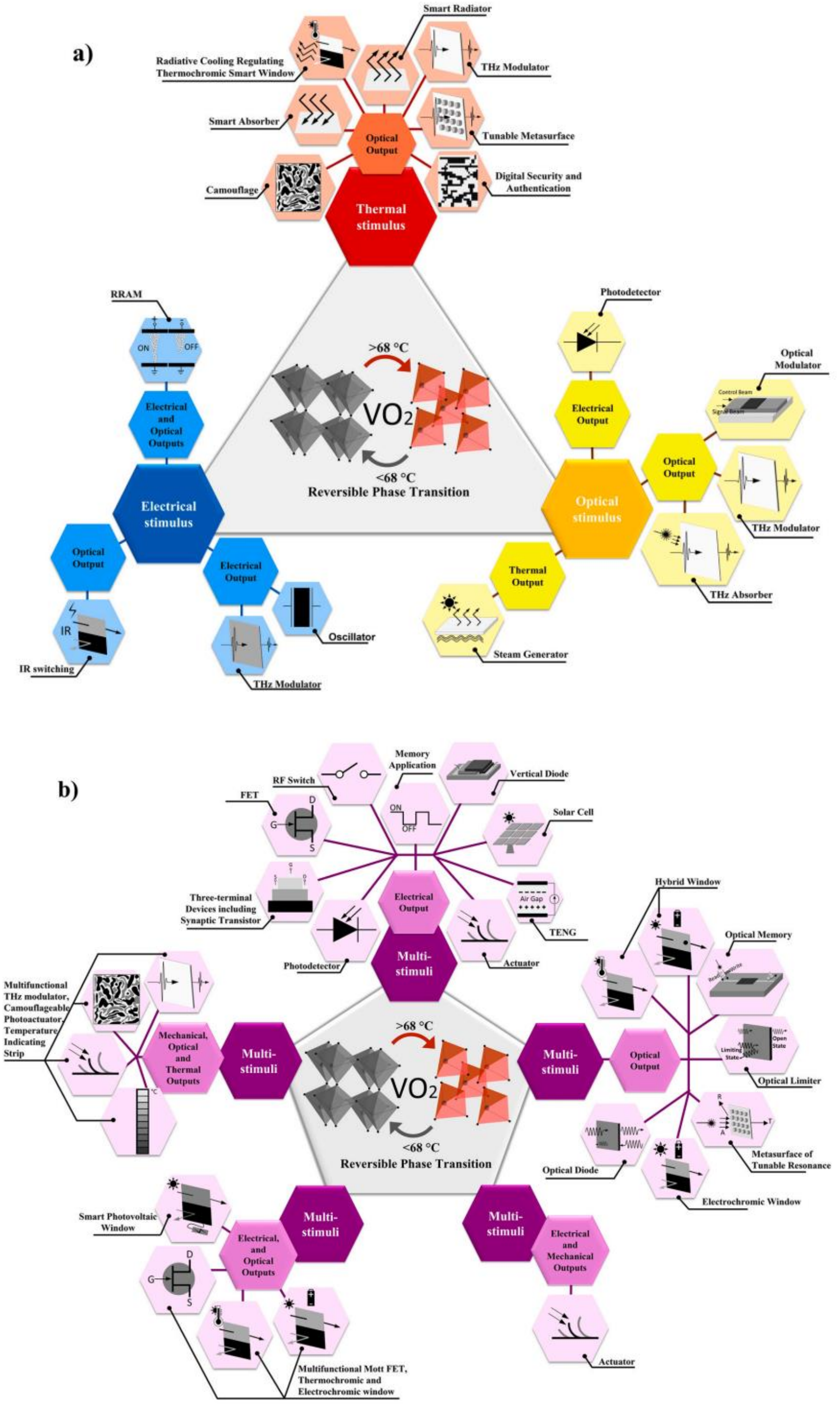

Figure 12. VO_2-based devices controlled by a) single-stimulus (thermal, optical, electrical) and b) multi-stimuli. [86]

I.5. Niobium dioxide

As mentioned previously, NbO_2 has a much higher transition temperature than VO_2 (and all the other PTM's, see Figure 1), at around 1080K, or ~800°C, but also a lower resistivity ratio between the high and low temperature states [6]. Another key difference between VO_2 and NbO_2 is that while in the former the debate about the driving mechanism of the MIT is centered around electron-electron vs. electron-lattice scenarios, in the latter the electron correlation scenario only takes minor importance to the MIT [87], this effect being less prominent. Although there are some reports who look at NbO_2 as having a first-order transition [88–90], others present a much more compelling case that the driving mechanism is indeed a second-order Peierls transition via dimerization of chains of Nb atoms [91–93]. As in the case of VO_2, the electronic and structural MITs might be decorrelated, as experiments showed that ultra-fast laser irradiation of the material can induce the MIT without reaching the critical temperature necessary for the SPT, at laser fluences even lower that the ones for VO_2 [94,95].

Niobium dioxide has been grown using different methods such as PLD [96], MBE [97], ion-beam sputtering [98], and magnetron sputtering [99,100]. Contrary to other deposition methods, sputtering does not easily lead to epitaxial films due to the formation of Nb-O clusters (NbO, NbO_2, NbO_3) in the plasma which affect the nucleation and growth process of NbO_2 [101,102]. Music *et al.* [101] showed that reactive sputtering leads to epitaxial growth of NbO, but may lead to disruption in the growth of epitaxial NbO_2 due to NbO clusters' presence in the plasma, thus, a high control over the plasma sputtering parameters during the deposition is needed, as a balance between Nb-O phases in the plasma is crucial.

I.5.1. Structural properties

Niobium oxides have many phases and polymorphs, albeit fewer than VO_2, with a list of reported niobium oxides being presented in a review article by Nico *et. al* [103]. Among the various compounds however, the most common and important ones are Nb_2O_5, NbO, and, of course, NbO_2, which is discussed in this thesis. Nb_2O_5 is used in applications such as catalysts, in electrochromic and sensor devices or in fuel cells [104] while NbO is interesting due to its superconductivity properties or applications in memory and electrolytic capacitors [103,105]. The Nb-O phase diagram [106] is presented in Figure 13.

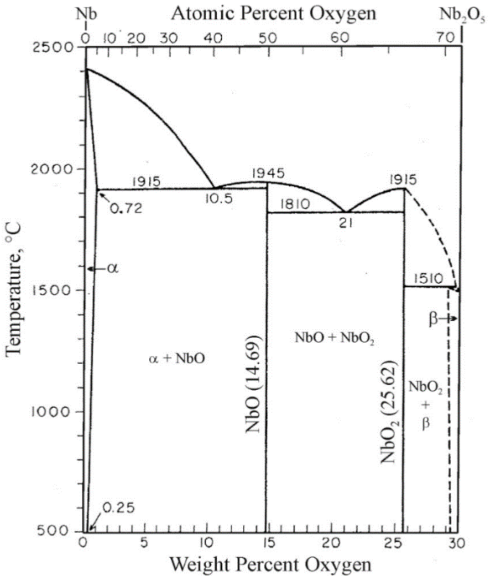

Figure 13. Niobium-oxygen phase diagram. [106]

As opposed to VO_2 which has a transition from an M1 to an R phase, NbO_2 has a tetragonal structure both in the high temperature phase and the low temperature phase, and they are commonly referred to in literature as rutile, space group P42/mnm, and body-centered tetragonal (BCT), or sometimes simply tetragonal, with a space group I41/a (represented in Figure 14). The high temperature phase has the lattice parameters a_R =4.846A and c_R=3.032A [107] while the low temperature phase has parameters a_T=13.702 and c_T=5.985Å, although, slight deviations from these parameters are encountered in the literature [101]. The relations between the high and low phases are $a_T \approx 2\sqrt{2a_R}$, $c_T \approx 2c_R$ [108]. Owing to the dimerization of the Nb atoms, the regular spacing present in the rutile phase disappears with alternating Nb-Nb distances of 2.71 Å and 3.3 Å appearing. A zig-zag displacement develops as well along the rutile [110] and [1-10] directions, with Nb-O lengths varying between 1.91 Å and 2.25 Å [109].

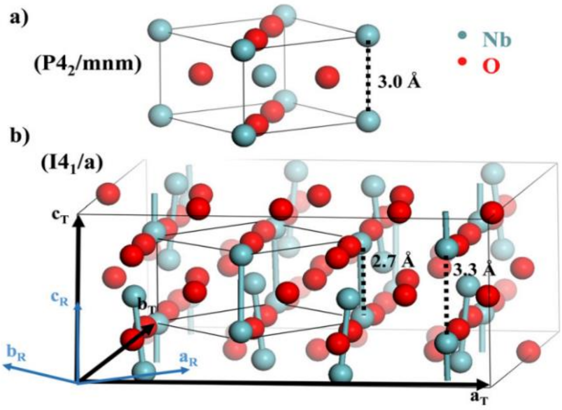

Figure 14. a). Unit cell of the high-temperature phase with rutile crystal structure. b). Unit cell of the low temperature tetragonal phase of NbO_2. [97]

I.5.2. Band diagram of NbO_2

The similarities between NbO_2 and VO_2 led researchers to describe its electronic structure based on Goodenough’s model proposed for the vanadium dioxide [62,99,110].

Niobium dioxide has a $4d^1$ configuration, formed after the bonding of four Nb electrons with the O atoms. These broader 4d bands, in comparison to the 3d bands of VO_2, contribute to stronger metal-metal bonding in the fourth-row dioxides and results in higher transition temperatures for NbO_2. In both the metallic and insulating phases the same features are present, three groups of bands, with the lower ones dominated by O 2p states and two higher energy groups being dominated by Nb 4d states [109]. In metallic NbO_2, the crystal field splitting causes the separation of the higher, Nb 4d, bands into two groups with t_{2g} and e_g^{σ} symmetry. The hybridization of the Nb 4d and the O 2p orbitals also lead to near-Fermi level energy bands, and to the σ-type and π-type overlap with t_{2g} and e_g symmetry respectively. This near Fermi electronic structure consists of two weakly hybridizing t_{2g} bands, namely, $d_{\parallel}$ states with 1D dispersion parallel to the Nb chains, and isotropically dispersing e_g^{π} bands [99,111].

In the case of insulating NbO_2 two main phenomena are occurring, the splitting of the $d_{\parallel}$ band into $d_{\parallel}$ bonding and $d_{\parallel}^*$ antibonding states due to the Nb-Nb dimerization, and the e_g^{π} states’ energy upshift due to higher p-d overlap, leading to a very high depopulation of these orbitals. This upshift is due to the lower Nb-O distances arising from the zigzag-like displacement of the Nb atoms. These changes lead to the complete separation of the $d_{\parallel}$ bands from the e_g^{π} states, which gives rise to a band gap of 0.1 eV [99,109].

I.5.3. Applications of NbO_2

As the thermal transition temperature in NbO_2 occurs at high temperatures, devices based on this material will focus more on the electrical switching effect, although NbO_2 films could have potential applications in high temperature cut-off switches, which have not been yet completely explored. Niobium dioxide has a large dielectric constant (~10 between 1k and 10M Hz) [112], a large Seebeck coefficient (close to -200 μVK^{-1}) [113,114] and a low fluence required for optic excitation (2.2 mJ/cm^2) [94]. These properties enable various emerging applications including thermoelectronics [115], coupled electrical oscillators [116], selector devices [117], memristors based on metal-insulator-metal structure [118,119], electrical and optical switches [98,100], or in the energy domain as catalysts for fuel cells [120]. An advantage that NbO_2 has over VO_2 is that the fluence required to induce the optical activation of the MIT in NbO_2 is lower, and the electronic recovery time is also faster than for VO_2, making NbO_2 better suited for ultrafast switching applications [94].

Taking account of all the bibliographic studies done so far, it is apparent that a significant portion of research conducted on NbO_2 is dedicated to exploring the material's potential application in memory devices, particularly as synthetic neurons [119]. Moreover, compared to VO_2, NbO_2's high temperature MIT makes it less susceptible to unwanted effects coming from Joule heating. That is not to say that the heating of NbO_2 films cannot be exploited, as literature studies reveals the temperature-dependent MIT threshold in electric controlled of the NbO_2 films [121]. This temperature-dependence is interesting for frequency tuning the NbO_2-based oscillators, as it was shown by multiple authors that decreasing the operation temperature of the NbO_2 oscillators (studied between 338 and 4K) leads to lower oscillation frequencies [119,122,123]. This is interesting for NbO_2-based oscillatory networks as frequency tuning by temperature control can be done up until higher temperatures without accidentally triggering an MIT, as would be the case for VO_2.

I.6. Material doping of VO_2 and NbO_2

Modulating the transition characteristics of MIT-capable materials i.e. the hysteresis curve and its associated parameters, has been sought-after by researchers in order to broaden the applications where MIT devices can be used. An already mentioned field that requires a lower T_{MIT} is thermochromics, where it's necessary for the active layers to operate at temperatures close to room temperature.

Much effort has been put into the control of the phase transition, with known methods including oxygen stoichiometry modifications [5], strain engineering [32,90] and doping, the latter being the most common and efficient way. Material doping in its basic form consists of substituting certain of the initial material's atoms with atoms of different nature, with the total concentration usually being relatively low. For example, 1% of tungsten in a VO_2 film is enough to reduce the T_{MIT} by 25- 30°C. The valence difference between the dopant and the material's atoms changes the electronic density of the system and will impact the global conductivity of the material. Researchers have noticed that the size of the dopant is also important, as the MIT materials are sensitive to distortions of the lattice symmetry [124]. A recent comprehensive review on element doping of VO_2 has been presented by Xue and Yin [125]. A usual method of dopant classification is by the type of charger carrier they are introducing, whether it's a hole or an electron i.e. p- or n- doping. This classification however does not account for the dopants that are of the same valence as vanadium that yet still affect the MIT. Moreover, it is still under debate if this classification, which is based on the electronic properties of IV and III-V materials, still holds for transition metal oxides. As such, the dopants within phase transition materials may be classified as:

i) elements that increase the T_{MIT}: in the case of VO_2, notable dopants are Al [126], Fe [127], Si [128] and Cr [129]. While increasing the transition temperature has a practical usage in increasing the efficiency of solar thermal collectors [128], it also stabilizes the M_2 phase of VO_2, thus allowing researchers to study it or employ it in applications that require this normally unstable phase. From the aforementioned doping elements, the most efficient one to increase the temperature of transition is Fe, with the highest T_{MIT} increase reported to around 134°C for 12.6 mol% Fe-doping of VO_2 [127]. Surprisingly, elements such as Cr or Ge can both increase and decrease the T_{MIT} or simply not affect it, which is probably a result of an interplay of effects induced by the deposition technique [125].

ii) elements that decrease the T_{MIT}: in the case of VO_2 there are three types of dopants which are decreasing the composite transition temperature, i) those with lower valence, ii) those with equal valence, and finally, iii) those with higher valence than VO_2. The higher valence atoms are the most efficient ones, as they are introducing electrons into the compound and possibly alter the local structure. Notable examples are W [130], Mo [131], and Nb [132]. From these, the most well-known and commonly used dopant is tungsten, as it has the highest down shifting of the T_{MIT} to temperatures as low as -50°C in nanobeams [133]. Equal valence dopants can be Ti [134] or Hf [135], while examples of lower valence ones are Mg [136] or Sb [137].

While the literature is rich on VO_2 element doping, the same cannot be said for NbO_2. Ti doping of NbO_2 [138] has been investigated in order to improve selector devices for RRAM applications, and showed that doping with Ti helps reduce leakage currents of the devices when in the insulating state. Ti atoms also have the advantage of being oxygen getters due to the favorable thermodynamic properties, this helps prevent the transformation of NbO_2 in the more oxidized Nb_2O_5 phase. Furthermore, N doping of NbO_2 was shown to increase the catalytic activity of the films and improve the stability of the catalyst, to be used in oxygen reduction reaction applications for future fuel cells [139]. Although reports on NbO_2 doping are scarce, it is worth mentioning a different type of doping to the chemical one, which is a variation of electrostatic doping called space charge doping. This technique is used to *n* or *p* dope the material in a way that it remains in this state even after the voltage is applied, by quenching the sample [111].

I.7. Epitaxial growth of VO_2 and NbO_2

The term “epitaxy” has its origin in the Greek words of “epi” meaning “upon”, and “taxis” meaning “arrangement” and as the name suggests, in epitaxial layers the crystal lattice from the substrate is meant to be continued into the thin film. Two categories arise, homoepitaxy, where a film is grown on a substrate of the same composition, and heteroepitaxy, where the compositions and/ or the crystal structure between the film and the substrate are different. Epitaxy produces mono-crystalline films which have different properties when compared to their polycrystalline counterparts. Epitaxial thin films also have fewer defects and grain boundaries, and higher uniformity than polycrystalline films, which directly influence properties such as the optical transparency and the electrical transport (resistivity) in the material [140,141]. In the case of VO_2, epitaxial films have a higher MIT resistivity ratio between the low and high temperature phases, and display much more abrupt transitions with lower widths [142]. Furthermore, the hysteresis shape (T_{MIT}, ΔT, ΔH) can be modulated and specific crystalline phases can be stabilized by strain engineering via lattice mismatch [143,144].

VO_2 has been epitaxially grown on substrates such as Al_2O_3 with different orientations [28,145], on TiO_2 or on MgF_2 [146] by different deposition techniques such a magnetron sputtering [28], PLD [147], MBE [32], chemical vapor deposition (CVD) [145] or e-beam evaporation [143]. As VO_2 grows epitaxially on c-Al_2O_3 and shows the highest magnitudes in the optical and electrical transitions in literature, most of the work in this thesis has been focused on this type of substrate. It has been previously shown that VO_2 layers grow epitaxially with the (010) planes parallel to the (001) planes of c-Al_2O_3, with the epitaxial relationships [100]VO_2‖[210]Al_2O_3, [100]VO_2‖[-110]Al_2O_3, and [100]VO_2‖[120]Al_2O_3 [142].

Figure 15 depicts the (h0l) VO_2 plane and the (hk0) Al_2O_3 plane. The primitive unit cell of VO_2 is represented by black dashed lines on the (h0l) VO_2 plane. Figure 15 b) illustrates the different possibilities for positioning the VO_2 unit cell on the hexagonal structure of the sapphire-c substrate, assuming an angle β = 120°. The presence of three distinct possibilities to position the VO_2 unit cell on the substrate give rise to three distinct in-plane orientations (variants) and this explains with the observed 6-fold symmetry in the φ-scan which will be also illustrated in the Chapter 3 of the manuscript (Figure 37) [148]. In reality, the β angle of VO_2 is equal to 122.6°, indicating that the VO_2 unit cell does not perfectly overlap with the sapphire-c unit cell. The three orientations shown in Figure 15 b) are offset by ±2.6°, as seen in Figure 15 c), which explains specific features in the φ-scan diagrams (Figure 37) [149].

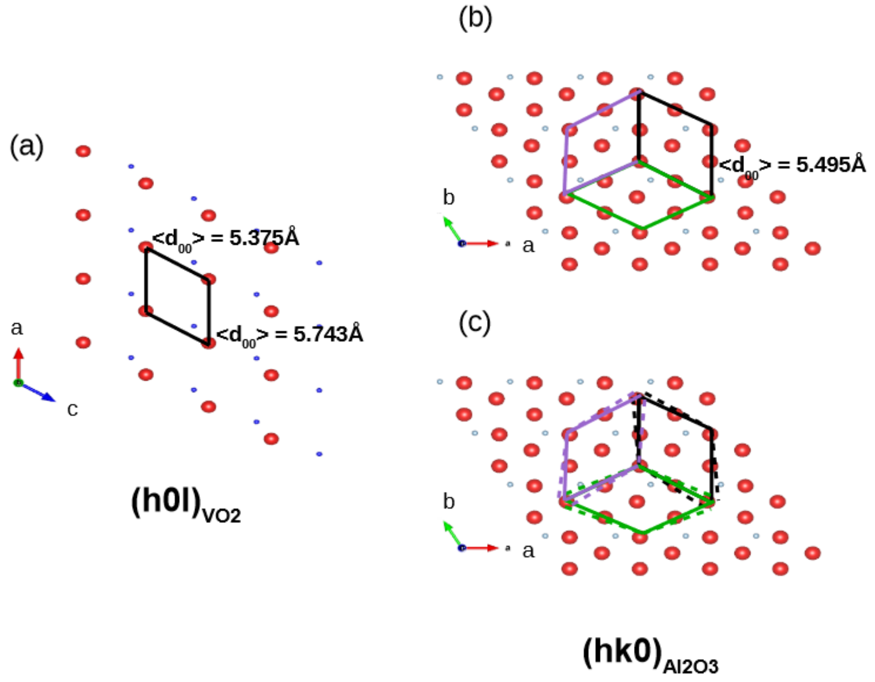

Figure 15. a) Diagram of the primitive unit cell (β = 120°) of VO_2 on the (h0l) VO_2 plane. b) Diagram illustrating the placement of the primitive unit cell of VO_2 (β = 120°) on the (hk0) Al_2O_3 plane. c) Diagram illustrating the placement of the primitive unit cell of VO_2 (β = 122.6°) on the (hk0) Al_2O_3 plane. [150]

A successful method in growing high quality epitaxial VO_2 by magnetron sputtering is to first grow the V_2O_3 phase and afterwards go through a supplementary annealing step in an oxygen-rich atmosphere [151]. Indeed, as illustrated in Figure 16, V_2O_3 and Al_2O_3 have a similar corundum structure and a smaller lattice mismatch between them than for VO_2 and Al_2O_3. The epitaxial relationships were determined to be V_2O_3 (0001)||Al_2O_3 (0001) and V_2O_3[-12-10]||Al_2O_3[-12-10] [152], with the lattice mismatch strain of -3.9% between V_2O_3 (PDF 00-034-0187) and Al_2O_3 (PDF 04-007-1400) along the a axis, while for VO_2 and Al_2O_3 is -4.4% along the [100] VO_2 and 2.1% along the [001] VO_2. Moreover, as mentioned previously in section I.2.1, V_2O_3 and VO_2 are the two end members of the Magnéli family thus transition from V_2O_3 to VO_2 can be easily achieved by an annealing step in an oxygen atmosphere.

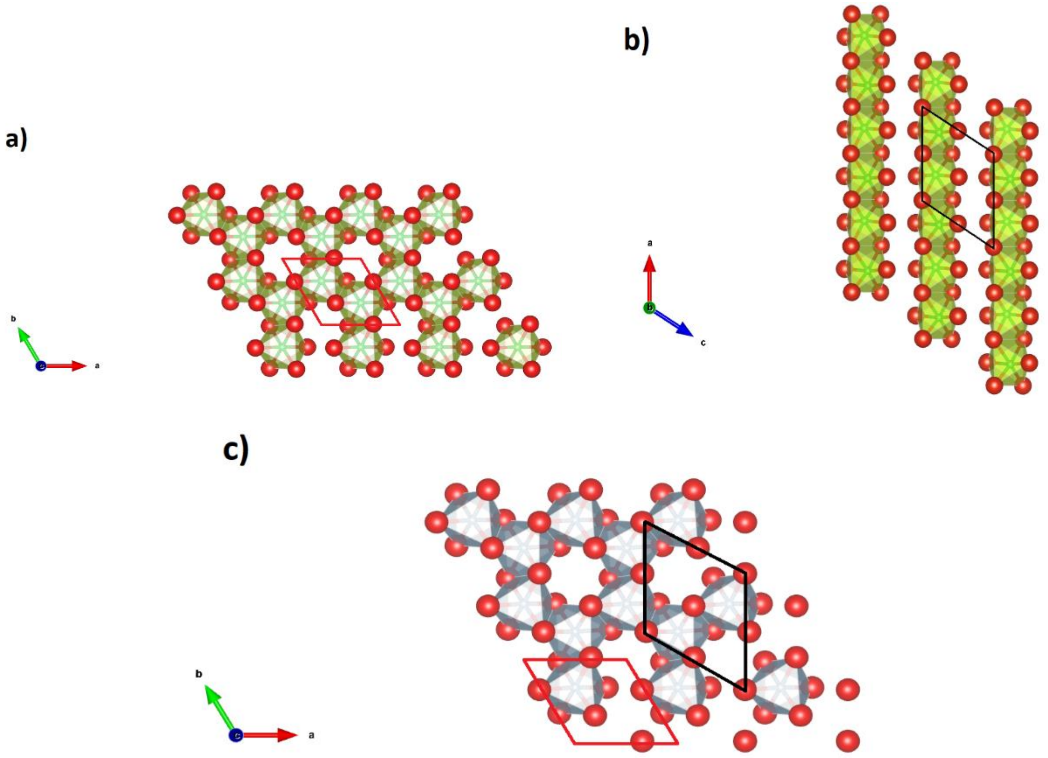

Figure 16 a) V_2O_3 structure and unit cell b) VO_2 M_1 structure and unit cell c) Al_2O_3 structure and unit cell (red, identical to V_2O_3) and VO_2 (black).

In the case of NbO_2, epitaxial growth has been achieved on MgF_2 substrates using MBE [6], ion beam sputtering [153] and PLD [154], on c-Al_2O_3 by PLD[90] and reactive bias target ion beam deposition [155], and on STO substrates by MBE [97]. The epitaxial relationships between NbO_2 and c-Al_2O_3 (illustrated in Figure 17) have been reported to be [001](110)NbO_2||[10-10](0001)Al_2O_3 [155]. Substrates such as MgF_2 or TiO_2 might be more favorable to grow epitaxial NbO_2 as the structures are similar, thus leading to a lower structure mismatch between the substrates and the obtained layers [156]. As mentioned earlier, during reactive magnetron sputtering deposition, Nb-O clusters in the sputtering plasma may hinder the formation of epitaxial growth of NbO_2, and thus, favorable conditions for epitaxial NbO_2 growth require extensive investigations of deposition parameters.

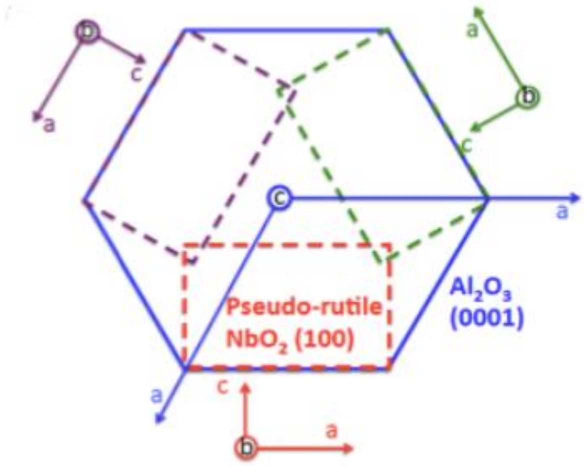

Figure 17 Illustration depicting the epitaxial relationship between the tetragonal structure of NbO_2 and a sapphire substrate. [155]

I.8. Conclusion

In this chapter a short introduction of the metal-to-insulator transition has been made, afterwards the two most important and common driving mechanism of this transition have been discussed, namely Mott transition and Peierls transition. This was followed by introducing the two materials that are the focus of this thesis, their phase family, band diagram, properties and applications. As tungsten doping represents an important part in my research, a chapter dedicated to VO_2 (and a much lesser extent NbO_2) doping was the focus of a separate chapter. Finally, the epitaxial growth of materials and the epitaxial relationships between out materials and c-sapphire substrate (the main substrate used in my research) were explored, which are important in controlling the crystalline quality of the films and thus the electrical or optical performances.

During this thesis research on VO_2 and NbO_2 I have employed reactive DC magnetron sputtering in order to grow thin films of these materials. Moreover, using photolithographic methods simple devices (oscillators, electrical and optical modulators) have also been fabricated. In order to characterize these films, the main techniques used throughout the thesis were X-ray diffraction, electrical measurements, Raman spectroscopy, atomic force microscopy, THz-TDS spectroscopy and Rutherford backscattering spectrometry. The methods of deposition and characterization are the focus of this chapter and will be described below.

II.1. Magnetron Sputtering

Magnetron sputtering is a physical vapor deposition (PVD) technique based on the diode sputtering deposition method, but with an incorporation of a magnetron. A diode sputtering works on the simple principle of ejecting atoms from a material of interest, called a target, in order to deposit them on a substrate located in close vicinity to it. In its most basic form this is achieved in a vacuum chamber by introducing a non-reactive and relatively inexpensive gas, which is usually argon, between two planar electrodes and applying a voltage which, when increased above the breakdown value of the gas, will create a self-sustaining plasma that initiates the sputtering process. A DC glow discharge is characterized by different and distinct regions which will be briefly described as they are key in understanding the sputtering process. After the plasma is started, in the region next to the cathode (usually the target material) a dark space called the Aston dark space can be seen, where a strong electric field is present but the electrons ejected from the cathode don’t have enough energy to ionize the gas. As the electrons accelerate and gain energy they begin to excite the Ar inert gas atoms which quickly transition back to their ground level while producing luminous radiation, thus creating the second region called the cathode glow. As electrons further accelerate they ionize the Ar atoms which accelerate to the negatively charged cathode, this region is called the cathode dark space. The ions that hit the cathode (target) produce secondary electrons that maintain the plasma. The bombardment of the target by the ions ejects atoms from the target is the so-called sputtering process which ultimately produces the thin films. Next to the cathode dark space is the negative glow that is formed by the electrons that are slowed down after ionization and thus have enough time to combine with ions and emit light. After this intense light zone, the Faraday dark space and the positive column follow, the anode dark glow and finally the anode dark space. All these zones of a DC glow discharge are represented in Figure 18. By placing a substrate close to the anode one can collect the sputtered material that forms into a thin film.

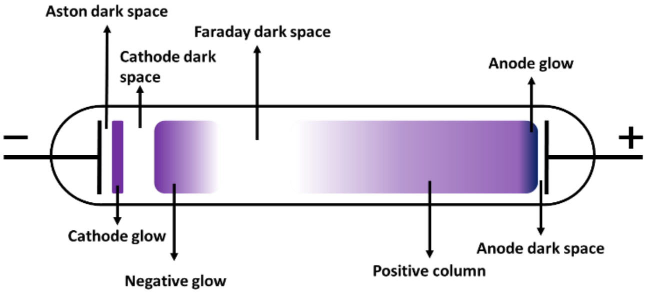

Figure 18. DC glow discharge regions in a typical diode sputtering system.

In order to improve this technique by increasing the deposition rate and lowering the discharge voltage, the lifetime of electrons around the cathode needs to be increased. The simplest method to do so is to confine the electrons with a magnetic field, or a magnetron, hence the name of the technique called magnetron sputtering. A schematic of the magnetron sputtering technique is represented in Figure 19 a), showing the magnetic lines that confine the electrons, which ionize the Ar atoms that are further accelerated towards the cathode, and the target atoms being sputtered and depositing on the substrate.

The trapping of electrons by the magnetic field leads to a large percentage of the ionization occurring around the target as can be seen in Figure 19 b), which is an optical image of one of the sputtering systems used during this thesis [157].

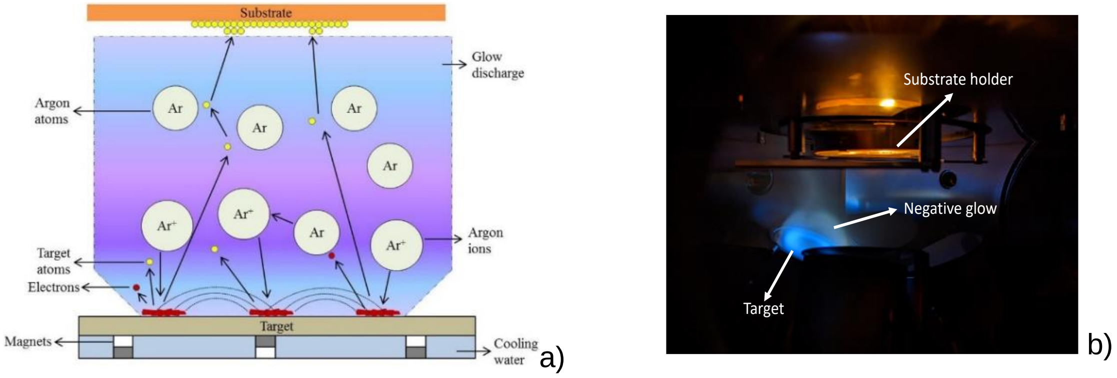

Figure 19. a) the schematic of magnetron sputtering [158] and b) experimental setup of reactive DC magnetron sputtering.

II.1.1. Reactive magnetron sputtering

The introduction of a reactive gas, usually O_2 or N_2, along with the non-reactive one during the sputtering process has been successfully used to fabricate new compounds such as oxides, nitrides or oxinitrides. In the context of this thesis as the sputtering will be done from metallic vanadium and niobium targets, the reactive gas of interest is O_2. The way this works is seemingly fairly straightforward: the reactive gas, oxygen in our case, is introduced in the sputtering chamber and will react with the exposed surfaces (target, substrate, chamber walls) thus creating oxidized phases. Reaction can be considered as non-existing in the gas phase as the densities of the gas and the sputtered atoms are low and collisions are rare [159]. While it sounds easy, the reaction mechanisms between the reactive gas and the sputtered material may lead to some stability issues.

In the case of the DC reactive sputtering (employing metallic targets), at zero gas flow of oxygen, the sputtering yield and sputter erosion rate is determined by the target material. Increasing the reactive gas flow up until a certain critical value does not alter significantly the composition of the target and the sputtering yield will remain constant for a given power. This is because all the reactive gas is absorbed either at the substrate level or is being sputtered as soon as it is chemisorbed by the target. In this region the target is said to operate in “metallic mode”. At a certain critical value, the partial pressure of oxygen is high enough and the compound formed on the target starts to dominate the sputtering with a yield that is much lower than the metallic one. As the target becomes oxidized, the excess oxygen that has not been chemisorbed will contribute to increasing the partial pressure of oxygen. This gives rise to an avalanche effect where the lower sputtering yield leads an increased partial pressure of oxygen around the target which in turn leads to an even lower sputtering yield. This region is sometimes called a “transition mode”. After the process stabilizes, the target is said to be in a “poisoned mode” and has a drastically lower deposition rate than the metallic mode. These regions, alongside the voltage evolution with oxygen for one of our vanadium targets can be seen in Figure 18. Many factors may contribute to the shape of this said “poisoning curve” such as vacuum chamber size, vacuum pump speed or target history and purity. As in our experiments the plasma discharge is operated under a constant power, the voltage (and current) changes and reflects the target’s oxidation state, as illustrated by the curve of the voltage evolution with the reactive gas partial pressure (or flow under a constant pressure).

During the course of this thesis research, the VO_2 and a portion of the NbO_2 films were fabricated inside a 3” DC magnetron sputtering vacuum chamber (PLASSYS MP300) configured in a sputter-up formation. The temperature of this system was capped at 750°C and the substrate rotation was maintained at 12 rotations/ minute in order to ensure a uniform deposition. Several NbO_2 films were fabricated using a PVD6 3” deposition system equipped with up to six magnetron sputtering sources, with RF, DC and pulsed DC source power supplies was also used. Figure 19 b) offers an inside view of the sputtering chamber during deposition.

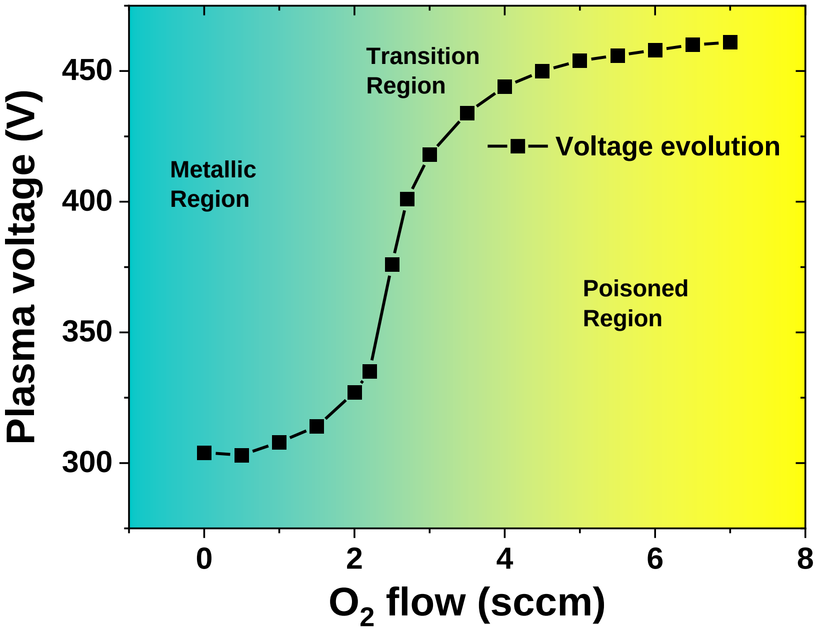

Figure 20. Plasma voltage during vanadium target sputtering evolution with different oxygen flows (under a constant 70 sccm flow of Ar and fixed total pressure of 4 mTorr).

II.2. X-ray diffraction analysis

II.2.1. X-ray diffraction theory

Diffraction effects are observed when the electromagnetic radiation that falls on a periodic structure, with wavelengths comparable to the size of the structure, interfere constructively. One can apply this effect to crystals and molecules, where the interatomic lengths are usually of a few tenths of nanometers, using X-ray radiation. Indeed, X-ray diffraction (XRD) is a powerful non-destructive characterization technique that allows for gathering information about the crystal structure of the materials. Notably, it allows for the determination and the quantification of the crystalline phases in the material, their orientations, the strain in the material or the size of the crystallites.

The collision between the x-rays and the matter gives two types of interactions, an inelastic scattering (Compton scattering) where energy is transferred to the electron but doesn't release it, and an elastic scattering (Thomson scattering) where the electron starts to oscillate at the frequency of the incoming radiation and becomes itself a source of radiation. This latter process is what XRD uses for structurally analyzing the films. Since the energy is conserved, the incident wave vector, k_0, and the diffracted wavevector, k_d, have the same magnitude 1/λ, λ being the wavelength. Diffraction occurs when the waves scattered by different lattice planes of the material coherently interfere, i.e. when the path difference between the scattered waves, $\delta = \delta_1 + \delta_2$, equals an integer multiple of the x-ray wavelength nλ. This geometry is depicted in Figure 21 below, from which Bragg's law is straightforwardly obtained as:

$$2dsin\theta = n\lambda \qquad (4)$$

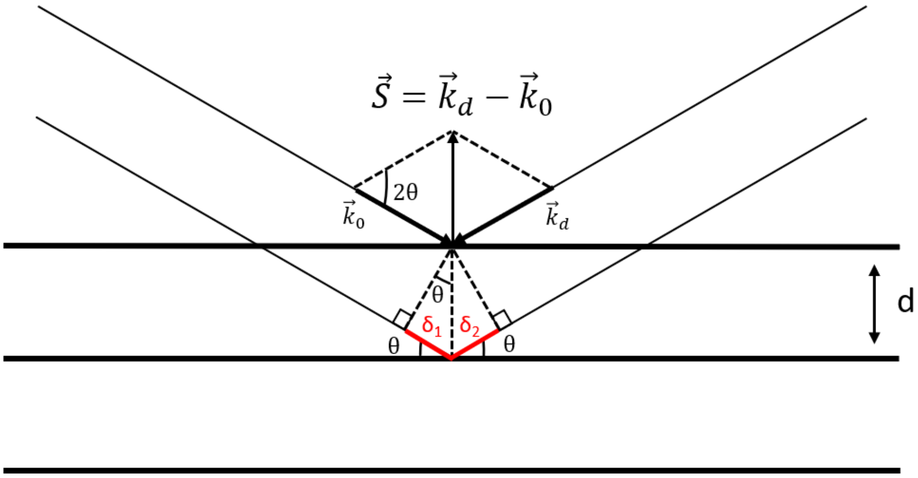

Figure 21. Representation of Bragg's law.

The figure also represents the diffraction vector $S = k_d - k_0$, with magnitude $2sin\theta/\lambda$, which will be used below.

As useful as it is, Bragg's law describes diffraction in a 2D plane, whereas diffraction actually occurs in 3 dimensions. Also, it doesn't give any information regarding the intensity of the diffracted X-rays. Within the kinematical theory of diffraction, the intensity diffracted by a material can be written as:

$$I(S) = \left|\sum_j F_j(S)\exp(-2\pi i S\cdot r_j)\right|^2 \qquad (5)$$

where F is the structure factor of the jth unit cell and r_j is the distance of the jth unit cell. Being a Fourier series, Equation (5) exhibits maxima when $\boldsymbol{S}\cdot\boldsymbol{r_j}$ is an integer, which, from the definitions above is equivalent to Bragg's law. This allows to express the diffraction condition in a different way; since d_j is a real space vector, i.e. $\boldsymbol{r_j} = \boldsymbol{ua} + \boldsymbol{vb} + \boldsymbol{wc}$ (a, b,c being the lattice parameters of a crystalline structure), the only way to satisfy that the scalar product $\boldsymbol{S}\cdot\boldsymbol{r_j}$ is an integer is that the scattering vector S is a reciprocal lattice vector, i.e.

$$S = d^* = ha^* + kb^* + lc^* \qquad (6)$$

a*, b*,c* being the reciprocal lattice parameters

Reciprocal lattice

A crystal is a regular structure defined by repeating a pattern placed on the nodes of a three-dimensional lattice with the base vectors $\vec{a}$, $\vec{b}$, and $\vec{c}$. The reciprocal lattice, with its base vectors $\vec{a}^*$, $\vec{b}^*$, $\vec{c}^*$, can be associated with the direct lattice. The base vectors of the reciprocal lattice are defined as following:

$$\vec{a}^* = \frac{\vec{b} \wedge \vec{c}}{v}, \vec{b}^* = \frac{\vec{c} \wedge \vec{a}}{v}, \vec{c}^* = \frac{\vec{a} \wedge \vec{b}}{v} \qquad (7)$$

Where v represents the volume of the unit cell in the direct lattice, calculated as $v = \vec{a} \cdot (\vec{b} \wedge \vec{c})$

Ewald sphere

The above diffraction condition can be further simplified to the Laue condition states that the diffracted signal will have maximum intensity in a given direction if and only if the scattering vector $\vec{S}$ is a vector in the reciprocal lattice. Diffraction will occur when a node of the reciprocal lattice intersects the Ewald sphere [160], which represents all possible $\vec{Q}$ vectors.

In order to bring the diffraction node onto the Ewald sphere and gain access to information about the crystalline structure of the material, several parameters can be modified, such as the sample orientation, the X-ray source direction, or the wavelength of the incident photons. In the present work we use a setup, described below, with a fixed wavelength and a fixed incident beam direction.

II.2.2. Experimental XRD setup

The X-ray diffraction measurements were performed using a commercially available D8 Discover diffractometer from Bruker. It is equipped with a copper X-ray source ($CuK_{\alpha1}$, λ = 1.5406Å), a multilayer parabolic mirror, and a 4-reflection monochromator with germanium (Ge) crystals with (220) orientation. The linear detector covers a range of 2° in 2θ with an angular resolution of 0.01°. For all our analyses, a 200 µm slit was used to reduce the beam thickness.

To increase the intensity of the incident beam while preserving angular resolution as much as possible, the second crystal of the monochromator was removed, resulting in a configuration with 2 reflections instead of 4. To verify the influence of this modification, a rocking curve, explained in the following section, was performed around the (006) position of the sapphire. The obtained peak was simulated to determine its intensity and full-width at half-maximum. The use of a 2-reflection monochromator allows tripling the peak intensity without sacrificing too much the resolution (minimal increase in the full-width at half-maximum). Consequently, all the XRD studies were conducted using the 2-reflection monochromator with germanium crystals.

The sample holder consists of an Eulerian cradle equipped with three rotations ω, ψ, and φ. A stage that controls the x, y, z directions allows for sample positioning. The z motor adjusts the sample height, while the x and y motors enable lateral sample positioning. Additionally, the sample flatness can be adjusted using a dual tilt stage ξ/ζ. This allows the crystal to be rotated around the surface normal while maintaining the Bragg condition for a given plane family.

The diffractometer is also equipped with a DHS110 furnace (commercialized by Anton Paar) that enables *in-situ* analyses up to a temperature of 1100°C under ambient or controlled atmosphere. This furnace features an Al_2O_3 stage on which the sample is placed. Heating is achieved through a resistive heating element located beneath the alumina stage. To provide thermal stability to the sample, a graphite dome (a low X-ray-absorbing material) is placed over the entire setup.

II.2.3. Types of XRD measurements

Rocking curve scan (ω scan)

In a rocking curve type scan, represented in Figure 22 a), the sample is rotated ("rocked") in a given ω range, while the detector remains in a fixed 2θ position. In this geometry, and for low rocking angles (~1°), the scattering vector moves in a direction almost parallel to the sample surface. As such, the rocking curves contain information in the "in-plane" direction of the sample. A perfect crystal will produce a very sharp peak, while defects coming from mosaicity, dislocation and curvature will create disruption in the parallelism of the atomic planes and will lead to a broadening in the ω scan.

θ-2θ scan

The θ-2θ scan is one of the most used types of scans for its relative simplicity and amount of information extracted. In this scan the X-ray radiation hits the sample at an angle ω = θ whereas the detector is set at twice that angle, 2θ, hence the name of the scan. During the scan the sample orientation is varied, by the Δθ steps, while the detector is rotated by the 2Δθ steps. The θ-2θ naming comes from the fact that the scan can be understood as a variation of the exit angle with respect to the extended incoming beam. In these types of scans the scattering vector is always oriented perpendicular to the crystal's surface, thus only information along this "out-of-plane" direction contribute to the Bragg reflection. The scan is represented in Figure 22 b).

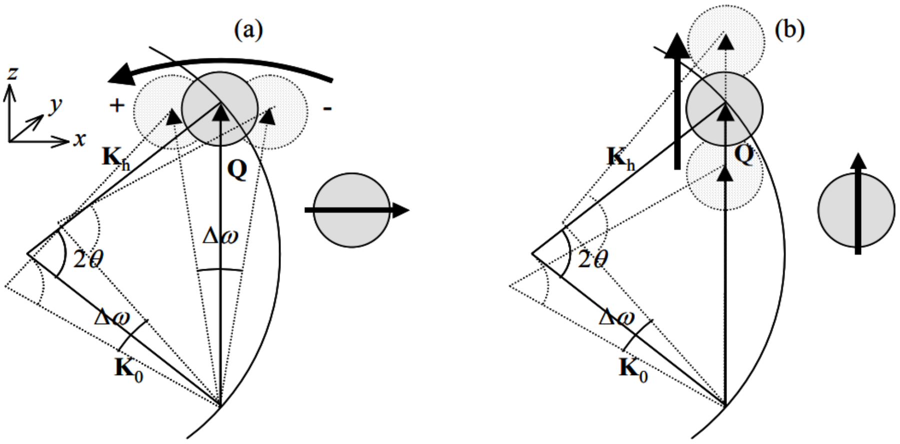

Figure 22. Reciprocal space view of the a) ω scan and b) θ-2θ scan. [161]

Azimuthal scans (φ scan)

The φ scans consist in rotating the sample along the φ axis while maintain fixed θ and 2θ axis. This scan allows to detect all equivalent planes, in the in-plane direction, to pass in Bragg position. Comparing the φ-scan of the grown thin film and the Φ-scan of the substrate allows for comparing the epitaxial relationships between them.

Grazing incidence X-ray diffraction (GIXRD/2θ scan)

Grazing incidence (GI) scan consists of a 2θ scan while the incidence angle is maintained constant and low angles between 0.2 and 2°, hence the name “grazing incidence”. Due to the low angles used, this scan type allows for an increased volume of the sample irradiated by the x-rays and thus an increased intensity of the obtained signal. GIXRD gives information on those lattice planes that are not oriented. For instance, a randomly oriented polycrystalline sample will produce a conventional powder diffraction pattern, whereas an epitaxial film, or a single crystal will produce no signal at all

It is worth noting that the results of the performed scans have been analyzed using different fits (PearsonVII, Voigt, Gauss, etc) using Fityk and OriginLab as analysis programs. Furthermore, large diffraction data files, such as the temperature-dependent sans or the ones of reciprocal space mapping or from other combined scans (Φ scans + ω scans) have been processed using DxTools, a free and open-source program developed for that purpose [162].

II.3. Electrical characterization techniques

II.3.1. Four-point probe measurements

Four-point probe measurements, shown schematically in Figure 23, is a simple and nondestructive way of determining the resistivity of a material. In this method four sharply tipped wires, usually made of tungsten, come into contact with the surface to be measured. A known current is passed between the outer tips, while a voltage reading is recorded between the inner tips.

The extracted sheet resistance (R_S), is measured in ohm/square or Ω/□. When the thickness t of the layer is known then the resistivity can be calculated from:

$$\rho = \mathrm{R_S t} \tag{8}$$

However, when considering a real sample, it is necessary to account for the edge effects. Therefore, correction factors for the diameter (CFd) and thickness (CFt) need to be applied to the sheet resistance measurement. CFd is defined by the ratio between the length of the material and the distance between the tips *d/s* and CFt by ratio between the width and the thickness of the material *a/d*. In our measurement setup *s* has a size of 1 mm and the area of the films, unless stated otherwise, are 10x10 mm^2, corresponding to CFd = 4.22 and Cft = 0.99. Taking all into consideration, R_S takes the form in equation (9), where *I* is the applied current between the two outer tips and *V* the voltage between the inner tips.

$$R_S = \left(\frac{V}{I}\right) CF_d CF_t \tag{9}$$

Furthermore, in order to measure the evolution of resistance with increasing temperature the films and substrate have been placed on a Peltier heating element. A thermocouple is placed near the surface of the films in order to measure their temperature. The measurements were typically done in the temperature range of 25°C (or room temperature) and 95°C.

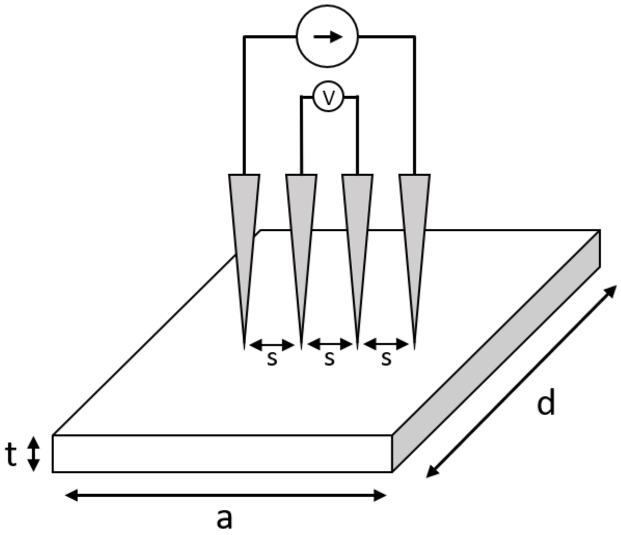

Figure 23. Four-point probe measurement set-up.

II.3.2. Current-voltage characteristics of the oxide-based devices

In order to measure the current-voltage characteristics of the films and evaluate their electrical performances, planar devices were fabricated using a combination of lithography techniques and electron-beam evaporation to deposit metallic electrodes separated by VO_2 patches of different sizes. Current-voltage (I-V) curves were recorded to test the electrical activation of VO_2 and NbO_2, to evaluate the optical activation of some of the films and to assess the degradation of the films' properties during repeated thermal activations. Two functioning modes were used for the I-V curves. The first one is voltage control where the source (Keithley 2112A sourcemeter unit) applies a voltage sweep on the device and the current is measured, while the second mode is current-controlled, the source injects a progressively increased current in the device and the associated voltage is measured.

For VO_2, in the voltage control (voltage sweep), the electrically-induced insulator-to metallic transitions (IMT) are identified by an abrupt jump in the current values for a specific voltage threshold (Figure 24 a)). Thus, once the threshold voltage value is reached, the material transforms from an insulating to a metallic state, hence the current jump. For decreasing voltage, the metal-to insulator transition or MIT is triggered at a lower voltage, giving rise to a hysteresis in the I-V curve.

In the current control mode (current sweep) (Figure 24 b)), the I-V curve takes a different shape. While the increased current is imposed to the circuit, the voltage increases up to the threshold value and, once the MIT is triggered, the voltage starts to drop with increasing current until the MIT is finalized. This region between the two points is called a negative differential resistance and is of particular interest in initiating periodic oscillations in the circuit.

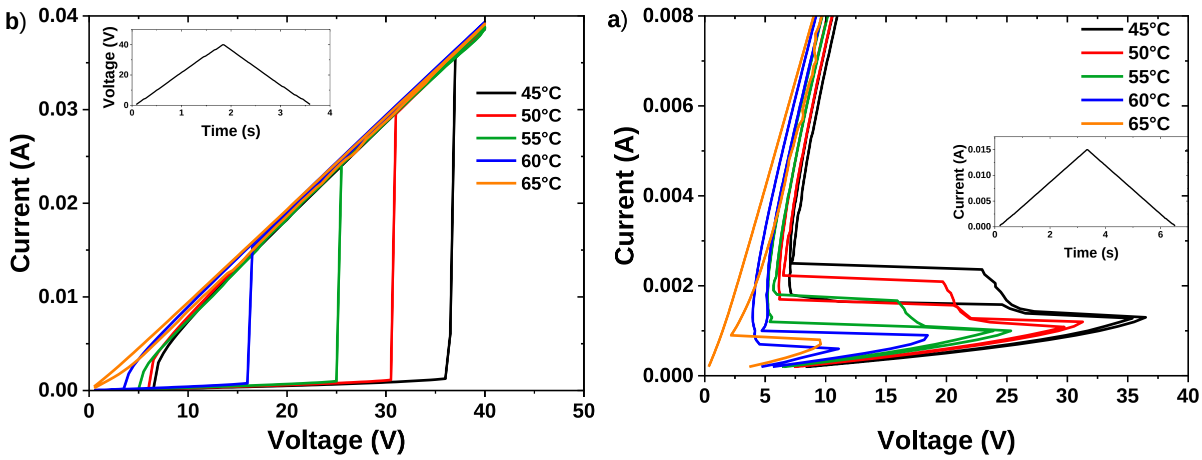

Figure 24. Typical I-V characteristics of a) voltage-controlled sweep and b) current-controlled sweeps of VO_2 films at different temperatures. Inset are the voltage/ current evolutions with time (graphs obtained from Oihan Allegrets's measurements).

II.4. Terahertz time-domain spectroscopy

Terahertz time domain spectroscopy (THz-TDS) is used to measure the transmission, reflection and the optical constants (refraction index and absorption) of materials in the THz domain (0.1-10 THz). A typical THz-TDS system uses a technique based on two photoconductive antennas for generating and detecting both the amplitude and phase of THz waves. The process involves exciting these antennas using a femtosecond laser that usually has a central wavelength of 800 or 1550 nm and a repetition rate of 80 MHz. To ensure synchronous detection, the laser beam is divided into two beams - one used for generating the THz radiation and the other for synchronously detecting it (Figure 25). The THz field at the detector is measured using a synchronous detection amplifier and a current amplifier, provided that the terahertz wave and laser beam reach the detector at the same time. The temporal THz signal is obtained by sampling it over time using an optical delay line in the detection path of the laser beam.

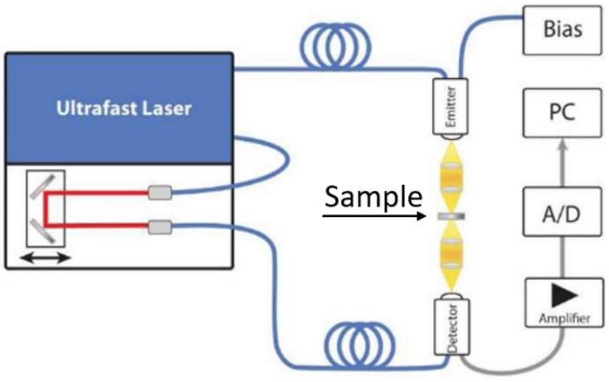

Figure 25. Schematic of a THz-TDS setup (TeraK15 from Menlo Systems). Indicated with an arrow is the sample position.

In THz-TDS, as the name implies, the THz pulse is constructed as a function of time, but the data can be represented in the frequency domain using a Fourier transformation. In the system we use (TeraK15 from Menlo Systems) the THz beam is focused with the beam dimension on the sample being of 2 mm. The system's antenna's maximum emitter optical power is of 30 mW at 1550 nm, with a laser repetition rate of 100 MHz.

In Figure 26 a) a typical THz-TDS time signal travelling through air (black curve) and through air plus a c-sapphire substrate (red curve) is presented. Figure 26 b) represents the spectra after the FFT step was performed. In order to eliminate the influence from the background (ambient atmosphere) and the substrate spectrum, it is necessary to perform a subtraction step after sample was measured. This ensures that the specific absorption lines of water vapors in the atmosphere and the simple substrate are effectively removed. In order to minimize these absorption lines, the measurements can be performed in a dry air purged enclosure. For our experiments the samples were mounted on a Peltier device with a hole in the middle, this was done in order to control the MIT and to let the THz radiation pass through. The measurements were performed with a time window between -234.23 ps and -224.26 ps, with a step of 0.0(33) ps, which after an FFT translates roughly from 0.001 to 15 THz. It is however important to note that when analyzing the data only the 0.2-2 THz window could be used, as at other frequencies the noise was too large to extract meaningful data.

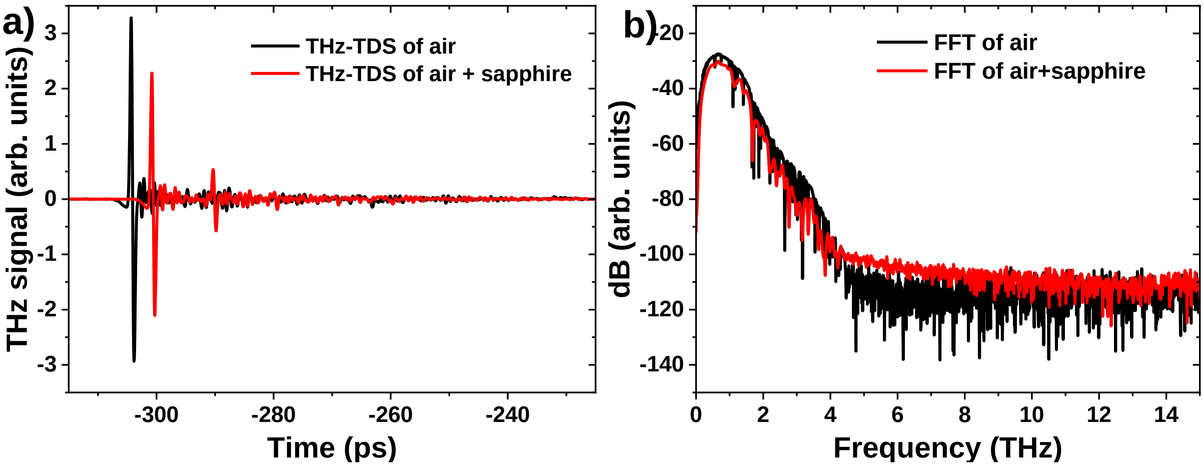

Figure 26. a) THz-TDS spectra of air and air + the sapphire substrate b) Fast Fourier transform of the air + sapphire THz-TDS signal.

II.5. Other characterization techniques

While the same deposition method, XRD and electrical measurements were used throughout the thesis and for almost all the samples, other characterization and fabrication techniques were occasionally used and thus only briefly mentioned hereafter.

Raman spectroscopy

Raman spectroscopy is a method that consists in irradiating the sample of interest with a monochromatic wave generated by a laser. The Raman shift (the difference between the scattered light and incident light) is usually between the frequency range of 10-4000 cm^{-1}. This method is used to probe the vibrational modes of a material which gives essential information such as the atomic bonding properties, the chemical structure and the crystallinity.

A part of the Raman spectroscopy experiments was performed at XLIM using a Raman inverted microscope (Horiba LabRAM HR Evolution) using the excitation from a continuous HeNe laser (λ= 632.8nm) with an incident power of 6 mW and focused on the sample with a 60× objective to a spot of ~ 2 μm in diameter. The rest of the experiments were performed at

IRCER by Maggy Colas and Julie Cornette using an inVia Reflex Renishaw confocal Raman spectrometer. Raman data were collected using a 50× objective and a holographic grating of 2400 lines/mm using a 532-nm excitation laser with a power of 40 mW. The recorded spectral range was 100–1200 cm^{-1}, with various acquisition times. As for the electrical measurements, a Peltier thermoelectric element was used to control the heating and the cooling of the samples.

Rutherford backscattering spectroscopy (RBS)

RBS is a non-destructive elemental analysis technique that is used to identify and quantify the chemical elements contained in materials down to thicknesses of a few hundred nanometers. It is based on the irradiation of the material to be studied with a He ion beam (from 100 keV to a few MeV) and then analyzing the energy of the ions backscattered by Coulomb repulsion with the target nuclei. RBS measurements were performed, analyzed and interpreted at the JANNuS-SCALP facility (IJCLab, Université Paris Saclay) by Aurelian Debelle and Lionel Thomé who have vast experience in this characterization technique. In the framework of this thesis, it was used to determine the V, W and O content in doped W:VO$_2$ films.

Atomic force microscopy (AFM)

AFM and profilometry are both techniques used to characterize the topography of thin films. The typical AFM setup consists of a laser, a cantilever with a sharp tip, usually made of silicon or silicon nitride and mounted to a piezoelectric actuator, and finally a photodiode for receiving the reflected laser beam from the end-point of the cantilever. The sharp tip scans the sample's surface and registers the slight variations in the height of the tip, which corresponds to the morphology of the substrate. The AFM operates in three modes: i) non-contact, where the tip hovers over the sample surface at distances small enough for the van der Waals force to cause the tip to oscillate. A feedback loop control maintains a constant oscillation frequency and the vertical movements of the piezoelectric motor are recorded to reconstruct the surface ii) tapping mode, where the tip oscillates and comes intermittently in contact with the sample and iii) contact mode, where the tip is brought into close contact with the sample and an electronic feedback loop ensures the deflection remains constant during the scan. In our case, the topography of the layers was analyzed using a Dimension Icon AFM-Bruker microscope at IRCER by Valerie Coudert.

Photolithography

Photolithography is one of the most used methods for obtaining nanoscale circuits and devices due to its ease of use and low processing time. In photolithography a photoresist coating is applied to the sample of interest which is then covered by a photomask with the desired structures printed on it, and then irradiated by, usually, UV light. The end step is submerging the film into a developer, which selectively removes the exposed/ unexposed regions of the photoresist, this step reveals the mask's pattern on the substrate.

There are two types of photoresist: i. positive, where the areas exposed by the radiation become soluble to the developer, and ii. negative, where the opposite effect happens, the irradiated area becomes insoluble to the developer.

By utilizing an additional technique called "lift-off", circuits are patterned on the substrate by coating the surface with a gold thin film that will deposit everywhere including in the gaps left by the mask. Finally, film is submerged in a solvent, such as acetone, in order to remove the photoresist covered with the new coating, and reveal the final circuit. A schematic of this technique employing a positive photoresist is represented in Figure 27, it is also worth mentioning that just before the Au coating a very thin titanium layer can be also evaporated onto the film in order to improve gold adhesion.

Conversely, the opposite of the “lift-off” technique which is named “etching technique” can be employed. In this technique, after the metal is deposited and the mask is developed, an etching of the metal through the resist pattern is done. Afterwards, the mask is removed with a solvent, revealing the final circuit. Photolithography has been used in order to create simple planar devices with electrodes of different sizes separated by VO_2 or NbO_2 patterns.

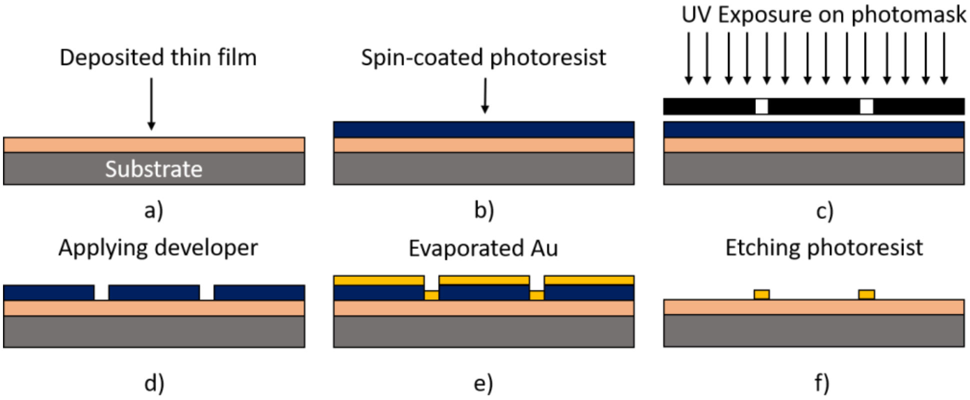

Figure 27. Simplified lift-off process a) sputtering of VO_2/ NbO_2 thin films b) spin-coating a positive photoresist layer c) exposing the photoresist to UV light d) removing the exposed surface with a developer e) evaporating Au on the film f) removing the rest of the photoresist in order to reveal the wanted circuit.

II.6. Conclusion

In this chapter the main and most important fabrication (reactive DC magnetron sputtering, photolithography) and characterization (XRD, AFM, RBS, Raman, THz-TDS, electrical characterization technique) methods that will be used throughout the thesis have been described. Even though these are the main ones, it is possible that other techniques, such as infrared thermal imaging, will be employed at various stages of sample and device analysis.

In the next chapter the methods described here will be put to use in order to optimize the fabrication of high quality VO_2 films and to characterize their thermal, electrical and optical properties.

Chapter III. Study of VO_2 thin films fabricated by reactive magnetron sputtering

As the focus of the thesis is on attaining comprehensive control over the performances of VO_2 and NbO_2 thin films by establishing correlations between the structural, optical and electrical properties, it is important to understand the influence of the synthesis parameters over the intrinsic properties of the films. It should be mentioned that the group's prior experience of VO_2 thin film growth using e-beam evaporation was of great help in achieving this task.

III.1. Initial steps on obtaining VO_2 films. Oxygen flow control and annealing

III.1.1. As-grown films

In the reactive magnetron sputtering system various depositions parameters can be controlled, among these, all the depositions were done at a sputtering power of 150 W, 70 sccm Ar flow and variable O_2 flow, at a total chamber pressure of 4 mTorr. Unless mentioned otherwise, the films were deposited on 10×10 mm^2 c-sapphire substrates, however, the sputtering set-up allows for large area depositions on substrates as large as 50×50 mm^2 or 3" wafers (as seen in Figure 28).

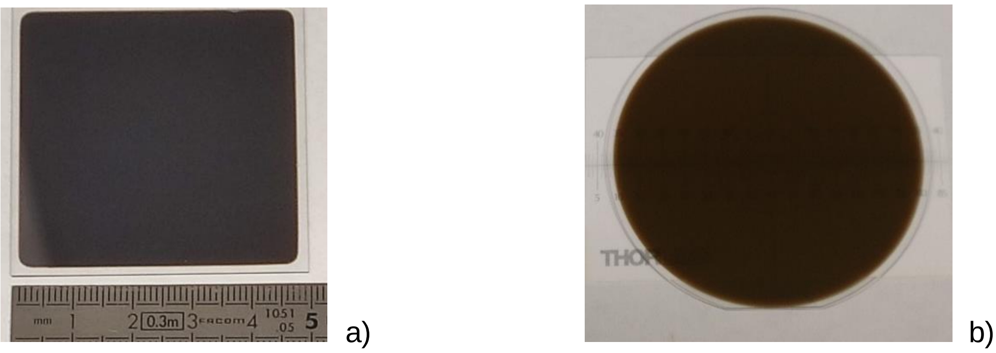
a) b)

Figure 28. VO_2 film deposited on a a) 50×50 mm^2 substrate and b) 3" diameter wafer

In order to find the optimal oxygen flow for synthesizing VO_2, the first step was establishing the oxygen poisoning curve of the target, which was defined in the previous chapter. The methodology for obtaining the curve was as follows: 1) pre-sputtering the target in order to remove unwanted contamination, such as oxidized species or carbon; 2) adding O_2 to the Ar atmosphere at a specific flow value; 3) letting the plasma stabilize, and measuring its current and voltage; 4) reducing to 0 sccm of O_2 and repeating the steps with increasing O_2 flows. This was done in order to reproduce a real deposition experiment for our specific experimental setup. Furthermore, in order to evaluate the influence of the target composition on the poisoning curve, and ultimately on the characteristics of the thin films, two vanadium targets have been used. Thus, we utilized one target which has been previously used on other experiments with a V purity of 99.5%, that will hereafter be named Target 1 or T1, and a second one, brand new target with a purity of 99.9%, which will be named Target 2 or T2. The measured poisoning curves of the two targets are represented in Figure 29. In the case of T1, the operating point for the deposition was chosen in the middle of the curve, also called the transition region (i.e. the region between the low and high plasma voltages), as a compromise between the sputtering rate and the oxygen incorporation into the films. It was furthermore expected that at higher oxygen flows, in the poisoned region (high plasma voltage region where the target is oxidized) the films would grow in a V_2O_5 phase, and in the metallic region (low voltage region where the target remains metallic), in the form of the under stoichiometric V_2O_3 phase. In the case of T2 as the avalanche effect from the oxygen poisoning is very fast, an exact and constant value in the transition region could not be stabilized, thus the oxygen flow values were chosen in the vicinity this region. These differences between the two targets arise mainly from their V purities and their geometry i.e. the older target T1 has ridges formed around the region where the sputtering process was more intense.

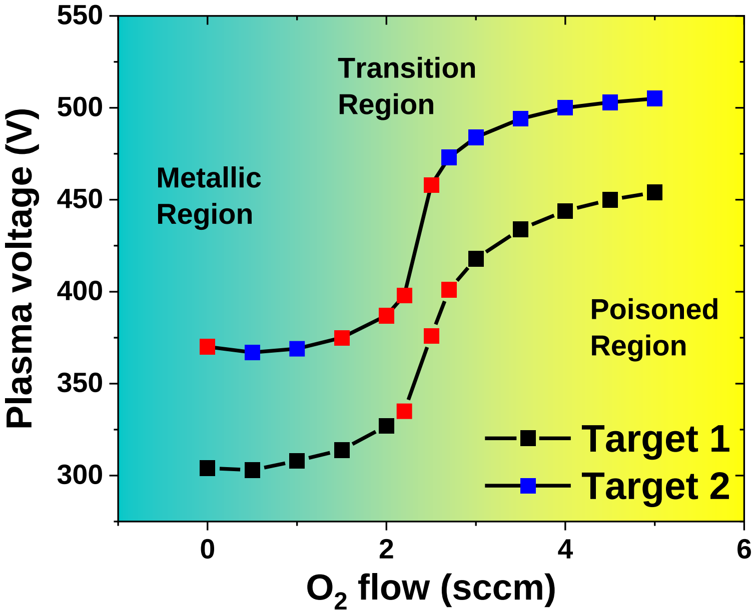

Figure 29. Evolution of plasma voltage during vanadium target sputtering for different oxygen flows in the Ar+O_2 mixture and different targets. Indicated in red are the operation points in the future experiments for T1 and T2.

The oxygen flow during sputtering for T1 was chosen at 2.5 sccm, and slightly offset around this value, at 2.2 and 2.7 sccm O_2, while for T2 the values were chosen as 0, 1.5, 2, 2.2 and 2.5 sccm O_2 in order to fully assess the O_2 influence and to draw the sputtering rate vs oxygen flow curve, presented in Table 1 below. While it is expected that the plasma voltage during deposition will fluctuate around the originally measured ones, in the case of the deposition at 2.2 sccm O_2 from T2, during experiments, the voltage jumped above the transition region, to the beginning of the poisoned region. Although operating in the transition region could be an efficient way for reaching a good oxygen stoichiometry while keeping a high sputtering rate, experiments are not usually possible due to plasma instabilities posing challenges in experiment repeatability. This, however, was not the case for T1, as the plasma seemed to be stable even in the transition region.

A rather simple and preliminary method to check the V-O phases present in the film is their 3visual inspection. When the samples are in a metallic V phase, the films are light gray and very shiny, while the ones in V_2O_3 phase are darker gray, towards black. VO_2 is known to be orange-dark orange colored and V_2O_5 to be yellow-red. Of course, the thickness of the samples plays a key role in their physical appearance. Even though the method can be unreliable, this kind of inspection can provide some quick information on the nature of the films.

Generally, the first measurements performed on the films after the deposition process were the temperature-dependent sheet resistance (R_S) evolution using the 4-point probe method. This was done in order to quickly establish the onset of a temperature-driven insulator-to-metal transition in the films. The results of the measurements, done between room temperature and 95°C, on the films deposited at different O_2 flows from T2 are shown in

Figure 30. As observed in this figure, all the films have similar behavior, except the ones deposited at 2.2 and 2.5 sccm O_2 which indeed exhibit an MIT. The film deposited at 2.5 sccm O_2 has a R_S of 1.12×10^6 Ω/□ at 25°C and of 4×10^4 Ω/□ at 95°C, thus a resistance ratio of one order of magnitude between these two highly resistive states. In the 2.2 sccm O_2 film's case, the ratio between the two states is of two orders of magnitude from a R_S at 25°C of 3.8×103 Ω/□ and at 95°C of 23 Ω/□, both states being relatively metallic.

In the case of T1, all the films exhibit a metallic behavior, indicating the possible synthesis of the under stoichiometric V-O phase V_2O_3. The R_S values being between 30 and 60 Ω/□.

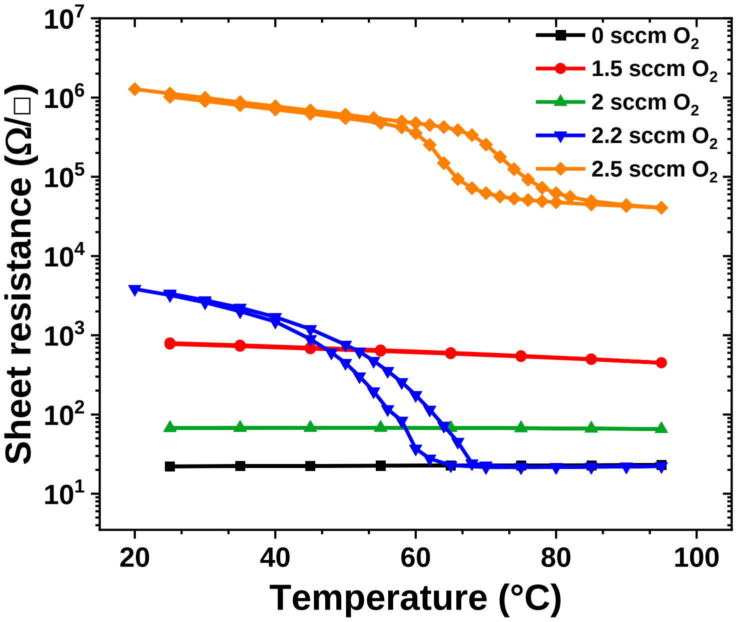

Figure 30. Temperature dependent-electrical measurements of as-deposited V-O films for T2.

Oxygen flow (sccm)	Deposition rate (nm/min)
1.5	13.7
2	12.4
2.2	4.2
2.5	3.5

Table 1. Deposition rate in function of O_2 flow for T2.

Analysis of the film's structural properties using XRD (Figure 31) indicate that for the samples where no MIT is present, from both T1 and T2 , diffraction peaks are present at around ~38.6° and ~83° (except for the sample deposited at 0 sccm O_2 from T2), which could be attributed to the 006 and 0012 reflections of V_2O_3 (PDF 00-034-0187). The peaks at 46.68° and 90.71° corresponding to the 006 and 0012 reflections of sapphire. In the case of the sample deposited at 0 sccm O_2, a relatively broad peak is present at ~41.52° with the full width half maximum

FWHM = 1°. This peak originates from the (110) diffraction plane of the metallic vanadium phase (PDF 00-022-1058).

Let us now discuss the samples exhibiting an MIT deposited from T2 (Figure 31 b)). The sample deposited at 2.2 sccm O_2 flow presents a strong signal coming from the VO_2 (020) planes, although this position is highly shifted from the standard one, with the measured $2\theta_{exp}$ at 40.03° vs the standard $2\theta_{th}$ at 37.797° (PDF 04-007-1466). Finally, the film deposited at 2.5 sccm O_2 flow has diffraction peaks coming from both V_2O_5 and VO_2 phases, indicated by the peaks at ~20.14° and ~41.09° coming from the (001) plane family of V_2O_5 (PDF 04-007-0398), and the ones at 39.81° and ~85.81° from the VO_2 (010) plane family. These results indicate that, upon increasing the O_2 flow in the deposition chamber, the stoichiometry of the deposited film progressively evolves from pure V to V_2O_5, encompassing V_2O_3 and VO_2.

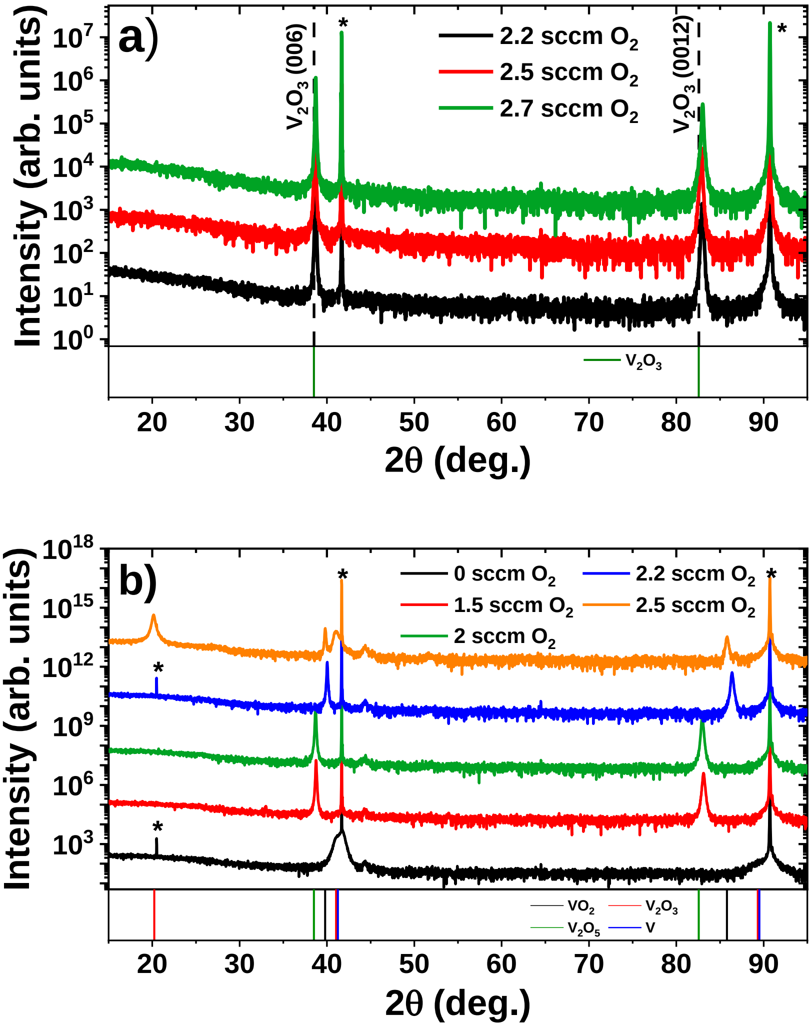

Figure 31. θ-2θ scans of as-deposited films at different temperatures with the lines representing the diffraction positions from different V-O phases from a) T1 and b) T2. Stars represent the sapphire substrate peaks plus the forbidden reflections of sapphire.

In order to confirm that the phase present in the films with diffraction peaks at ~38.6° and 83° is indeed V_2O_3, an electrical 2-point probe measurement was performed down to temperatures of -190°C on the film deposited at 2 sccm O_2 from T2. V_2O_3, similarly to VO_2, exhibits an MIT with the transition temperature around -113°C (160K) [3], thus a transition in the electrical properties should be seen in the as-deposited films as well. The result in Figure 32 presenting the evolution of the 2-point resistance vs temperature shows an abrupt increase in resistance starting at -110°C which continued up to -190°C which is the limit of the recording setup. When decreasing the temperature, a hysteresis can be observed, a feature characteristic of a temperature induced MIT.

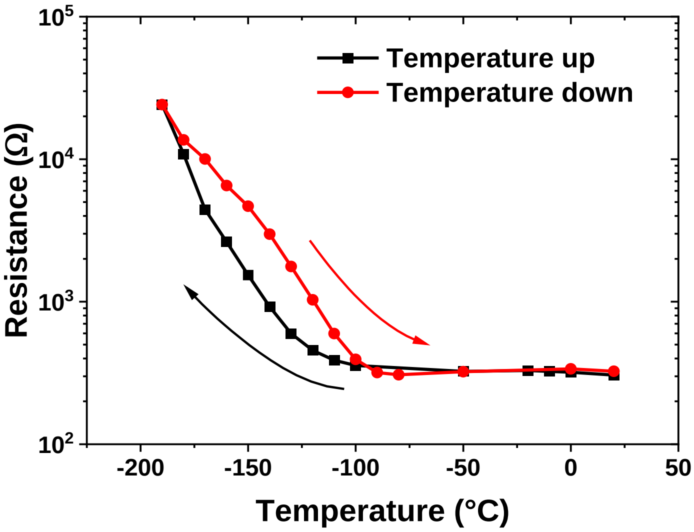

Figure 32. Temperature-dependent resistance evolution of V_2O_3 between 20 and -190°C.

Thus, the as-deposited films crystallize in either the V_2O_3 phase, the VO_2 phase, or in a VO_2/V_2O_5 phase mixture depending on the O_2 flow and overall exhibit poor electrical properties. Therefore, as previously reported [151,163], a subsequent annealing step under oxygen flow was performed to investigate how it would affect the stoichiometry of the deposited films, and whether this could provide an additional mean to control the film properties.

III.1.2. Effect of post-deposition annealing

Based on previous experience of the research group [163], the chosen annealing parameters were initially fixed at 550°C and 20 sccm O_2 flow for a total chamber pressure of ~20 mTorr and 30 minutes annealing time. The annealing was done *in-situ* in the magnetron sputtering chamber. After the samples were cooled down to room-temperature and removed from the annealing chamber, they were measured using the 4-point probe technique. Let us first consider the films grown from the T1 target, with their respective temperature-dependent sheet resistances being presented in Figure 33.

Contrarily to the as grown films showing a metallic-like behavior, all annealed films exhibit a marked MIT. The hysteresis parameters (T_{MIT}, ΔT, ΔH, R_{SM1}/R_{SR} ratio) have been extracted by fitting the curve with a sigmoid function:

$$f(x) = a \times (1 - \tanh\left(\frac{x-b}{c}\right) + d - e \times x \qquad (10)$$

Where a is the amplitude of the transition, b the inflection point, c is the width of the transition, d the vertical offset and e the slope of the transition. From these, the b parameter gives directly the middle points of the heating or cooling curves, respectively, which are also used to calculate the ΔH. The ΔT has been extracted by doing a 2nd order derivative on the curves, as described in Chapter I. The error was estimated from the standard deviation of the fitted parameters, and then the uncertainty propagation formula was performed to get the uncertainty of the extracted parameters.

The hysteresis parameters and are shown in Table 2. The high, state-of-the-art, electrical resistivity change, of more than five orders of magnitude for the film deposited at 2.5 sccm O_2 is indicative of a high-quality film. For the films deposited from T1, all the hysteresis parameters remain broadly similar, with the ΔT and ΔH clearly increasing with increasing oxygen flow during deposition.

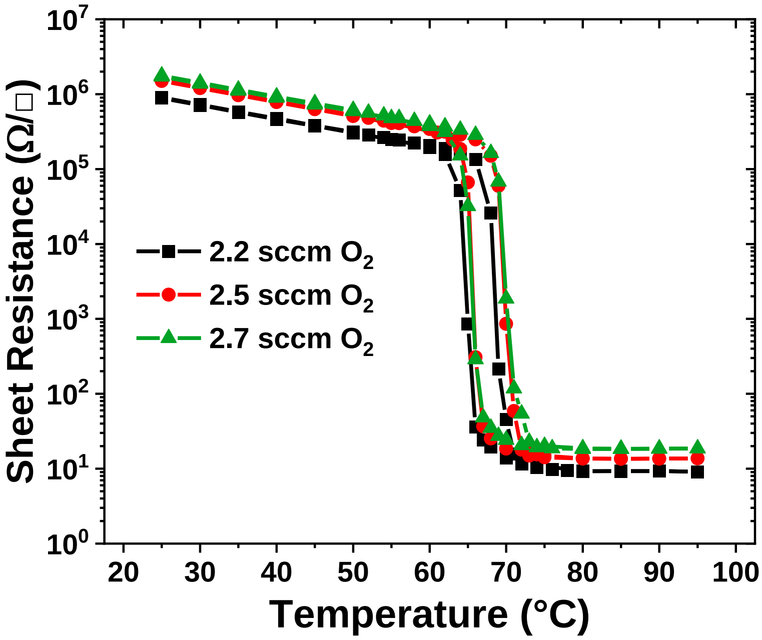

Figure 33. Temperature-dependent R_S evolution of annealed films from T1.

Oxygen flow (sccm)	**T_{MIT} (°C)**	**ΔH (°C)**	**ΔT (°C)**	**$R_{S\ M1}$/ $R_{S\ R}$ ratio**
2.2	66.7 ± 0.1	3.8 ± 0.2	4.9 ± 0.2	9.9×10^4
2.5	67.7 ± 0.1	4.2 ± 0.2	5.3 ± 0.2	1.1×10^5
2.7	67.7 ± 0.1	4.4 ± 0.2	5.9 ± 0.2	9.5×10^4

Table 2. MIT parameters extracted from the hysteresis curves of the annealed films from T1.

Raman spectroscopy measurements performed on the unannealed and the annealed films obtained at 2.5 sccm O_2 from T1 are presented in Figure 34. In the case of the annealed sample, the Raman spectrum is typical of a M1-phase VO_2 [164,165], with peaks identified at ~146, 195, 225, 260, 310, 340, 390, 441, 500, 588, 615, and 663 cm^{-1}. All of the peaks, with the exception of those at 193 and 223 which correspond to the lattice motion involving V-V bonds, are indicative of the vibrational modes of V-O bonds [165]. The large peak at 615 cm^{-1} is a superposition of the 588 and 615 cm^{-1} peaks, which sometimes extends over to the 663 cm^{-1} peak as well [165]. When comparing our measured Raman modes to literature [164], we find that in our sample there are some missing peaks at ~265, 395, 453, 489, 830 cm^{-1} which could result from their overlap with neighboring ones.

These results are in stark contrast with the as-deposited film, for which the features present are: i. a wide peak at around ~220 cm^{-1}, which corresponds to an overlap of an A_{1g} and an E_g symmetry modes, ii. a small peak at ~300 cm^{-1} of E_g symmetry produced from the in-phase movement of vanadium atoms, and iii. a peak at ~500 cm^{-1} which is related to the A_{1g} phonon mode. These peaks are indicative of the V_2O_3 phase [54], and further confirm previous electrical and XRD analysis.

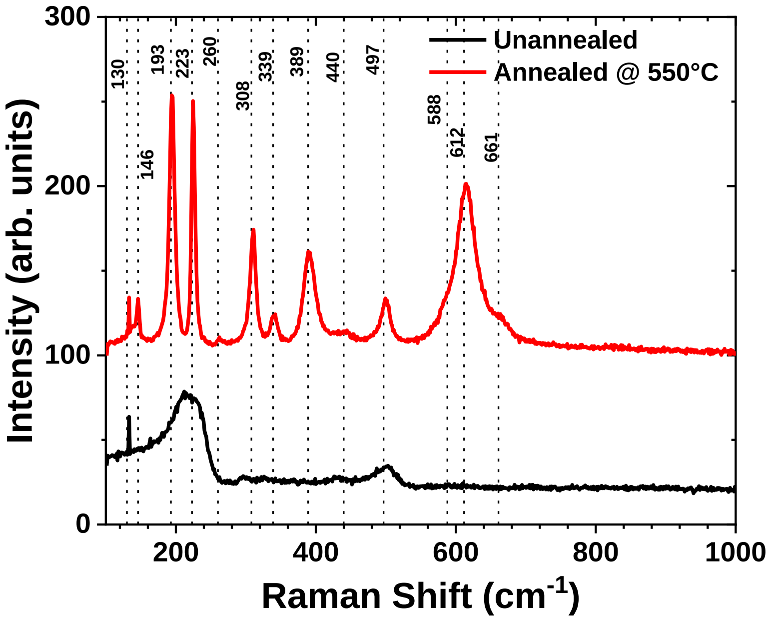

Figure 34. Raman spectra of the annealed and unannealed films deposited at 2.5 sccm O_2 flow from T1.

Let us now consider the samples deposited from T2 which underwent similar post-annealing treatment. The electrical measurements results are presented in Figure 35 with the hysteresis parameters summarized in Table 3. It's clear that annealing has positive effect on all the films and, after this critical step, they present relatively high transition ratios. The only film that doesn't show a huge variation before and after annealing was the one deposited at 2.5 sccm O_2 where the transition sheet resistance varies between 4.4×10^6 Ω/□ and 2.2×10^5 Ω/□, vs. 1.12×10^6 Ω/□ and 4×10^4 Ω/□ before annealing (Figure 30). This could be due to the fact that the film already had a combination of VO_2 and V_2O_5 phases, i.e. it is already oxygen over-stoichiometric so that it can be reasonably assumed that oxygen annealing has no effect in this case. Surprisingly, the film deposited at 0 sccm O_2, thus as-deposited pure vanadium, showed the best after-annealing electrical characteristics from the series, with an R_S ratio between the two states of ~9×10^4. This however is contrasted with the poor optical quality of the film indicating cracks on the surface. Also surprising was the fact that the T_{MIT} of the film deposited at 2.2 sccm, the as-deposited VO_2 (blue curves on Figure 30 and Figure 35), increased from 55.6°C to 76.49°C after annealing. A reason for this increase in T_{MIT} to values higher that the ones expected of VO_2 (67°C) can be attributed to the increase of compressive strain [163], which will be shortly discussed. In the case of the VO_2 films obtained at 1.5 and 2 sccm O_2, thus before the transition region of the poisoning curve, the hysteresis and transition width become smaller at the higher oxygen flow, which could be due to an improved stoichiometry, while the T_{MIT} for the 1.5 sccm O_2 film is closer to the theoretical value of 340K (66.85°C), consistent with the low level of *out-of-plane* strain, discussed in the following part.

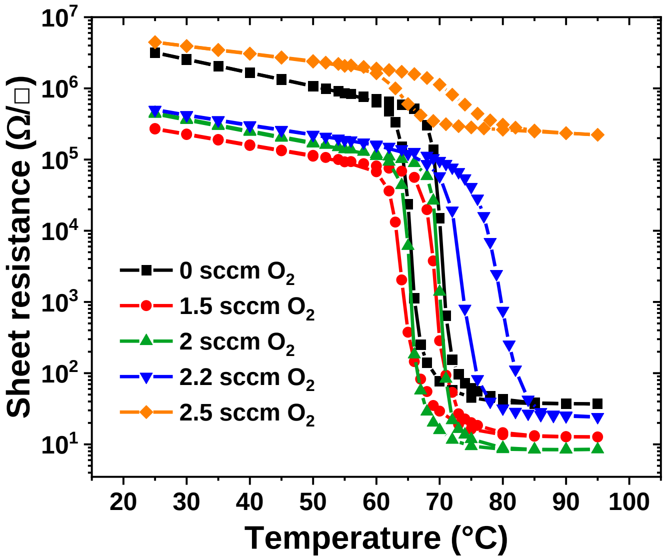

Figure 35. Electrical hysteresis of annealed films deposited from T2

Oxygen flow (sccm)	T_{MIT} (°C)	ΔH (°C)	ΔT (°C)	$R_{S\,M1}$/ $R_{S\,R}$ ratio
0	68.1 ± 0.1	4.3 ± 0.2	6.9 ± 0.2	8.5×10^4
1.5	66.9 ± 0.1	5.1 ± 0.3	7.9 ± 0.3	2.1×10^4
2	67.8 ± 0.1	4.6 ± 0.2	6.2 ± 0.2	5.3×10^4
2.2	76.3 ± 0.1	5.7 ± 0.2	9.5 ± 0.2	2×10^4
2.5	68.3 ± 0.3	9.4± 0.7	14.5 ± 0.7	2×10^1

Table 3. MIT parameters extracted from the hysteresis curves of the films obtained from T2

The θ-2θ XRD scans shown in Figure 36 a) reveal that after annealing, all the films present diffractions peaks corresponding solely to the VO_2 phase, with the exception of the sample obtained from 2.5 sccm O_2. This supports the speculation, made in the electrical properties discussion, about the nature of the film. The θ-2θ scans also reveal that in the case of the 2.2 sccm O_2 film, the (020) reflection is heavily shifted towards higher angles when compared to the theoretical position, corresponding to a compressive strain of $e_{zz} = -0.56\%$, which can explain the increased T_{MIT}.

The value of the *out-of-plane* strain e_{zz} is computed from:

$$e_{zz} = \frac{(b - b_{th})}{b_{th}} \qquad (11)$$

Where b is the lattice parameter of VO_2, b = $2d_{020}$, d_{020} being directly obtained from Bragg's law. The *out-of-plane* strain quantifies the deviation of the lattice parameter from its theoretical value b_{th}. "zz" indicates that this strain corresponds to the third diagonal component of the strain tensor. The z-axis is perpendicular to the surface, while the x-axis lies in the surface of the film in the direction of the X-ray beam.It is worth mentioning that this high strain can be attributed to the film's lower thickness (~124 nm) which is due to the operating point of the sputtering, positioned in the poisoned region of the plasma voltage vs. O_2 flow curve (Figure 29). This compressive strain is due the thermal expansion mismatch between the VO_2 and the Al_2O_3 substrate and accounts for the shift in the MIT [163]. Similar levels of strain have been observed in ~100 nm thick films grown on sapphire [163], these strain values are rapidly dropping for films with thicknesses above 200 nm, hence the values close to the theoretical 67°C observed for all other films.

ω-scans recorded from on the (020) lattice planes of VO_2 are represented in Figure 36 b). These scans reveal that the films deposited in the metallic region (of the plasma voltage vs. O_2 flow curve of the target, < 2 sccm) have increasingly sharper peaks as the O_2 flow during sputtering is getting closer to 2 sccm O_2. The ω-scan curve of the sample deposited at 0 sccm O_2 has a FWHM = 1.64° which is indicative of a high level of disorder. The FWHM decreases to 0.59° and 0.47° for the films obtained from 1.5 and 2 sccm O_2, respectively, indicating an improvement of the crystalline quality. As in the case for its electrical behavior (Figure 35 and Table 3), the film grown at 2.2 sccm O_2 exhibits a peculiar behavior, where the ω-scan has a two component peak profile which is frequently observed in epitaxial thin films [166], including VO_2 films [143]. In short, the narrow peak arises from the long-range order characteristic of high-quality crystalline materials, while the broader one from the short-range correlations in the defect structure (i.e. mosaicity). This shape is not straightforwardly observed for the other, thicker films because of their lower level of strain: strain relaxation induces defects in the material that lower the intensity of the superposed narrow peak. A narrow peak's presence can nonetheless be suspected in the film obtained from 2 sccm O_2, also indicating a good crystalline quality for this film. Finally, the FWHM of the film prepared under 2.5 sccm O_2 is very large (0.78°) and with a very weak intensity, indicating that the presence of V_2O_5 in the film significantly degrades the crystalline quality, hence its degraded electrical properties.

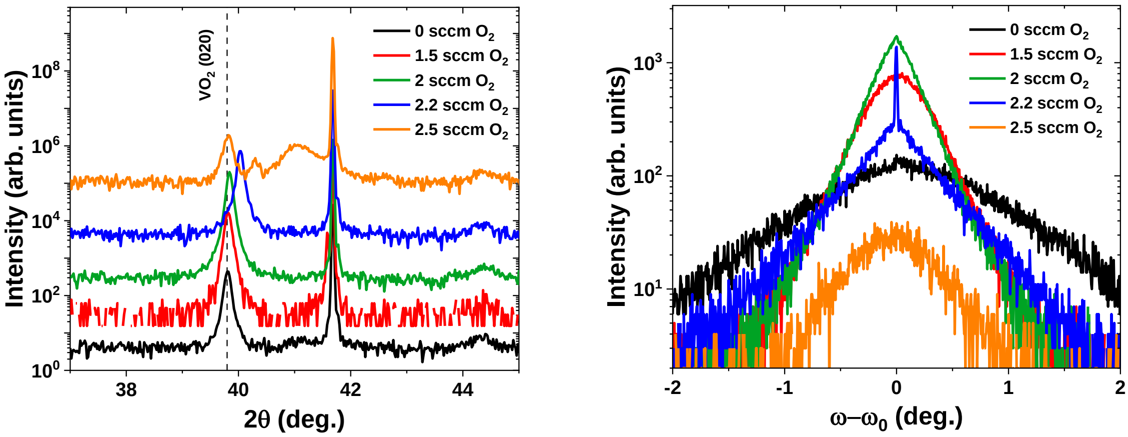

Figure 36. XRD measurements of annealed T1 films a) θ-2θ scan b) ω-scan.

The thicknesses, strain values and full width half maximum values obtained from the ω-scans corresponding to the depositions at the different O_2 flows are shown in Table 4. The small fractional uncertainties are mostly < ± 0.01 and are due to the XRD scans having low noise, allowing for a good data fit.

Oxygen flow (sccm)	Thickness (nm)	Out-of-plane strain (%)	FWHM - broad peak
0	70	-0.02	1.64
1.5	412	-0.04	0.59
2	373	-0.08	0.47
2.2	124	-0.56	1.13
2.5	105	-0.02	0.78

Table 4. Thickness and *out-of-plane* strain values for the sample fabricated at different oxygen flows.

III.1.3. Epitaxial orientation and structural phase transition

The scans θ-2θ above demonstrate that the (010) planes of VO_2 are parallel to the (001) planes of sapphire. The *in-plane* orientation of the vanadium dioxide films was determined using φ-scans. Figure 37 shows a) the θ-2θ and b) the φ-scan of the annealed sample deposited at 500°C at 2.5 sccm O_2. The data shown here correspond to a film grown from the T1 target, but, upon inspection, all films exhibit the same orientations. For φ angles between -180° and +180°, the (220) VO_2 plane appears six times, indicating that the vanadium dioxide has a six-fold symmetry instead of the two-fold symmetry as expected for a monoclinic structure. This difference is a well-known phenomenon caused by the presence of three structurally identical possible orientations of the (010) planes relative to the (001) planes of sapphire, which results in the development of three epitaxial variants in the plane. In addition, it is observed in the φ-scans that the diffraction peaks are double-split, with peaks separated by approximatively ±2.6°. This is because of an angle mismatch between the β angle of VO_2 (122.6°) and the γ angle of Al_2O_3 (120°), which was already observed for this system [163]. In short, the epitaxial relations are as follows: [100]VO_2 || [210]Al_2O_3 , [100]VO_2 || [-110]Al_2O_3, and [100]VO_2 || [120]Al_2O_3. This is consistent with the results from the literature presented in details in Chapter I.

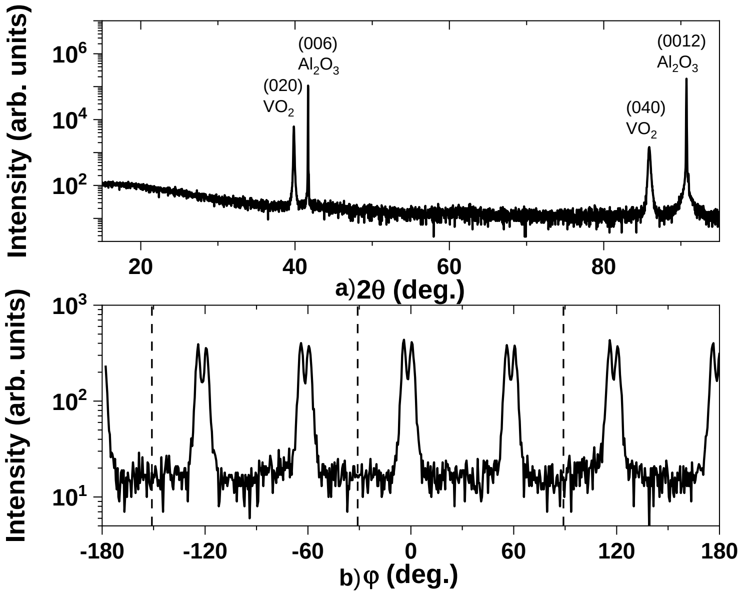

Figure 37. a) θ-2θ scan of a film deposited from T1 at 2.5 sccm O_2, 500°C and annealed at 550°C b) φ-scan of same film recorded for the (220) planes of VO_2. The dotted lined indicate the (104) peak positions of sapphire.

The temperature-dependent structural phase transition of the annealed sample obtained at 2.5 sccm O_2 from T1 was also measured. This was done by mounting the sample on the XRD heating stage in order to perform a θ-2θ scan for every 2°C between 44 and 90°C. The results are presented in Figure 38 and show the rather abrupt nature of the M1 to R transition and the stabilization of the R phase starting from 68°C.

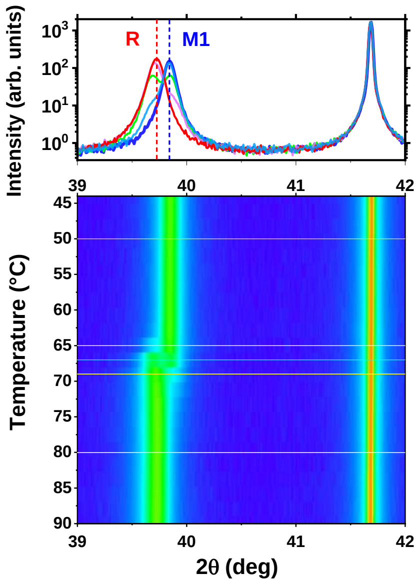

Figure 38. XRD intensity-temperature mapping and extracted θ-2θ scans demonstrating the M1-to-R phase shift of the (020) VO_2 peak as temperature increases.

In order to test the stability in time, an important feature for a practical use of the VO_2 layers, repeated thermal cycles of heating and cooling have been applied on a VO_2 film obtained at 500°C deposition and 550°C annealing temperatures from T1. A two-probe configuration was used to measures the resistance of the film. The measurements were performed by periodically ramping up and down the temperature in the 30-100°C range with heating/cooling rates of 10°C/min for 25 cycles, and with rates of 20°C/min for more than 60 cycles. Figure 39 shows the evolution of the film's surface resistance with time. The measurements indicate that no significant degradation of the electrical properties of the layer throughout the temperature cycling occurs. The film presents as-well an excellent stability for repeated thermal activation between the two states of the VO_2.

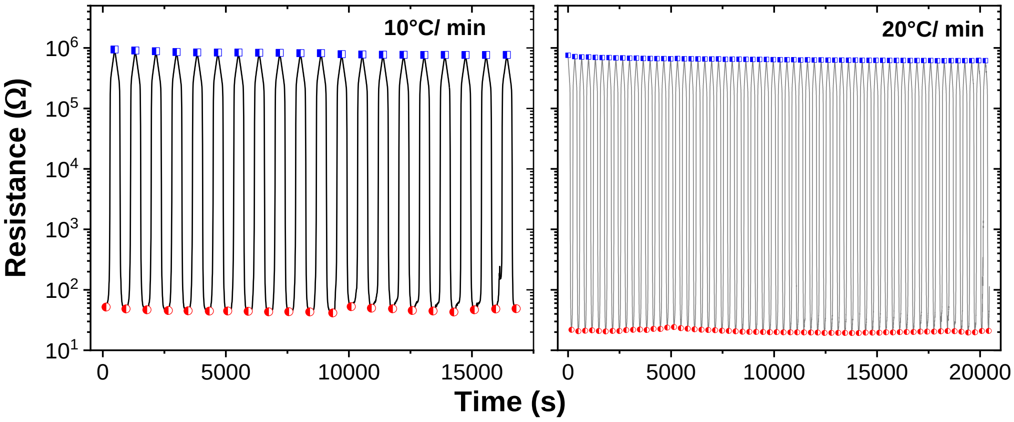

Figure 39. Time-dependent VO_2 layer surface resistance evolution for multiple thermal cycles with 10°C/min and 20°C/min rates.

III.2. Influence of deposition parameters on the characteristics of VO_2 layers

This section describes the effects of varying deposition and annealing conditions on the electrical and structural properties of the films. In order to simplify the discussion, the deposition at 500°C and 2.5 sccm O_2 will be referred to as "standard" deposition conditions. The annealing at 550°C, 20 sccm O_2 at 20 mTorr chamber pressure and for a time of 30 minutes will be called hereafter a "standard" annealing. As the highest MIT resistivity ratio was obtained from T1 at 2.5 sccm O_2 with a deposition temperature of 500°C and an annealing temperature of 550°C, the following discussion will focus on samples obtained from T1.

III.2.1. Influence of thickness on the VO_2 thin films' structural and electrical characteristics

In order to assess the influence of the films' thicknesses on their performances, samples have been fabricated at 10-, 20- and 30-minutes deposition time using the standard methods of deposition and annealing. The targeted thicknesses were > 50 nm, mainly to decrease the influence of the strain coming from substrate-film interface. The effects of lower thicknesses has already been studied in the research group using e-beam sputtering [150] and it was found that as thicknesses increases in the range 15-300 nm, strain relaxation increases (i.e. the strain is decreasing) which in turn results shifts the MIT temperature towards the theoretical 67°C value. Additionally, the decrease in defect density (which are mainly located at the interface) induces a decrease in ΔT and an increase in resistivity in the insulating state, consequent to a reduction of defect states in the band gap. In our case, the final thicknesses of the films grown during 10, 20 and 30 min were 61, 85 and 169 nm, respectively, with the related deposition rates of 6.14, 4.24 and 5.62 nm/min. The discrepancies in the deposition rates are induced, most probably, by plasma instabilities during the sputtering process.

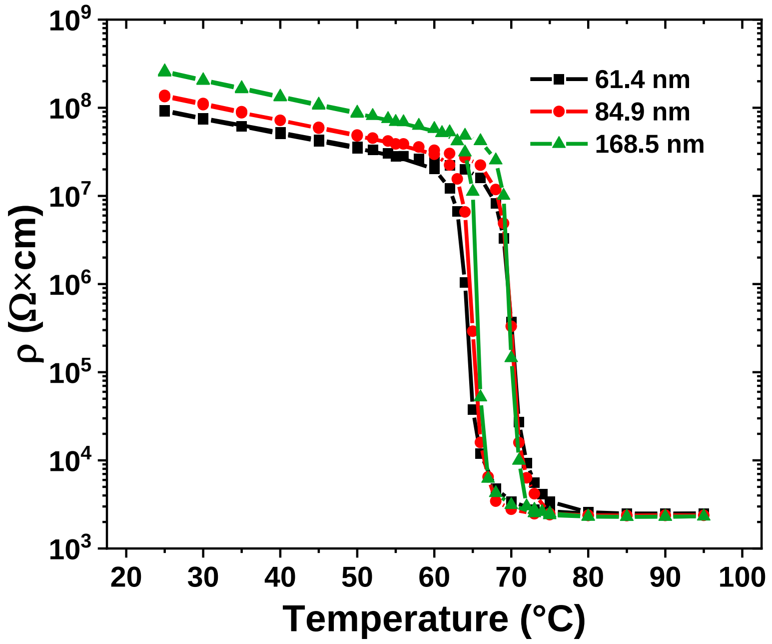

Figure 40. MIT hysteresis of the temperature-dependent resistivity evolution in VO_2 films with different thickness.

Thickness (nm)	**T_{MIT} (°C)**	**ΔH (°C)**	**ΔT (°C)**	**ρ_{M1}/ρ_R resistivity ratio**
61	67.2 ± 0.1	5.8 ± 0.2	7.7 ± 0.2	3.7×10^4
85	67.5 ± 0.1	5.0 ± 0.2	6.6 ± 0.2	5.8×10^4
169	67.7 ± 0.1	4.2 ± 0.2	5.3 ± 0.2	1.1×10^5

Table 5. MIT hysteresis parameters of the films deposited at different thicknesses.

Four-point probe temperature-dependent electric measurements reveal hysteresis curves (presented in Figure 40), with rather small variations between the T_{MIT}, ΔT and ΔH. The parameters of these curves, as extracted in Table 5 evolve progressively with increasing thickness, with the T_{MIT} and resistivity ratios increasing with thickness, which is due to a lowering of the thermal strain at higher thicknesses, as already observed in [163] and [122]. We have plotted the resistivity in order to eliminate the R_S dependency on thickness. The hysteresis width and transition width also decrease, which was expected due to research done in earlier work [163]. For the film with thickness of 169 nm, the T_{MIT}, ΔT, ΔH and MIT resistivity ratios reach excellent values, with a low transition and hysteresis width and more than five orders of magnitude between ρ_{M1} and ρ_R. As the ratio is already higher than five orders of magnitude, it can be concluded that for an even greater thickness the electrical performances would not largely improve.

XRD θ-2θ scans (Figure 41) and Raman spectroscopy (Figure 42) reveal also high similarity between the characteristics of each samples. For XRD, the 020 peaks show similar position, with increasing intensity due the increased thickness. ω-scans also, unsurprisingly, exhibit increasing intensity and a lowering of the broad peak's FWHM (0.45°, 0.37° and 0.33°) as a result of the decrease in defect density. In the case of the Raman scans, the increased thickness leads again to higher intensity peaks, their position remaining unchanged.

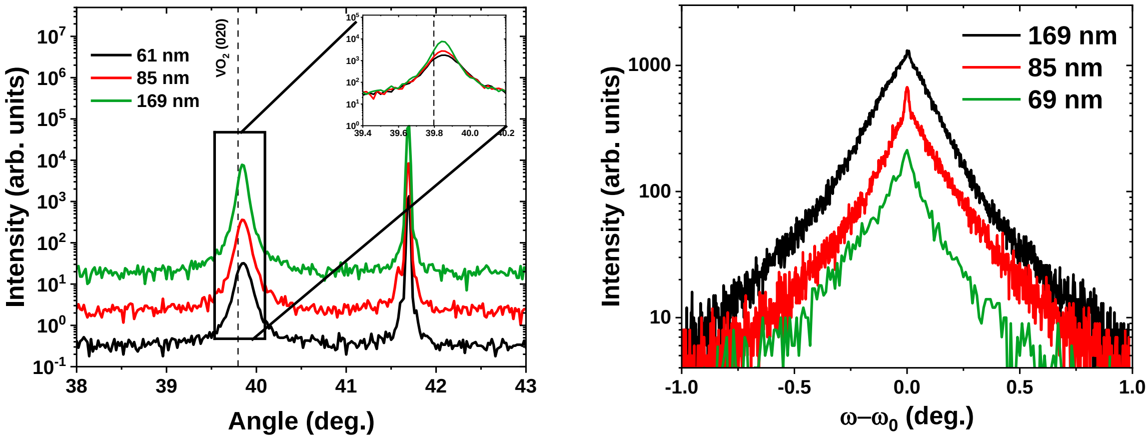

Figure 41. XRD scans of VO_2 films with different thicknesses a) θ-2θ scan of samples a different thickness, inset is zoom on the position of the 020 VO_2 peak with dashed line being the theoretical position of the peak, and b) ω-scan on the (020) peak.

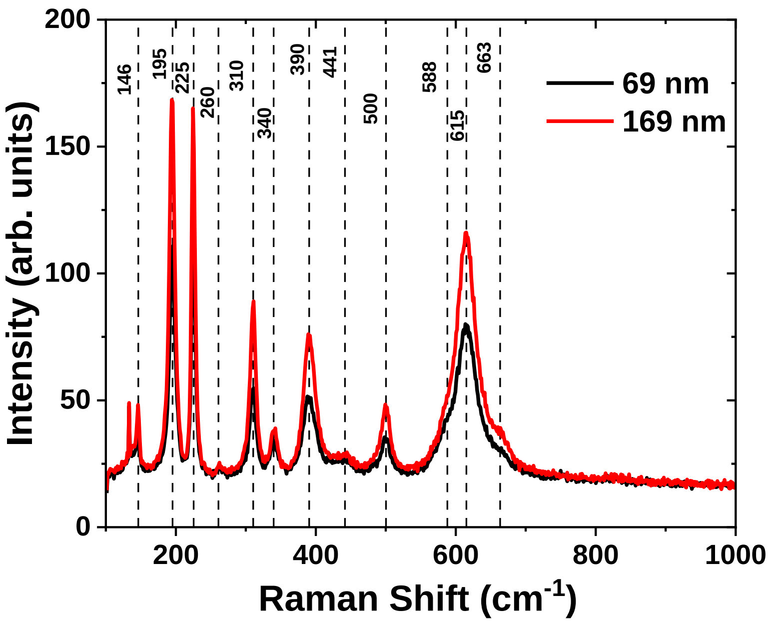

Figure 42. Raman spectroscopy results for VO_2 films of different thicknesses.

III.2.2. Deposition temperature influence on the characteristics of VO_2 layers

The first deposition parameter we investigated was the deposition temperature. We analyzed samples obtained from T1 at room temperature (RT), 150°C, 400°C, 500°C and 600°C, obtained at 2.5 sccm O_2 and with standard post-deposition annealing for all of them. The electrical characteristics of the samples are displayed in Figure 43 and the hysteresis parameters of their MIT are summarized in Table 6. The films obtained at RT and 150°C show lower resistance ratios between the two thermally-triggered MIT states and larger ΔT and ΔH values, which could be an indication of strain, phase mixture or lower film stoichiometry. The films deposited above 400°C have hysteresis curves that more or less super-impose, with only slight differences between their parameters, of less than 1°C. For the films obtained at 500 and 600°C, the differences in the hysteresis parameters are almost imperceptible. This shows, at least from the electrical performances point of view, that increasing the temperature over 400°C does not influence any more the films' performances.

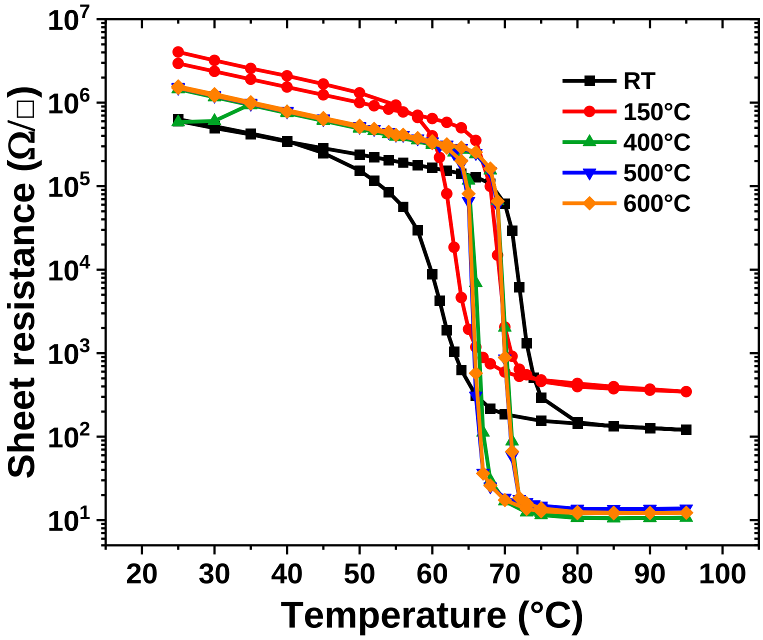

Figure 43. Temperature-dependent sheet resistance measurements of films deposited at different substrate temperatures.

Substrate temperature (°C)	**T_{MIT} (°C)**	**ΔH (°C)**	**ΔT (°C)**	**$R_{S\ M1}$/ $R_{S\ R}$ ratio**
0	66.2 ± 0.3	11.9 ± 0.6	15.9 ± 0.6	8.5×10^3
150	65.8 ± 0.1	6.2 ± 0.3	8.6 ± 0.3	5×10^3
400	68.1 ± 0.1	3.8 ± 0.2	5.3 ± 0.2	1.4×10^5
500	67.7 ± 0.1	4.2 ± 0.2	5.3 ± 0.2	1.1×10^5
600	67.8 ± 0.1	4.1 ± 0.2	5.4 ± 0.2	1.3×10^5

Table 6. MIT hysteresis parameters of the films deposited at different substrate temperatures.

The θ-2θ XRD scans (Figure 44 a)) of the same samples reveal that for films obtained at RT and 150°C, diffractions peaks appear at 27.88° and 39.76°, coming from the VO_2 (011) and (020) planes, respectively. Additionally, for the RT samples we noticed additional peaks at ~20.19° and ~41.08°, which come from the (010) and (020) reflections of V_2O_5, and a peak at 24.49°, from the (012) reflection of V_2O_3. Even though all the films were obtained using the same oxygen flow, a lower adatom mobility that is related to the decrease of substrate temperature can lead to inhomogeneous incorporation of O_2 and random orientations of the films [167]. On the other hand, besides the increased atom mobility, a higher substrate temperature favors the layer crystallization by reducing the concentration of defects [167].

The θ-2θ scans of the samples deposited at 400, 500 and 600°C reveal that each of the films present a VO_2 phase with a single (010) plane orientation. This, combined with the highly similar ω-scans in Figure 44 b), further supports the electrical measurements data, indicating that from 400 to 600°C, the characteristics of the films do not evolve much. Note that in the ω-scans the difference in intensities between the film deposited at 400/600°C and 500°C arise from different x-ray beam intensities exiting the x-ray generator. The *out-of-plane* strain (Table 7) is as well very similar, with $e_{zz} = -0.09\%$ (compressive strain) for the 400 and 600°C samples and -0.11% for the sample at 500°C, the difference coming possibly from the sample thickness difference (sample fabricated at 500°C is 169 nm while the 400°C one is 280 nm and the one at 600°C is 231 nm). In the case of the sample deposited at 150°C the strain is $+0.08\%$. The occurrence of tensile strain can be attributed to the existence of oxygen vacancies which are known to increase the lattice parameters of VO_2 [168].

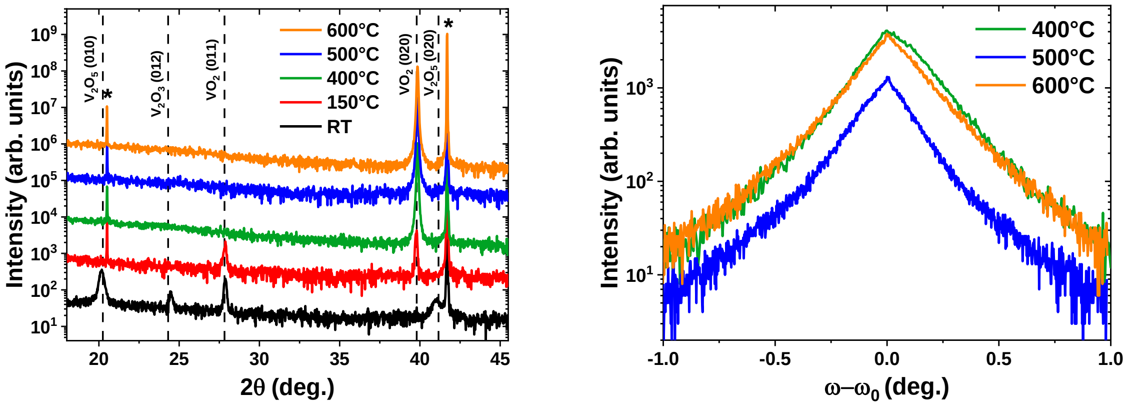

a)

b)

Figure 44. XRD measurements of samples obtained at different temperatures a) θ-2θ scans and b) ω-scans. Stars represent the peaks coming from the sapphire substrate plus the forbidden sapphire reflections.

Morphological measurements performed using AFM show that increasing the deposition temperature from room temperature to 400°C leads to an average films' grain length (AGL) increase from 140 nm to 223 nm on the 2×2 µm² scans (Figure 45). Further increase of temperature to 500°C does not lead to larger grains, as the AGL decreases to 207 nm for that temperature. These changes are however relatively small and would not be very significant in impacting the ΔT and ΔH. Moreover, the root mean square height Sq (measurement of the area roughness, equivalent to the standard deviations of the heights) for scan areas of 2×2 µm² increases from 9.8 nm for the sample obtained at RT to 12.2 nm for the sample obtained at 400°C, finally decreasing to 8.94 nm for the one obtained at 500°C. The values of the strain and the AGL for the different deposition temperatures are summarized in Table 7.

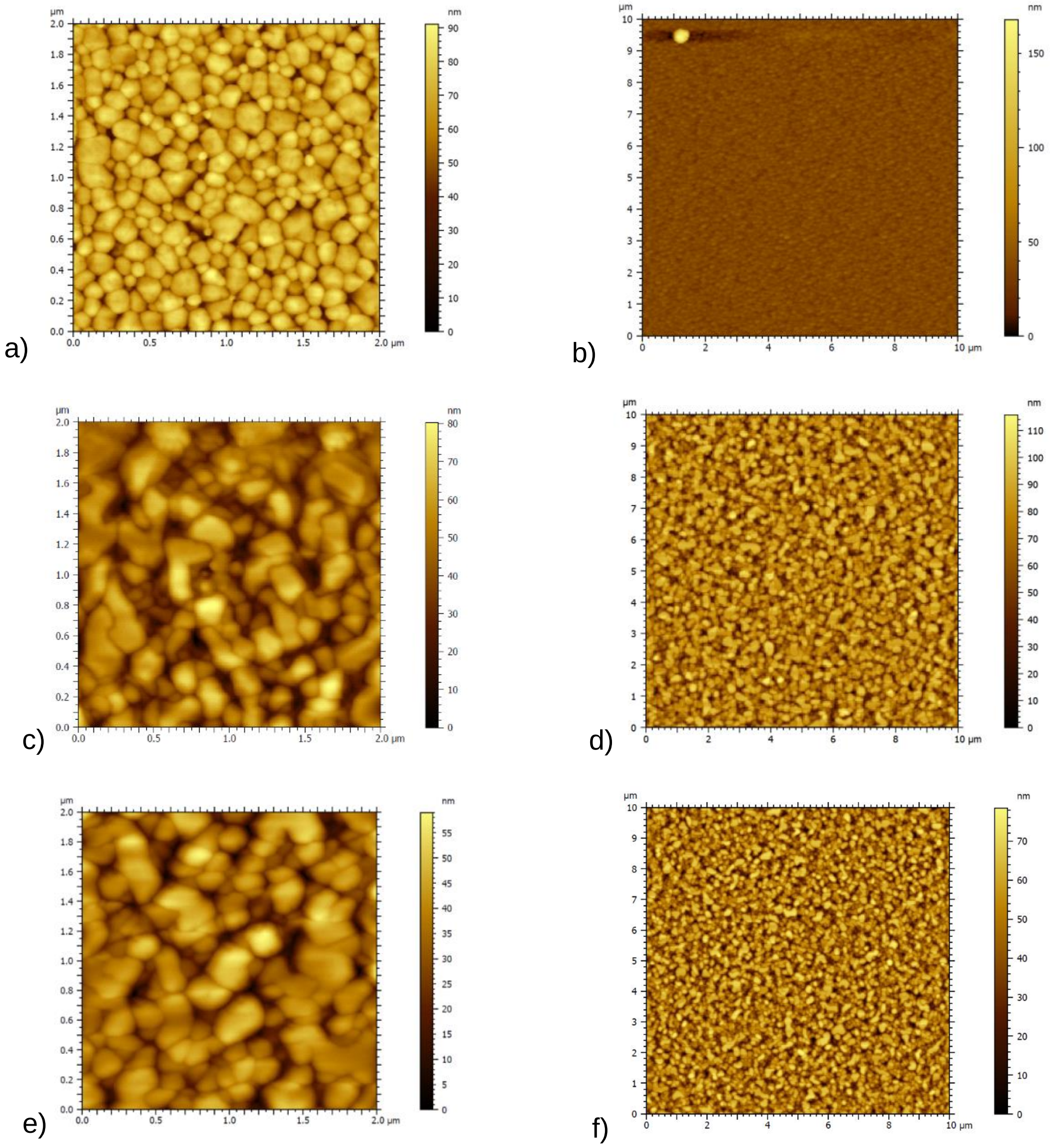

Figure 45. AFM scans for films deposited at RT a) 2x2 μm² b) 10x10 μm² areas, at 400°C c) 2x2 μm² d) 10x10 μm² areas and at 500°C e) 2x2 μm² f) 10x10 μm² areas.

Deposition temperature (°C)	***Out-of-plane* strain (%)**	**Average grain length (nm)**
RT	-	140 ± 42
150	+0.08	-
400	-0.09	223 ± 94
500	-0.11	207 ± 76
600	-0.09	-

Table 7. Strain and average grain sizes for samples fabricated at different temperatures.

III.3. Influence of annealing parameters

After assessing the influence of the deposition parameters on the films, we evaluated the influence of the annealing parameters on the VO_2 films' performances. So far, the standard annealing procedure used in order to obtain high quality VO_2 films was 550°C at 20 sccm O_2, and 20 mTorr total pressure, for a total time of 30 minutes, therefore, different annealing times, temperatures and pressures were evaluated. As per the previous chapter, T1 is the target used for the film fabrication.

III.3.1. Annealing temperature influence

In order to explore the impact of temperature during annealing we investigated the properties of films obtained with the standard method and annealed at values of 450, 550 and 650°C. As already established, without any annealing, the films crystallize in a V_2O_3 phase that has an MIT starting at around -110°C. To transform the films into the VO_2 phase, an annealing at 550°C in oxygen atmosphere was required, which has yielded very good structural and electrical results. Decreasing this temperature to 450°C reveals, from the 4-point probe measurements (Figure 46, red curve), a very weak transition, with an electrical resistivity amplitude change of less than one order of magnitude. From the XRD θ-2θ scans (Figure 47 a)) we can infer that, most likely, this is due to the co-existence of the V_2O_3 and VO_2 phases. Increasing the annealing temperatures to 550 and 650°C results in films that are fully oxidized towards the VO_2 phase and present five orders of magnitude in the resistivity change from RT to 95°C, from the insulating to the metallic phase. Although the curves are visually almost identical, the transition width is slightly higher for the film annealed at 650°C, possibly from an increase in structural defects, as seen in the ω-scans in Figure 47 b), combined with grain coalescence, which will be further discussed.

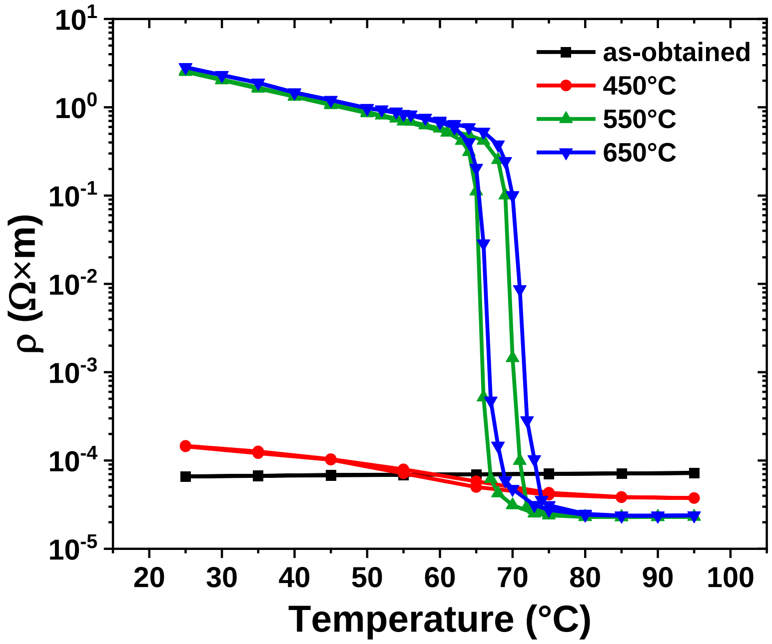

Figure 46. Electrical hysteresis of as obtained and annealed at 450, 550 and 650°C VO_2 films in O_2 atmosphere at 20 mTorr.

Rocking curve scans (Figure 47 b)) of the samples show that annealing at 450°C results in a broad peak with a full width half maximum FWHM = 0.8°, which is indicative of a high level of disorder. For the sample at 550°C a narrow peak appears in the middle of the rocking curve together with a narrowing of the broader peak (FWHM = 0.26°). At 650°C the central peak is still visible while the diffuse peak is widening (FWHM = 0.9°) indicating an increased mosaicity. The calculated e_{zz} strain evolves from -0.33% at 450°C to -0.11% at 550°C and finally to -0.12% at 650°C. From a structural point of view, the annealing at 550°C seems to be the optimal one.

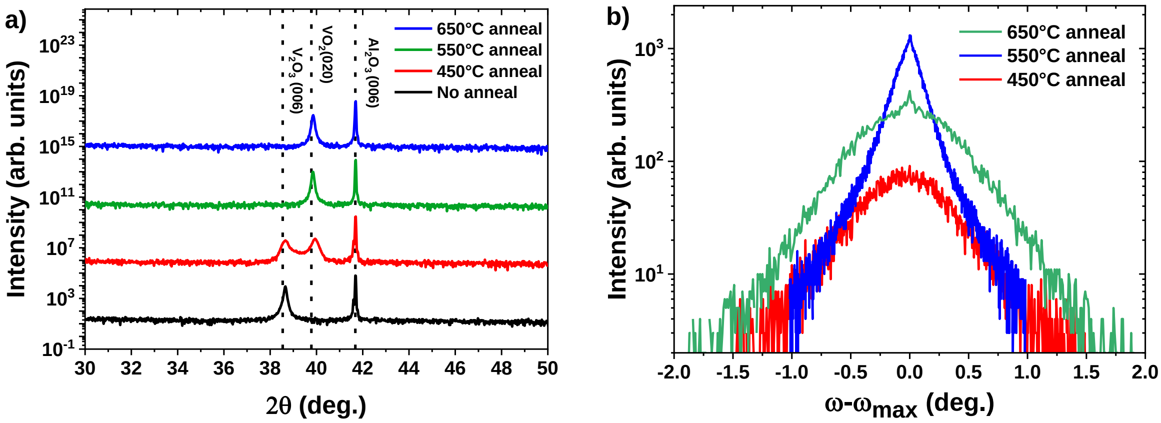

Figure 47. XRD scans of films annealed at different temperatures a) θ-2θ scan b) ω-scan.

AFM measurements (Figure 48) show that increasing the annealing temperature also increases the roughness of the films, with Sq = 8.94 for the films annealed at 550°C, and Sq = 11.2 nm for the films annealed at 650°C (data extracted from the on the 2×2 μm² scans). The AGL of the films remains mostly the same with 207 ± 76 nm for the 550°C and 201 ± 76 nm for the 650°C. The small AGL and strain difference between the films annealed at 550° and 650°C (summarized in Table 8) is reflected in the similar hysteresis curves.

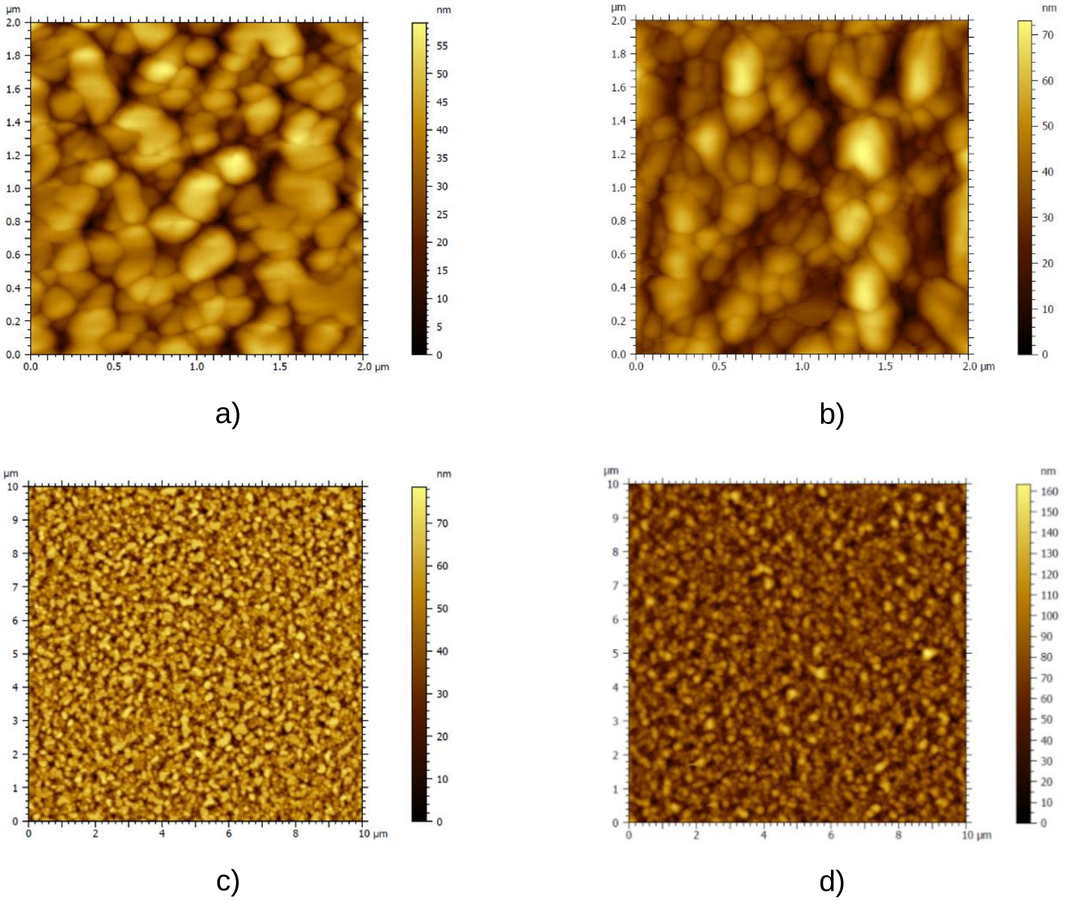

a)

b)

c)

d)

Figure 48. AFM scans for the films annealed at 550°C on a) 2x2 μm^2 and b) 10x10 μm^2 areas, and annealed at 650°C on c) 2x2 μm^2 and d) 10x10 μm^2 areas.

Annealing temperature (°C)	***Out-of-plane* strain (%)**	**Average grain length @ 2x2 μm^2 (nm)**
450	-0.33	-
550	-0.11	207 ± 76
650	-0.12	201 ± 76

Table 8. *Out-of-plane* strain and AGL of films annealed at different temperatures.

Raman spectra of the samples reveal that for the film annealed at 450°C all the peaks show highly decreased intensities coming from the insulating M1 phase of VO_2 and completely missing the peaks attributed to the B_g mode at 146 and 260 cm^{-1}, which can be linked to the reduced amount of VO_2 phase in the film. For the film annealed at 650°C there are some particular features which distinguish it from the standard annealing such as the separation of the peaks at 392 and 295 cm^{-1} and of the peaks at 588 and 612 cm^{-1}, this being mainly due to the redshift of the peak at 612 cm^{-1}. The wavenumbers associated with these peaks primarily correspond to the vibrations of oxygen bonds that link vanadium chains along the c-axis of the crystal structure and are directly proportional to the reduced masses of the oxygen and vanadium atoms [165]. Furthermore, an appearance of a broad peak at 130 cm^{-1} is observed, which could possibly come from an A_g phonon mode of VO_2 (M1) phase, indicated also by the appearance of a small peak at 830 cm^{-1} belonging to the B_g symmetry [54].

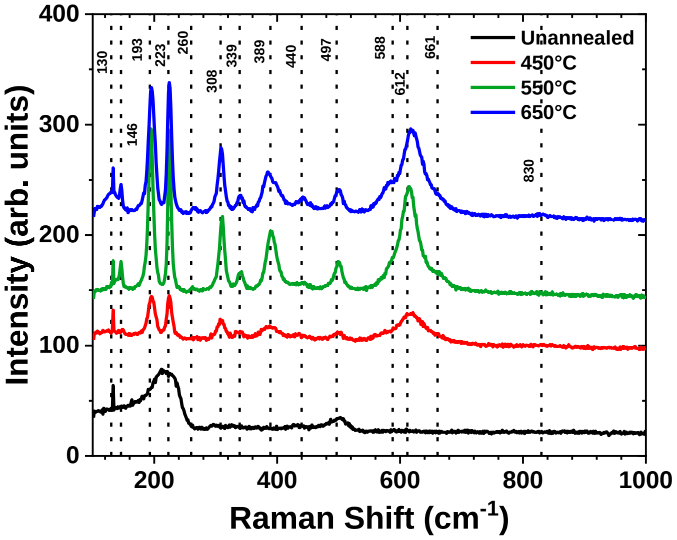

Figure 49. Raman spectra of VO_2 films annealed at different temperatures.

Furthermore, films deposited in different conditions (*i.e.* at 500°C for oxygen flows of 2.2 and 2.7 sccm O_2, and at 400 and 600°C for 2.5 sccm O_2 flows) were annealed at even higher temperatures, of 750°C. The XRD ω-scans (Figure 50 a)) for these films showed peculiar shapes, with a narrow peak superimposed with a broad peak, or replaced by two satellites separated by a dip in intensity (black curve in Figure 50 a)). These features have been already observed in epitaxial systems and are related to misfit dislocations generated at the film-substrate interface [169].

As mentioned before, in the ω-scans, the narrow peak is linked to the long-range order present in the films, and the broad peak is linked the short-range correlations in the defect structure. The presence of the satellites has been ascribed to the presence of periodic misfit dislocation arrays lying at the interface [169,170]. Combining the rocking curves with the azimuthal scans, we can plot the intensity distribution in the in-plane (Q_x, Q_y) planes, which is represented in Figure 50 b)). This mapping was done by performing an ω-scan, and rotating the sample around the azimuth by 2° from 0° to 180°. The results indicate a flower-like pattern which is linked to the appearance and expansion of the shoulders during the scans, which have a 60° periodicity. More research is needed in order to fully understand the appearance of these dislocations, as usually they are created during the growth process [169,170], while in our case they appear after a post-annealing step.

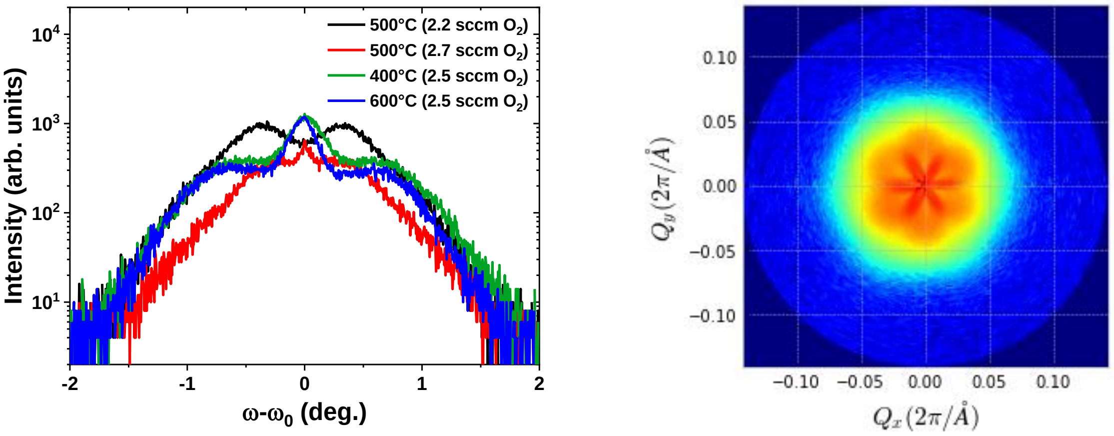

Figure 50. a) Films annealed at 750°C b) Q_x vs Q_y map of film deposited at 400°C, 2.5 sccm O_2 and annealed at 750°C. In a) the difference in peak shape is most likely related to the different positions of the sample on the sample stage. Indeed, before discovering this azimuthal anisotropy, no particular area was given to the azimuthal orientation of the sample prior measurement.

III.3.2. Influence of the chamber pressure during annealing on the VO_2 films

Additional investigations were conducted to evaluate the impact of chamber total pressure during annealing, where the experiments were carried out using three different pressure values: 6 mTorr, 20 mTorr (standard annealing), and 40 mTorr, all performed under an oxygen flow of 20 sccm O_2 and for samples obtained in standard deposition conditions.

The values of the measured electrical parameters extracted from the hysteresis curves (Figure 51) alongside their differences compared to the 20 mTorr O_2 annealing are presented in Table 9. It is observed that the T_{MIT}, ΔH, and ΔT decrease as the annealing pressure increases. Conversely, the resistance ratios show an increase, with the most significant change occurring between the annealing pressures of 6 and 20 mTorr. Between 20 and 40 mTorr the resistance ratios are very similar. The decrease of the ratio for the films annealed at 6 mTorr is mostly due to a lower resistance in the insulating state, from 1.5×10^6 Ω/□ at 25°C for the 20 mTorr annealed sample to 0.3×10^6 Ω/□ at 25°C for the 6 mTorr annealed one. Higher chamber pressures during annealing (e.g. 40 mTorr) seem to lead to better films in terms of resistance change between the insulating and metallic states, with the difference in magnitude between the 40 and 20 mTorr films being of 1×10^4.

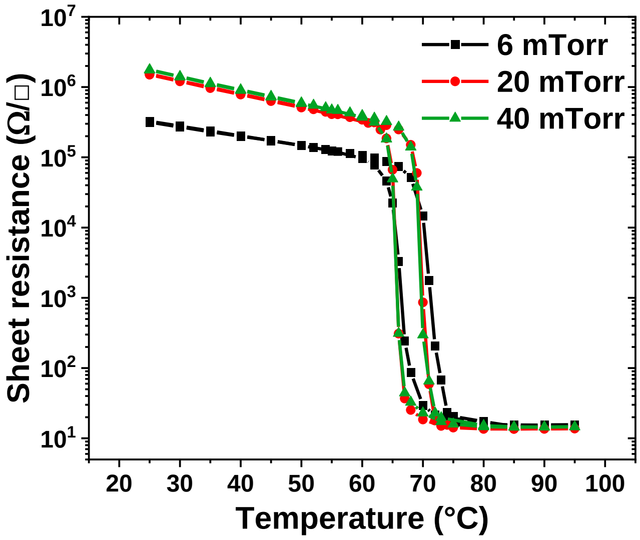

Figure 51. Temperature-dependent sheet resistance evolution for films annealed at 6, 20 and 40 mTorr O_2 atmosphere.

Annealing pressure	**T_{MIT} (°C)**	**ΔH (°C)**	**ΔT (°C)**	**$R_{S\,M1}/R_{S\,R}$ ratio**
6 mTorr	68.7 ± 0.1	4.9 ± 0.2	7.0 ± 0.2	2×10^4
20 mTorr	67.7 ± 0.1	4.2 ± 0.2	5.3 ± 0.2	1.1×10^5
40 mTorr	67.6 ± 0.1	4 ± 0.2	5.3 ± 0.2	1.2×10^5

Table 9. Hysteresis parameters of samples annealed at different O_2 pressures. Highlighted in blue is the film with standard deposition and standard annealing conditions.

The θ-2θ scans of the films, presented inFigure 52, show that, for the 20 and 40 mTorr annealing O_2 pressure, the VO_2 020 peaks are located at the same position, while for the one annealed under 6 mTorr O_2 the peak is more shifted towards higher angles. In terms of strain this corresponds to an e_{zz} of -0.18%, -0.11% and -0.10% when increasing the annealing pressure from 6 to 40 mTorr (Table 10), this strain most likely originating from a change in the O stoichiometry. From the XRD measurements it can be concluded that the annealing pressures indeed influences the structure of the films and the strain, especially at lower pressures.

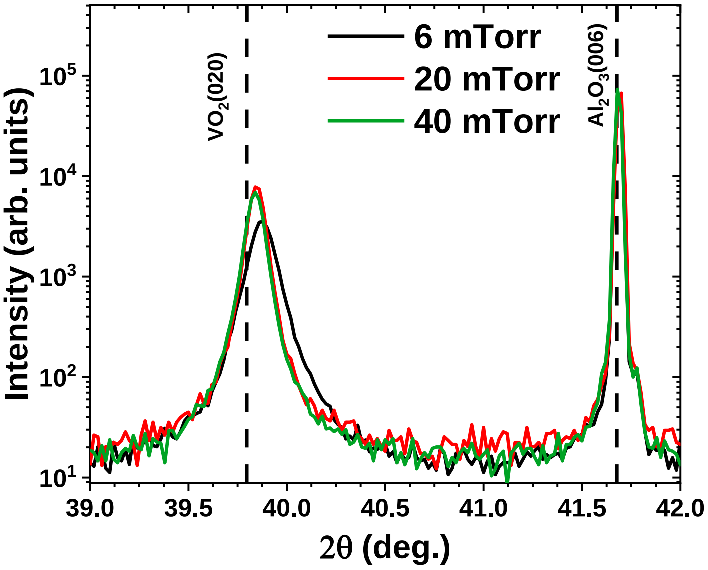

Figure 52. XRD θ-2θ scans measurements of films annealed at different O_2 pressures.

AFM analyses of the film annealed at 6 mTorr reveal a surface with very small grains and with an AGL of ~100 nm, which is almost half the AGL value for the films annealed at 20 mTorr (207 nm) (Figure 54 and Table 10). The values of the strain and AGL extracted from the films are presented in Table 10.

The differences between the hysteresis and transition widths of the two samples (Table 9) are however surprisingly small when considering the fact that the grain sizes of the 6 mTorr annealed sample are almost half of the ones annealed at 20 mTorr. This would indicate that while grain size is important, their effects are overshadowed by other parameters such as oxygen stoichiometry and strain, especially for epitaxially-grown thin films.

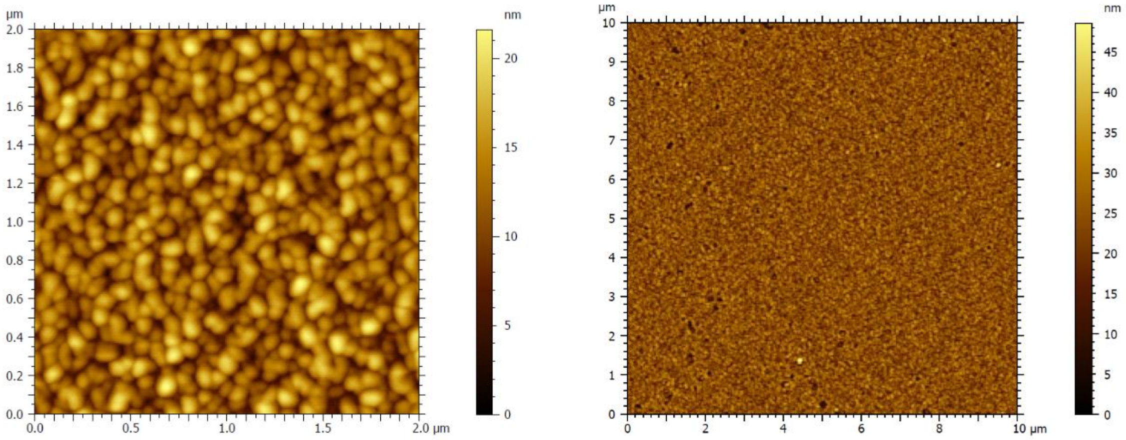

Figure 53. AFM scans on the films annealed in 6 mTorr O_2 atmosphere.

Annealing pressure (mTorr)	***Out-of-plane* strain (%)**	**Average grain length @ 2x2 μm^2 (nm)**
6	-0.18	98 ± 23
20	-0.11	207 ± 76
40	-0.10	-

Table 10. Out-of-plane strain and AGL of films annealed at different O_2 pressures.

The Raman spectral measurements of the same samples which are presented in Figure 54 reveal the same features on all the films regardless of pressure, the only difference being in the relative intensity of the peaks, possibly coming from the slight changes from the VO_2 stoichiometry from the different annealing chamber pressures.

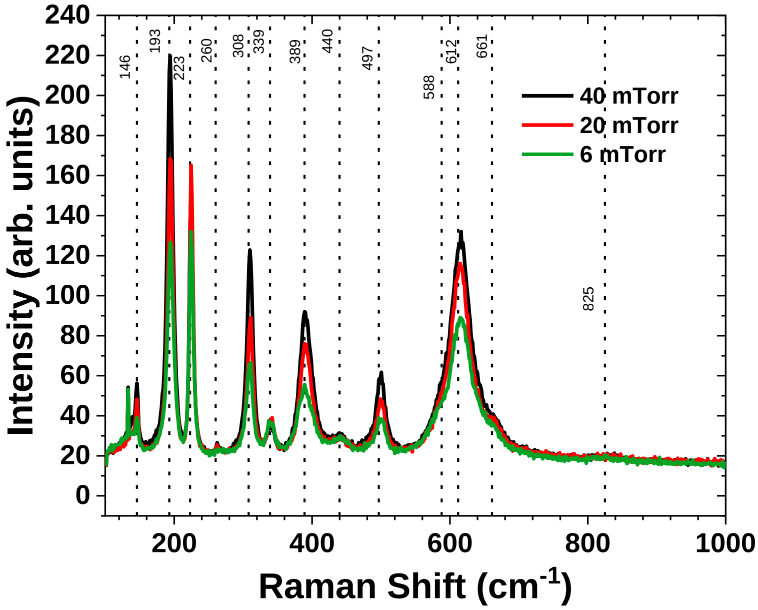

Figure 54. Raman spectra of films annealed at different chamber pressures.

III.3.2.1. Annealing time influence

The last annealing parameter whose influence was assessed was the annealing time in oxygen atmosphere. Comparisons were drawn between 30 and 90 minutes of O_2 annealing for samples deposited in different conditions. Table 11 represents the difference between the MIT parameters of the 90- and 30- minutes annealing of the films. The hysteresis curves are not shown simply because they look very similar to the ones annealed at 30 minutes, which have been already presented. The T_{MIT}, ΔH and ΔT generally increase with the annealing time, however, as the differences are mainly under the error, it can be assumed that increasing the annealing time does not lead to any modification of the electrical parameters. The metal-insulator resistivity ratios also slightly increase, which is due to an increase in the resistivity in the insulating phase.

Deposition conditions	**T_{MIT} difference(°C)**	**ΔH difference (°C)**	**ΔT difference (°C)**	**$R_{S\ M1}/R_{S\ R}$ ratio**
400°C, 2.5 sccm O_2	-0.1 ± 0.2	0.3 ± 0.3	0.3 ± 0.3	1.5×10^5
500°C, 2.2 sccm O2	0.5 ± 0.2	-0.1 ± 0.3	0.1 ± 0.3	1.3×10^5
500°C, 2.7 sccm O2	0.1 ± 0.1	0.1 ± 0.1	0.1 ± 0.1	1.1×10^5
600°C, 2.5 sccm O2	0.1 ± 0.2	0.1 ± 0.3	0.1 ± 0.3	1.3×10^5

Table 11. Difference between the 90- and 30- minutes electrical hysteresis parameters for samples obtained in different conditions.

XRD θ-2θ scans and ω-scans (not shown for similar reasons for the electrical hysteresis figures) of 30- and 90-minutes annealing superimpose neatly and show very similar peak intensities and positions. AFM scans on the sample deposited at 500°C under 2.7 sccm O_2 and annealed at 500°C for 90 min show that its AGLs are of 169 ± 58 nm, while for the same deposition but for an annealing at 750°C for 30 minutes are 210 ± 82 nm. This would suggest that the impact of a longer annealing time on grain coalescence is less significant than the annealing temperature parameter.

III.4. Terahertz amplitude modulation properties of the VO_2 films

Following the deposition of a large number of samples using seemingly identical deposition parameters, it was found that the value of the thickness was inconsistent. This inconsistency was determined to be due to the operating point of oxygen flow for the target T1, being in the middle of the target's transition mode in the plasma voltage vs oxygen flow curve, which resulted in unstable plasma discharges. This issue, combined with the overall poisoning curve evolution in time due to the target surface's degradation from heavy usage, made target T2 a better candidate for subsequent depositions. As a large part of the next chapter is dedicated to the THz measurements on bare and doped VO_2 layers obtained by using the T2 target, most of the results presented in this section will be focused on samples obtained using this target.

As the THz transmission measurements are performed in time-domain, the data needs to be converted to frequency-domain in order to efficiently analyze the THz radiation's interaction with the samples. This was done by removing the signal coming from the Fabry-Perot effect originating from the thick substrate (the small peaks after the most intense ones in Figure 55 a)) and subsequently using a Fast-Fourier transform of the spectra (FFT). Afterwards, the influences of the sapphire substrate and of the ambient atmosphere were subtracted from the raw spectra in order to record only the influence of the VO_2 film on the THz transmission. For this purpose, a reference spectrum was recorded from the substrate without the VO_2 layer. A representation of the THz amplitude modulation spectrum before and after applying the FFT and the above-mentioned corrections is presented in Figure 55.

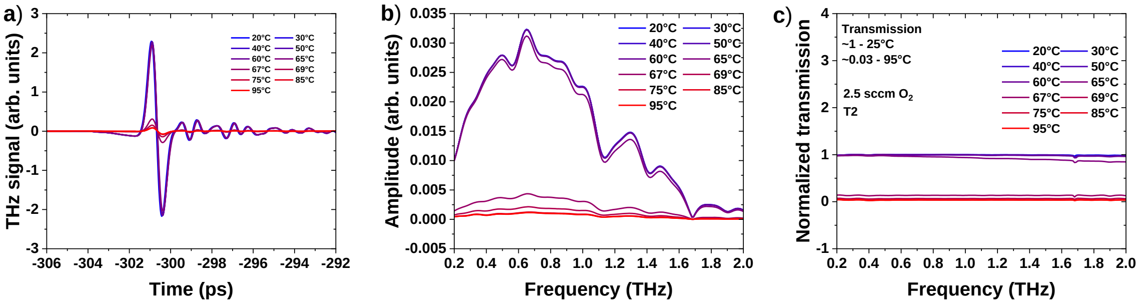

Figure 55. a) Time domain THz signal from a layer of VO_2 on a sapphire substrate at 20° and 95 °C, respectively b) As-obtained frequency domain THz amplitude modulation spectrum after FFT c) Normalized THz amplitude modulation spectrum of the VO_2 layer.

As the change in THz transmittance in VO_2 films is attributed to the variation in carrier density that stems from the phase transition, the modulation phenomenon is characterized by a broadband and nearly frequency-independent feature [75].

After the measurements, the values of THz transmissions in Figure 55 c) were averaged across the measured THz range (0.2 to 2 THz), and the results were plotted, finally giving a hysteresis curve resembling the electrical ones, as represented on Figure 56.

By using the same method of extracting the hysteresis parameters as in the case of the temperature-dependent resistivity measurements, we have extracted the amplitude modulation depth (MD), T_{MIT}, ΔT and ΔH characteristics for each sample (Table 12). The term MD is defined in Equation (12), where E_{max} and E_{min} are the maximum and minimum of the transmitted THz amplitude:

$$MD = \left[\frac{E_{max} - E_{min}}{E_{max}}\right] \tag{12}$$

The result of the analysis of the samples deposited at 1.5, 2 and 2.2 sccm O_2 flow from T2 and the standard deposition one from the target T1 (2.5 sccm O_2 flow) with standard annealing procedure for all the samples are presented (and indicated in the legend) on Figure 56. The sample obtained using the standard deposition and annealing condition from T1 was analyzed as well as it yielded the best results during the structural and electrical measurements. The analysis of the THz spectra during the thermally induced MIT in the samples show an abrupt transition in their normalized transmission with almost 100% transmission for the films in insulating state. VO_2 is known to have rather poor performances in the metallic state with the transmission usually being between 10 and 20% [171–173]. The results presented in Figure 56 show that, for specific samples, the normalized transmissions can be as low as 3% in the conductive state, at high temperatures, which confirm their high structural and electrical properties.

Various factors influence the MDs, and it is essential to consider the morphologies of the samples, their roughness, grain sizes, and films strain when discussing the MD. The *out-of-plane* e_{zz} strain of our samples is -0.54% for the one obtained at 2.2 sccm O_2, -0.03% for the one at 1.5 sccm O_2 and -0.08% for the 2 sccm O_2, and finally -0.11% for the 2.5 sccm O_2 film from T1. This strain evolution does not seem to be reflected in the MDs of the samples. Rather, according to Zhao *et al.* [174], the MD is strongly influenced by the resistance in the metallic phase which seems to be the case of our films as well, the MDs being lower for the films with the highest resistance in the rutile state.

A striking difference between the optical THz hysteresis and the temperature-dependent DC electrical hysteresis is the T_{MIT} of the samples, the THz T_{MIT} seemingly being lower. According to Pallares *et al.* [140] this difference between the electrical and optical measurements is likely induced by the lag between the nucleation of the R phase and its propagation to the grains interface. The grain boundaries interface change is directly affecting the local electrical carriers' transport, while the optical measurements are probing the overall change in materials properties of the global analyzed area, hence the variation between the optically and electrically recorded MIT properties. Another reason for the difference in T_{MIT} between the optical and electrical measurements is due to the need to form a conductive path between the electrical probes tips, which creates a delay in the measurements [13].

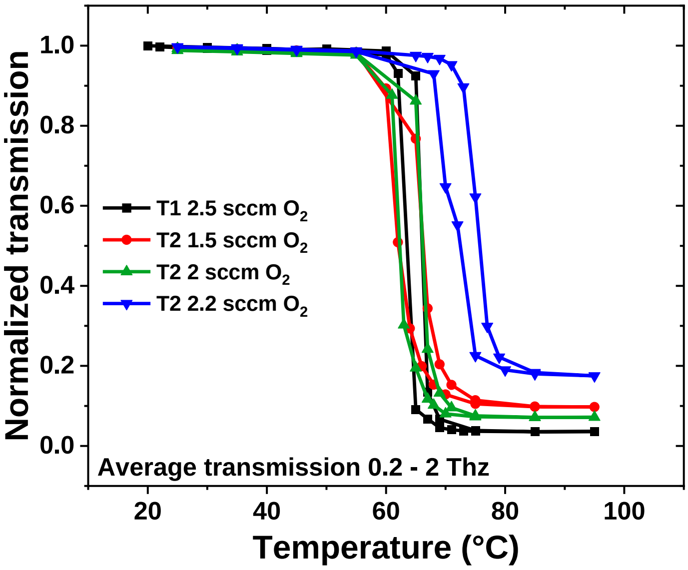

Figure 56. THz normalized transmission (0.2-2 THz) hysteresis curves of samples deposited at different oxygen flows and targets.

Sample	MD 0-2 THz (%)	T_{MIT} (°C)	ΔH (°C)	ΔT (°C)
1.5 sccm O_2 T2	90.2%	64.0 ± 0.3	4.1 ± 0.6	6.7 ± 0.6
2 sccm O_2 T2	92.7%	64.2 ± 0.2	3.8 ± 0.4	5.3 ± 0.4
2.2 sccm O_2 T2	82.4%	73.2 ± 0.6	4.0 ± 1.1	7.3 ± 1.1
2.5 sccm O_2 T1	96.4%	64.8 ± 0.1	2.6 ± 0.2	3.8 ± 0.2

Table 12. Hysteresis parameters of temperature-dependent normalized THz transmission (0.2-2 THz) of samples obtained at different oxygen flows and from different targets. Highlighted in blue is the sample with the highest MD.

Table 13 is comparing the performances of the obtained VO_2 films with similar layers and devices listed in literature. It can be seen that our bare VO_2 films perform much better, even compared to metasurfaces designed to improve the modulation depths. These properties are important for further incorporation of the fabricated VO_2 layers in THz modulators or meta-devices with state-of-the-art performances.

Design	Triggering method	Modulation depth	Frequency (THz)	Ref
Metasurface	Electrical	>60%	0.3-1	[175]
Bowtie antenna metasurface	Electrical	<90%	0.3-2.5	[176]
Hybrid metasurface	Electrical	68%	0.1-0.8	[72]
Bare VO_2	Thermal	85%	0.1-2	[177]
Bare VO_2	Thermal	69%	4.8-5.4	[140]
Bare VO_2	Thermal	74%	0.1-1.5	[172]
This work	Thermal	96%	0.2-2	-

Table 13. THz amplitude modulation performances of VO2 layers and devices reported in the literature compared to the highest attained MD in this work (highlighted in blue).

III.4.1. Conclusion

In this chapter the fabrication and characterization of VO_2 samples deposited and annealed in different conditions has been explored. Samples have been fabricated by means of reactive magnetron sputtering using two different targets, T1, which was older and with 99.5% V purity, and T2, newer, with 99.9% V purity. A defining feature of reactive magnetron sputtering is the existence of an oxygen poisoning curve i.e. a non-linear evolution of plasma voltage with increasing oxygen flow. This poisoning curve creates three distinct zones, a metallic zone, a transition zone (very reduced for the T2 target) where V_2O_3 films were obtained, and a poisoned zone, where low quality VO_2, V_2O_5 and a VO_2-V_2O_5 phase mixtures were obtained. We have employed an annealing step in order to increase the oxygen content in the films and reach the VO_2 phase. This step has proven very successful leading to the fabrication of high-quality films, with five orders of magnitude change in resistance between the insulating and metallic phases. For T1, three deposition oxygen flows were chosen, which were situated around the transition zone of the poisoning curve. Even though it was found later that this zone has unstable plasma characteristics that make repeatability an issue, especially regarding the thickness of the films, it was established that at a 2.5 sccm O_2 flow the films have the best structural and electrical characteristics. For the T2 target, the oxygen flows were chosen from the metallic and poisoned regions of the poisoning curve (0, 1.5, 2, 2.2, 2.5 sccm O_2). It was found that right where the poisoned region begins, the films integrate already a VO_2 phase, albeit of low quality. The annealing step was increased this film's resistance ratio between the low and high temperature phases and its structural quality, however a T_{MIT} of 76°C was obtained which was linked to a high *out-of-plane* strain. At slightly higher O_2 flow, a VO_2+V_2O_5 phase mixture was obtained, with annealing not having a huge impact on the film. The films deposited in the metallic region had more or less identical features to the ones as-deposited from T1, although the resistance ratios were smaller after annealing. The most surprising was that from this series the film deposited at 0 sccm O_2 (metallic V) had the best resistance ratio, although the film had high microstructural defects making its scale up to larger substrate areas doubtful. Scaling-up is easily done in reactive DC magnetron sputtering, as we have also deposited films on 3” wafers and substrates as large as 50×50 mm.

As the films obtained from T1 were better in terms of resistivity ratios, this target was used to explore the influence of the deposition and annealing parameters. Thus, films deposited at room temperature, 150, 400, 500 and 600°C were analyzed. It was found that the electrical performances, structural quality and phase purity of the films deposited at RT and 150°C were lower than the ones at higher temperature. After 400°C, the characteristics of the films didn’t change much upon increasing the temperature. The next deposition parameter that was varied was the thickness, where it was established that higher thicknesses (169 nm in our case) led to better structural and electrical qualities.

Next, we proceeded to investigate various annealing parameters and their effects. The initial focus was on exploring different temperatures, namely 450, 550, 650, and 750°C. It was found that 450°C is not sufficient to fully convert the V_2O_3 to VO_2, at least not for our annealing time of 30 minutes, the films existing in a V_2O_3+VO_2 phase mixture with a suppressed MIT. Increasing the annealing temperature to 550°C and 650°C revealed high quality VO_2 films with relatively similar structural and electrical characteristics. Further increasing the temperature to 750°C however led to “milky”, powdery-like looking films but with the highest resistance ratios between the insulating and metallic states. XRD ω-scans combined with φ-scans revealed also periodic misfit dislocations inside the films.

The influence of the chamber pressure (6, 20 and 40 mTorr) on the film’s electrical and structural properties was also explored. It was found that between 20 and 40 mTorr the results were very similar, while the films obtained at 6 mTorr showed lower resistance ratio, much lower grain sizes and higher in-plane strain.

The last type of analysis done in this chapter was related to THz transmission measurements. A film from the T2 target deposited at 500°C and annealed at 550°C was compared with samples deposited from T2 but realized under different experimental conditions. T2 was chosen because the samples from T1 presented inconsistent thicknesses due to sputtering plasma instability related issues. It was found that the films have high THz amplitude modulation depths over a range between 0.2 and 2 THz, at 96% for the films obtained from T1 in standard conditions, which is among the highest value reported in literature for VO_2 films.

Chapter IV. Fabrication of W:VO_2 thin films and thermal activation of their MIT

IV.1. Film fabrication

In order to fabricate tungsten doped VO_2 films, we used a simple yet effective method. A tungsten chip was placed on the metallic V target in order to integrate a fraction of tungsten atoms in the sputtering plasma during the deposition process. By selecting chips of various sizes, different W atomic percentages could be incorporated into the VO_2 thin films. For this purpose, three chip sizes have been selected, all with areas lower than 1 mm^2, and placed over the target. The W-doped VO_2 films were deposited from target 2 (T2). During all experiments, an oxygen flow of 2 sccm O_2 was used, with a deposition temperature of 500°C, for a total time of 30 minutes. The annealing step was employed on all samples in standard conditions (20 mTorr O_2 total pressure, 550°C annealing temperature, 30 minutes, 20 sccm O_2 flow).

To simplify the discussion in this chapter, the samples will be named as follows: D0, for the undoped VO_2 sample and D1, D2, and D3 for W:VO_2 samples with increasing amounts of tungsten. The undoped D0 was in fact based on two different samples: the first one corresponds to the sample grown from T1 deposited at 2.5 sccm O_2 as it had overall the best qualities (see Chapter 3); the second one, used for the electrical activation experiments, originates from a new VO_2 sample that was fabricated in order to deposit Au electrodes on them and test their activation behavior.

Albeit simple, the method used for doping does not allow direct control of the amount of W introduced in the films during growth as the chip sizes are arbitrarily chosen. Hence, the first step is to determine the atomic fraction of W in the film. For this purpose, Rutherford backscattering spectrometry (RBS) was used. These measurements were performed and the results analyzed at University of Paris-Saclay (IJCLab) by Aurelien Debelle and Lionel Thome. Figure 57 represents the experimental RBS spectra recorded on the undoped film and the films doped by the tungsten chips of different sizes. An RBS spectrum plots the number of backscattered ions vs. their energy, the latter being related to the depth at which the backscattering process took place and the nature of the atom of the target. The spectra display two main features: the signal at energies lower than 250 KeV, originating from the sapphire substrate and the ones after 250 KeV from the VO_2/ W:VO_2 layers. The solid lines present in Figure 57 correspond to the simulations done with the SIMNRA program [178], which allow to determine the overall composition of the films.

Sample D0 was deposited without any tungsten doping and could be fitted with a curve corresponding to a film with composition $VO_{1.9}$ which implies a lack of oxygen. For the samples D1-D3 the simulated curves were constructed by the addition of W within the $VO_{1.9}$ layer. The atomic fraction of W with respect to V was found to be 0.41%, 1.16%, and 1.86%, respectively.

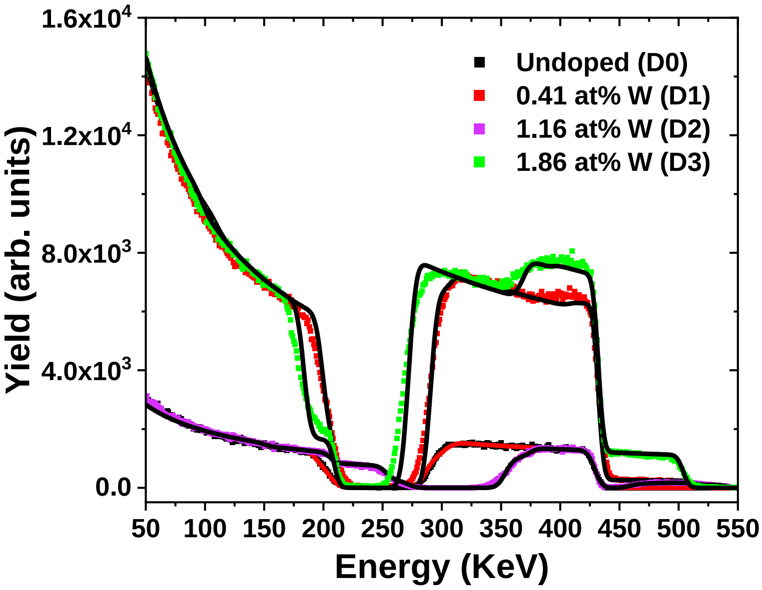

Figure 57. RBS spectra recorded on the W:VO_2 films with different amounts of doping.

IV.2. Structural and electrical properties of the W-doped films

The temperature-dependent resistance evolution was measured for each of the fabricated films. The results are plotted in Figure 58, and the extracted parameters are presented in Table 14. It can be seen that the T_{MIT} decreases for every increasing level of tungsten doping, from 67.7°C for D0 to 34.7°C for D3. By fitting the T_{MIT} for different doping levels with a straight line, a slope of 18.9°C ± 2.9/ at% W was extracted. This represents by how much every 1 at% of W reduces the T_{MIT}. Our results are similar to data reported in literature [124,179]. The ρ_{M1}/ρ_R ratio of the MIT transition also follows a monotonic decrease for every increasing doping level, dropping from a high five orders of magnitude to only one order of magnitude for the highest amount of W doping. This decrease is mainly due to the films becoming less insulating in the M_1 phase, which could be due to the structure's distortion towards a more rutile (conductive) phase [179,180], which will be further confirmed by the XRD and Raman measurements. While the hysteresis widths (ΔH) remain more or less the same after the initial doping threshold of 0.41%, the transition widths (ΔT) continuously increase for every doping level, up to 15°C for D3. Part of these effects can be explained through the analysis of the AFM scans which are shown in Figure 59 and will be shortly discussed hereafter.

It can also be seen from the hysteresis curves that D2 (green curve) has a higher conductivity in the metallic R phase than D3 (blue curve) and is comparable in resistivity to D3 in the M_1 phase. This effect is due to the lower thickness of sample D2 when compared to the other ones. Indeed, while most of the deposition speeds for the tungsten doping experiments were around 10-11 nm/ min, for total thicknesses of 300-350 nm, sample D2 had a deposition rate of 4.5 nm/ min, with a thickness of 134 nm. This can be attributed to fluctuations in the sputtering plasma, nonetheless, this thickness is large enough to consider that the thickness-related strain for all the films has little or no influence on their hysteresis parameters [163].

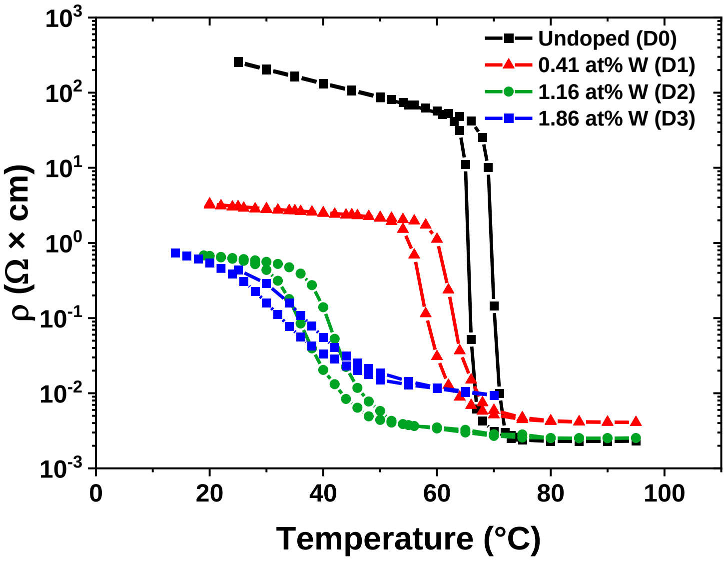

Figure 58. Temperature-dependent resistivity evolution for the undoped and W doped VO_2 films.

Doping level (at% W)	T_{MIT} (°C)	ΔH (°C)	ΔT (°C)	ρ_{M1}/ρ_R ratio
0	67.7 ± 0.1	4.2 ± 0.2	5.3 ± 0.2	1.1×10^5
0.41	60.6 ± 0.2	4.7 ± 0.4	8.9 ± 0.4	7.8×10^2
1.16	40.1 ± 0.3	4.9 ± 0.5	12.3 ± 0.5	2.7×10^2
1.86	34.7 ± 0.3	4.6 ± 0.6	16.2 ± 0.6	4.6×10

Table 14. Temperature-dependent resistivity evolution parameters for different doping levels.

The roughness and the grain sizes of the films have been extracted from the AFM scans. It can be seen that for increasing W content the grain sizes decrease from 207 nm for the undoped sample, to 120 nm for the sample with 0.41% W, and to 99 nm for the sample with 1.16 at% W level. The grains for the films with 1.86% W cannot clearly be identified due to their small size. D3 has also a very low surface roughness with a root mean square height (Sq) of 0.382 nm, similar to an as-deposited VO_2 layer. The decrease of grain sizes arising from metal-doping has been reported in literature and ascribed to the increase in density of nucleation sites [140]. As discussed in earlier chapters, it's important to note that grain size has an impact on both ΔT and ΔH. This influence is primarily due to the increased distribution of individual nanoscale grains' T_{MIT} in the films, which is a result of the higher defect density arising from the presence of grain boundaries. Furthermore, it was observed in reports that in metallic materials (Cu, Ni), a lower grain size increases the resistivity of the films [181,182], possibly seen here in the increase of the resistivity in the metallic rutile phase.

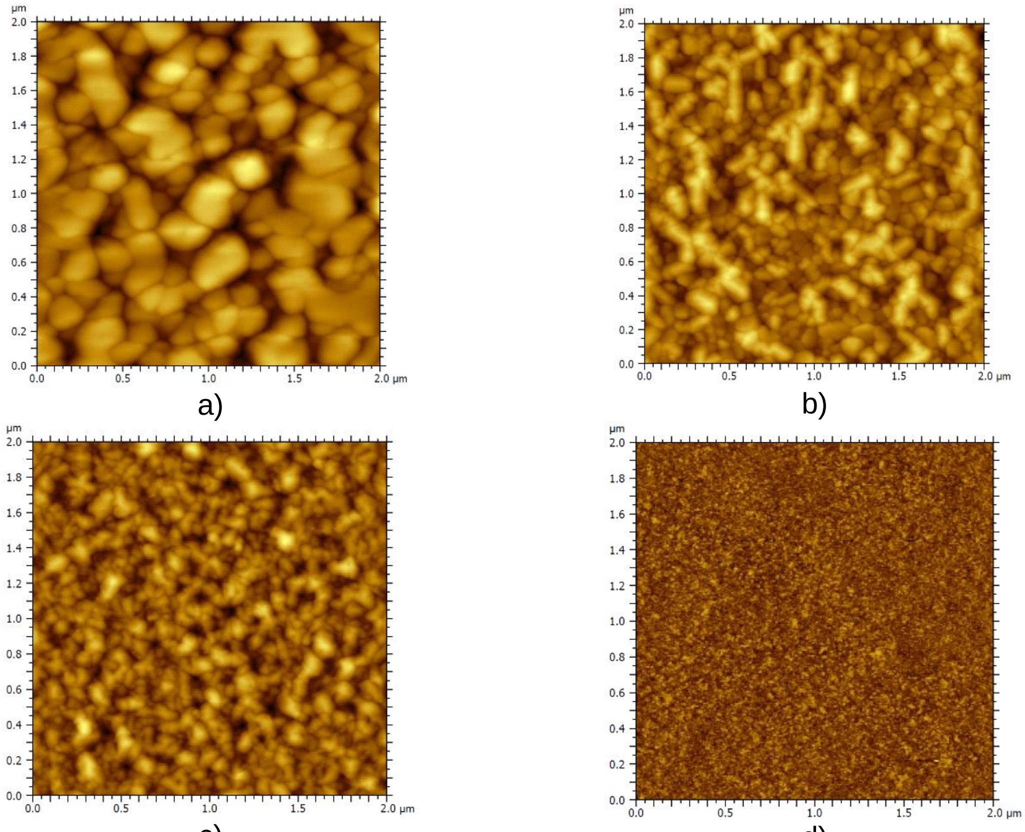

a) b)

c) d)

Figure 59. AFM scans of a) undoped film b) 0.41 at% W c) 1.16 at% W d) 1.86 at% W.

The θ-2θ XRD measurements of the films, illustrated in Figure 60 a), reveal the mono-oriented crystalline nature of the VO_2 films which persists even as the doping concentration attains its maximum level of 1.86 at% tungsten. One difference between the films stems from the emergence of a new peak at 27.7° for the sample at 1.86% W, which has been assigned to the (011) plane of VO_2. This disoriented phase likely appearing from the increased lattice distortions at high percentages of W doping. Furthermore, the *out-of-plane* strain e_{zz} of the doped samples, relative to the undoped samples (inset in Figure 60 b)), reveals an increase of the lattice parameter proportional to the doping amount, which demonstrates that W atoms are indeed incorporated in the VO_2 lattice. This increase alone should, however, not be taken as the only explanation for T_{MIT}'s decrease, as dopants with bigger atomic radii, such as Nb, are not as efficient as W in decreasing the T_{MIT}. Indeed, tungsten also acts as an electron dopant, with two added electrons per dopant ion. This effect is important in the VO_2 system as it decreases the energy required to dimerize the V-V atoms [183] which, according to Goodenough's model, are the first steps in the MIT. Table 15 summarizes the strain and grain sizes of the films.

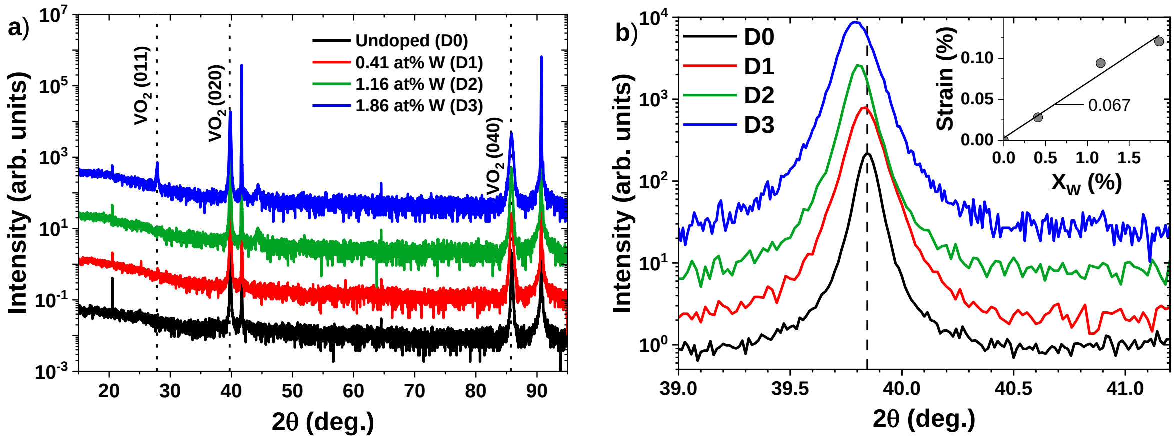

Figure 60. a) θ-2θ scan of W:VO_2 doped films between 15 and 95° and b) zoom on the VO_2 peaks compared with the undoped sample. Inset is the strain as a function of W doping with respect to the undoped sample.

Doping level (at% W)	**Average grain length (nm)**	***Out-of-plane* strain (%)**
0	207 ± 76	-
0.41	120 ± 41	0.03 ± 0.33
1.16	99 ± 29	0.09 ± 0.29
1.86	-	0.12 ± 0.06

Table 15. Average grain lengths and out-of-plane strain for films with different doping amounts with respect to the undoped film.

IV.3. Characterization of the structural phase transition

Temperature-dependent XRD measurements were also performed in order to evaluate the evolution of the structural phase transition with increasing W doping. The results are presented in Figure 61. As the W content increases in the films, the angular separation between the monoclinic and rutile phases of the films becomes less and less pronounced. Quantitatively, the relative difference in lattice spacing between the two phases decreases from 0.31% for the undoped film, down to 0.07% for the most doped film. This phenomenon indicates that, upon W doping, both phases (M1 and R) are structurally distorted and are getting more similar. A similar phenomenon has been reported in other works [180,184,185], where it was argued that upon W-doping, the local M_1 structure is distorted by the W substitution. This structural similarity allows to explain the reduced resistivity ratio. Moreover, since less energy is needed for the M1-R transition to take place this also explains the shift of the MIT.

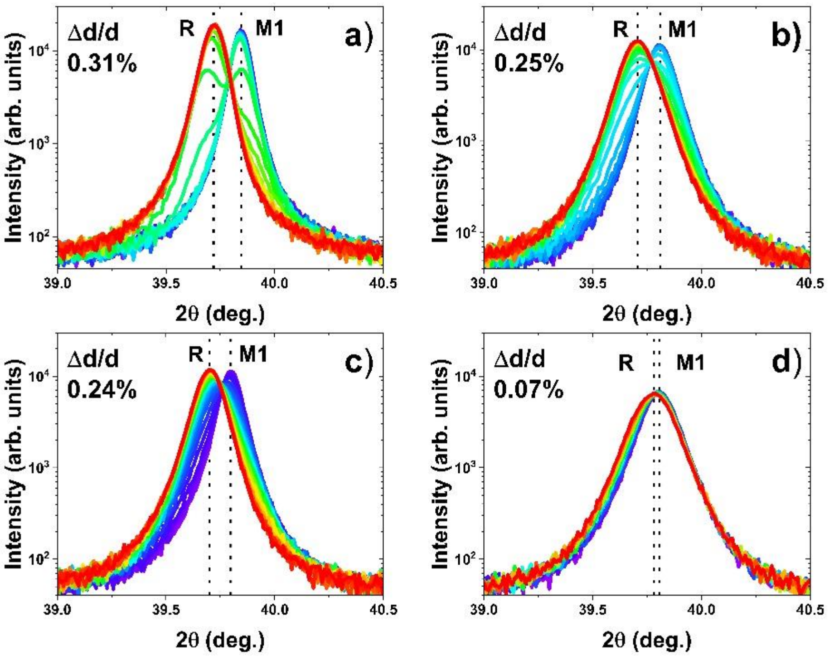

Figure 61. Temperature-dependent structural phase transitions of a) undoped (D0) b) 0.41 at% W (D1), c) 1.16 at% W (D2) and d) 1.86 at% W (D3) samples with indications of the Δd/d ratio between the M_1 and R phases.

Furthermore, the volume fraction of the M_1 phase with increasing temperature (Figure 62) can be extracted from the XRD scans in Figure 61. The transition temperatures of the samples and their evolution are similar to the ones extracted from the temperature-dependent resistivity scans, although absolute values may slightly differ because two different heating systems were used in the electrical and XRD experiments. It can also be noted that in the case of D3, the film starts at a value lower than 1, implying that the rutile phase is already present at room temperature.

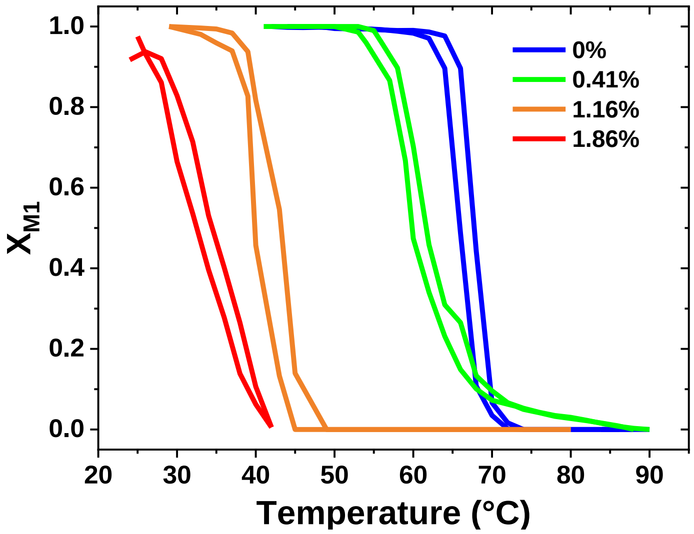

Figure 62. Temperature-dependent M_1 phase volume fraction evolution for W:VO_2 films of different W doping amounts.

Room temperature Raman measurements, illustrated in Figure 63, were performed on the undoped and doped films, and show that all scans present similar features, with typical M1 VO_2 peaks present at ~144, 193, 223, 259, 310, 339, 387, 442, 499, 613, 830 cm^{-1} [186]. The data has been normalized to the intensity of the ~613 cm^{-1} peak of each spectrum.

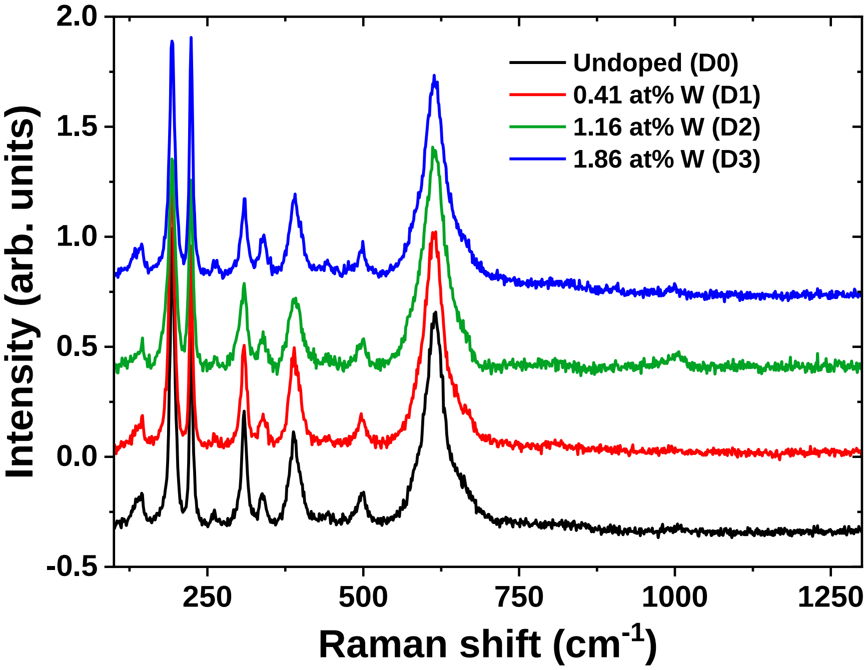

Figure 63. Raman spectra of films doped with different W amounts.

Raman scans of undoped films performed at room temperature have already been presented in Chapter 3, where all the peaks have been accounted for and discussed. Thus, it is interesting now to look at temperature-dependent Raman measurements performed on D0 and D3 samples in order to better understand the MIT mechanism of a typical VO_2 film when compared to a highly W-doped one. For the undoped D0 film, presented in Figure 64 a), the behavior is similar to other literature reports between the 60 and 75°C temperature range, with the Raman peaks dropping abruptly in intensity as they transition to the rutile phase with increasing temperature. Furthermore, it can be seen that the double peaks at 196 cm^{-1} and 224 cm^{-1} suffer very slight redshift while the peak around 620 cm^{-1} suffers a higher one of around 20 cm^{-1}, which is consistent with the emergence of the transitional M_2 phase [187]. In contrast, the D3 spectra remain unchanged from 16°C to 60°C (a temperature range including the MIT as observed from XRD and electrical measurements) and do not show any peak disappearance associated with the emergence of metallic VO_2. This is consistent with the structural similarity between the two phases observed by XRD. As the structural phase transition occurs between the disordered M_1 and R phases, the symmetry does not change significantly enough to be recorded by the Raman measurements. This effect has been reported before in [188]. However, a different behavior was more often described, where increasing the W-doping level leads to the decrease in intensity and broadening of the M_1 Raman peaks, due to the film's change in symmetry at RT [189,190].

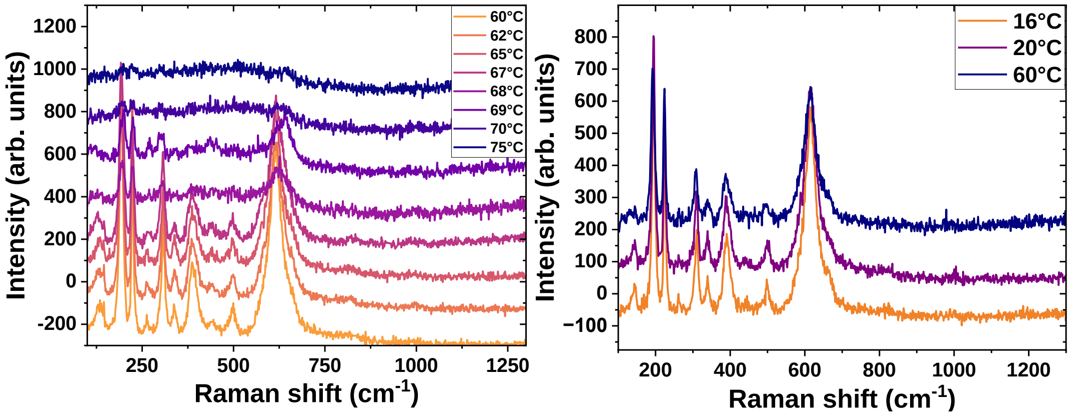

Figure 64. Raman spectra at different temperatures for the a) undoped film D0 and b) the most doped film, D3.

IV.4. Characterization of the THz amplitude modulation properties of the W:VO_2 samples

Temperature-depended THz optical measurements were performed in order to quantify the modulation depth of the samples with different W content. The method of data acquisition and analysis was described in Chapter 3, but to quickly recapitulate: the measurements are done initially in time-domain and transformed into frequency-domain with a Fast Fourier Transform, the data is then normalized to the spectrum of the bare substrate and ambient atmosphere. Figure 65 represents the normalized transmissions of the undoped and the highly doped film (1.86 at% W). To obtain hysteresis curves, the transmission values between 0.2 and 2 THz were averaged for each measured temperature. The steps mentioned here are better visualized in Figure 55.

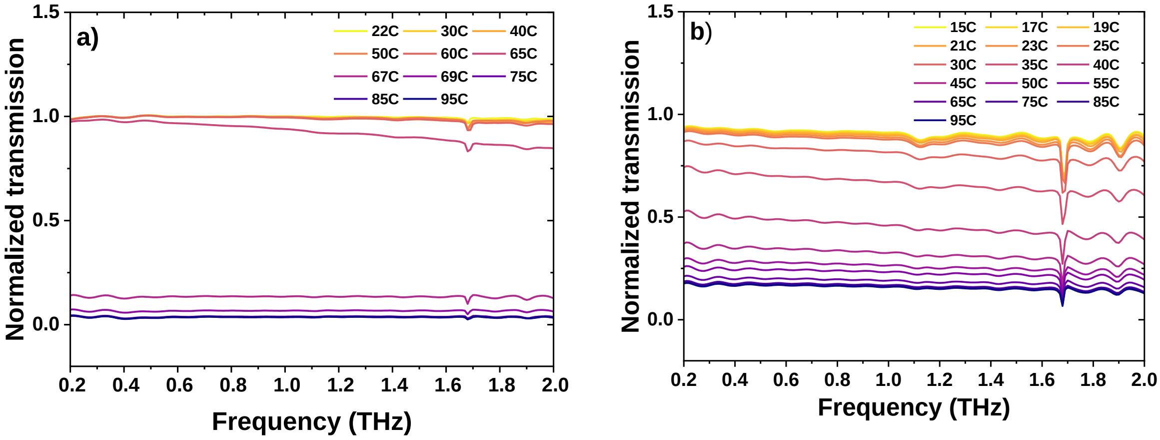

Figure 65. Temperature-dependent frequency domain spectra of a) D0, the undoped sample and b) D3, the highest W-doped sample (1.86 at% W).

The temperature-dependent normalized THz amplitudes and the associated parameters extracted from the hysteresis curves (Figure 66 and Table 16), show a decrease in the T_{MIT} for each subsequent level of doping, similar to the electrical measurements. It is however noteworthy the fact that at the higher W doping levels, D2 and D3, the T_{MIT} is slightly higher (<1°C) in the optical measurements than the electrical ones. The MIT in the films is expected to begin within the bulk of the material, resulting in a delay between the electrical measurements (which rely on the surface contact of the probes) and the optical measurements. This lag can seemingly make the optical T_{MIT} appear at a lower value compared to the electrical T_{MIT} which is the case for the films presented in the previous chapter and the D0 and D1 films here. The fact that for D2 and D3 electrical T_{MIT} is lower could be explained by the hole in the middle of the Peltier heating element designed to let the THz radiation through, which might introduce a slight temperature difference in the sample region above the hole, compared with the surrounding area.

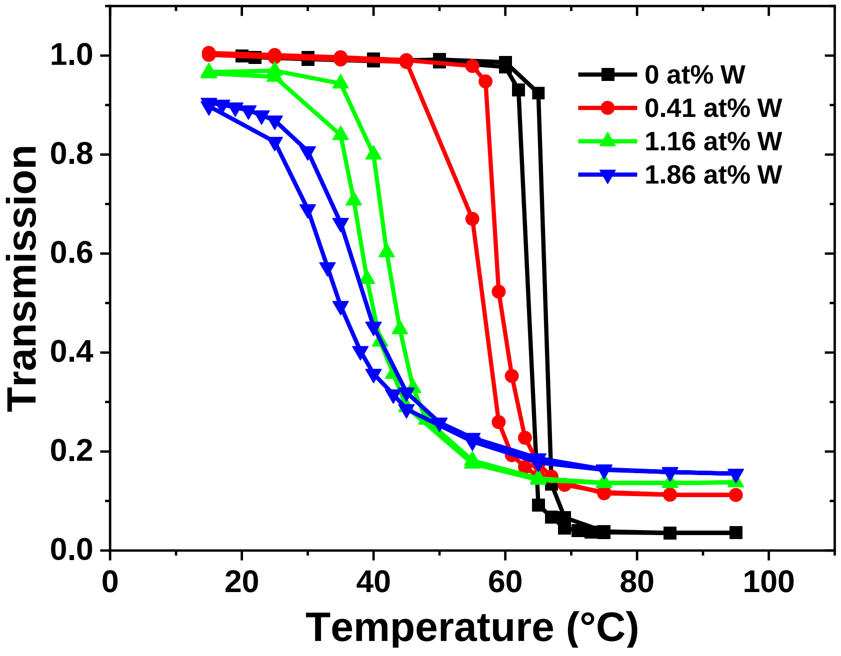

Figure 66. Temperature-dependent normalized THz amplitude transmission through the undoped and W-doped VO_2 samples.

W content (%)	MD (%)	T_{MIT} (°C)	ΔH (°C)	ΔT (°C)
0	96.3	64.8 ± 0.1	2.6 ± 0.2	3.8 ± 0.2
0.41	88.9	57.6 ± 0.4	3.2 ± 0.8	7.1 ± 0.8
1.16	85.7	40.8 ± 0.5	3.6 ± 0.9	9.6 ± 0.9
1.86	79.7	35.4 ± 0.6	4.3 ± 1.2	15.4 ± 1.2

Table 16. Hysteresis parameters of the THz amplitude transmission curves in Figure 66.

Interestingly, the magnitude of the transition is not as drastically changed in the THz transmission when compared to the change in resistivity presented in Figure 58. The modulation depth in the THz domain has been previously noted to be heavily influenced by the metallic phase and the free carrier density of the films [174]. Even though the resistivity is low in the insulating phase, the free electron density could still be not high enough to significantly affect the transmitted THz amplitude for the investigated frequency domain. However, this does not mean that the electron doping has no effect, as the transmission at room temperature is still reduced.

The differences between electrical and optical measurements are also affected by structural defects (like those at the film/substrate interface [163]) and grain boundaries, which in turn influence how the phase transition spreads through the material. Whereas structural defects and grain boundaries have a high impact on the electrical measurements by limiting carrier mobility or acting as charge carrier traps, these effects are negligible in the optical measurements [191].

IV.5. Large-area electrical activation of the MIT in the doped films

While temperature-dependent measurements are of interest to study the effect of doping on the films, the ability to control the MIT through electrical means is essential for the functionality of many devices.

In order to characterize the electrically- induced MIT on relatively large thin films areas, simple two-terminal devices were fabricated by photolithography, lift-off technique, and e-beam evaporation. Thus, Au electrodes were evaporated on the sides of the 10x10 mm^2 samples, each with a size of 3.1 × 10 mm^2, leaving a W:VO$_2$ strip measuring 3.8 × 10 mm^2 in the middle of the substrate (Figure 67). This distance can be considered as fairly large for electrical MIT activation, with reports in literature rarely going over lengths of 10 μm. As such, our films are one thousand times larger in width than typical electrically activated VO$_2$. These dimensions were nonetheless required both for XRD characterization (where the beam cross-section is 0.2 mm and more particularly for the THz characterization, as the THz spot of our system has a ~3 mm diameter.

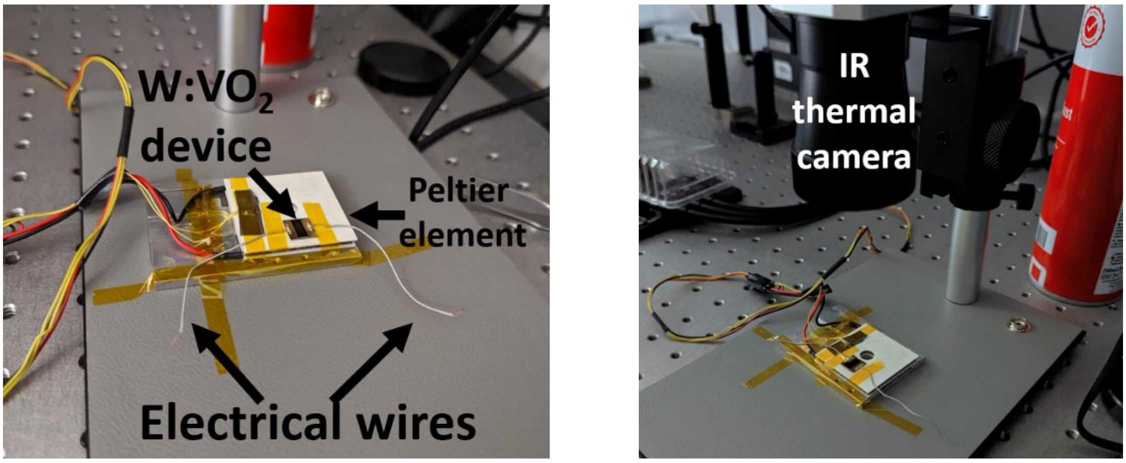

a) b)

Figure 67. a) Image of the realized devices mounted on the Peltier element and b) photo of the overall activation set-up including the IR thermal camera used for recording the specific phase change of the materials during IMT.

IV.5.1. Infrared thermal imaging of the transition under electrical activation

Figure 68 shows and explains some of the visible features of the thermal images, as well as the color scale for the undoped films, although it’s important to understand that the essential part of these images is not the temperature itself, but rather the color difference between the M$_1$ and R phase when the MIT is achieved. In the following section, the characterization and the onset of the metallic channel for various current and voltage values settings will be described.

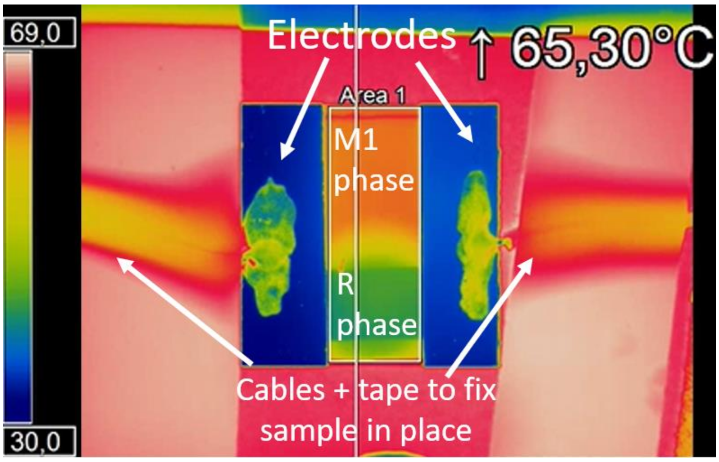

Figure 68. Typical IR thermal image of a VO_2-based device with annotations on the main features.

The current- voltage (I- V) curves of the two-terminal devices were first recorded in current mode (linearly sweep current and record voltage) in order to check the influence of the W-doping. Because of the large VO_2 areas, to reduce the necessary current/ voltage threshold for the MIT, we applied a thermal bias for the samples placed atop a Peltier heating element. Thus, the samples were maintained at 20°C for D3, 55°C for D1, and 64°C for D0. The current-controlled characteristic of the devices is presented in Figure 69, the inset image representing the current-time sweep characteristic.

In the first, low-current region of the curves, where the films are in the insulating phase, the voltage increases more or less linearly with increasing current until a certain threshold value of the voltage (V_{th}) where the MIT is triggered and the voltage drastically decreases. The V_{th} values are 142.58 V, 48.27 V, and 16.37 V for D0, D1, and D3 respectively (at the thermal bias temperatures of 64, 55, and 20°C). Although these switching voltages are much higher than the ones reported in the literature [192], it is important to remember that the films presented here have much larger distances between electrodes, almost 4 mm, when the ranges usually reported are in the µm-scale ranges.

At the threshold value, the films' voltage abruptly decreases with increasing current for the undoped films. This decrease in voltage is less abrupt as the doping levels increase, as it can be seen in Figure 69 for the red (sample D1) and black (sample D3) curves. The onset of this negative differential resistance (NDR) zone was already reported for nano- and micrometer-scales planar or out-of-plane VO_2-based devices [193,194] and was used to initiate free voltage oscillations in the devices, which are performing like relaxation oscillators. The performances of the oscillating behavior on our large-scale VO_2 devices (injected currents, frequency, amplitude) were not further tested due to time constraints.

After this sharp decrease in voltage, a second NDR zone can be seen, the change between the two zones, NDR1 and NDR2 (will be shortly explained, but the NDRs are highlighted in Figure 70), being much more evident on sample D1 (red curve in Figure 69). When the applied current is reduced to zero, the metallic phase is persisting i.e. there is no return to the insulating state (high voltage for a low applied current). Due to the additional thermal heating bias, the material state is “caught” in the lower-resistivity, metallic part of the cooling hysteresis curve (this will be further expanded on in the chapter on the optical activation of the doped films).

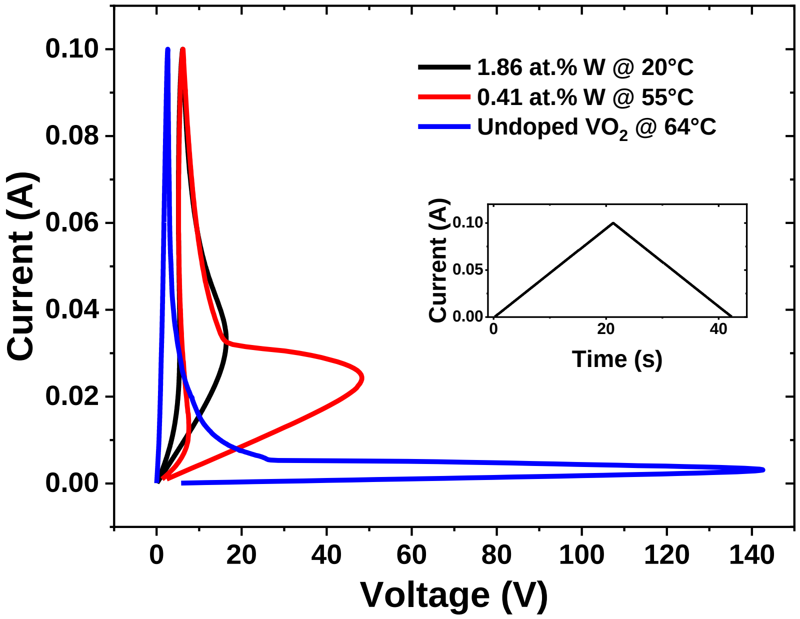

Figure 69. Current-voltage characteristics of current-controlled films D0, D1, and D3. The inset is representing the current sweeping function applied to the samples.

The IR thermal imagining can be combined with the I-V curve of the undoped film in order to have a better understanding of the mechanism of electrically triggered MIT. Since the IR and electrical measurements were not synchronized automatically, it is important to note that the explanations provided here offer only qualitative insights. Thus, Figure 70 is showing the combined IR thermal and electrical measurements of the undoped D0 film, which is initially heated at 64°C (below the MIT temperature). As the current increases from point 1 up until point 2, the IR thermal images show uniformly colored films, indicating that in this part, the film remains insulating. The region between points 2 and 3 is associated with the metallic channel formation between the two electrodes and onsets the 1st NDR. Rather interestingly, in points 2 and 3, it seems that the metallic channel initially forms in the middle of the film and then connects to the electrodes. Thus, it can be assumed that this NDR region could be successfully used for self-sustained oscillations, as the device itself could behave like a capacitor that charges and discharges periodically. When the 2nd NDR zone starts, between points 3 and 4, the channel expands until it fills the upper part of the film’s area with the metallic phase. This region is somewhat slower to form than the first NDR, but still faster than between points 4 and 5 which represents the channel trying to expand in the opposite direction of the initial metallic phase expansion and to fully cover the film. Finally, when the current is decreased back to 0 A (film state at point 6), the metallic channel is still present due to the persistence of the metallic state of the film due to the hysteresis loop.

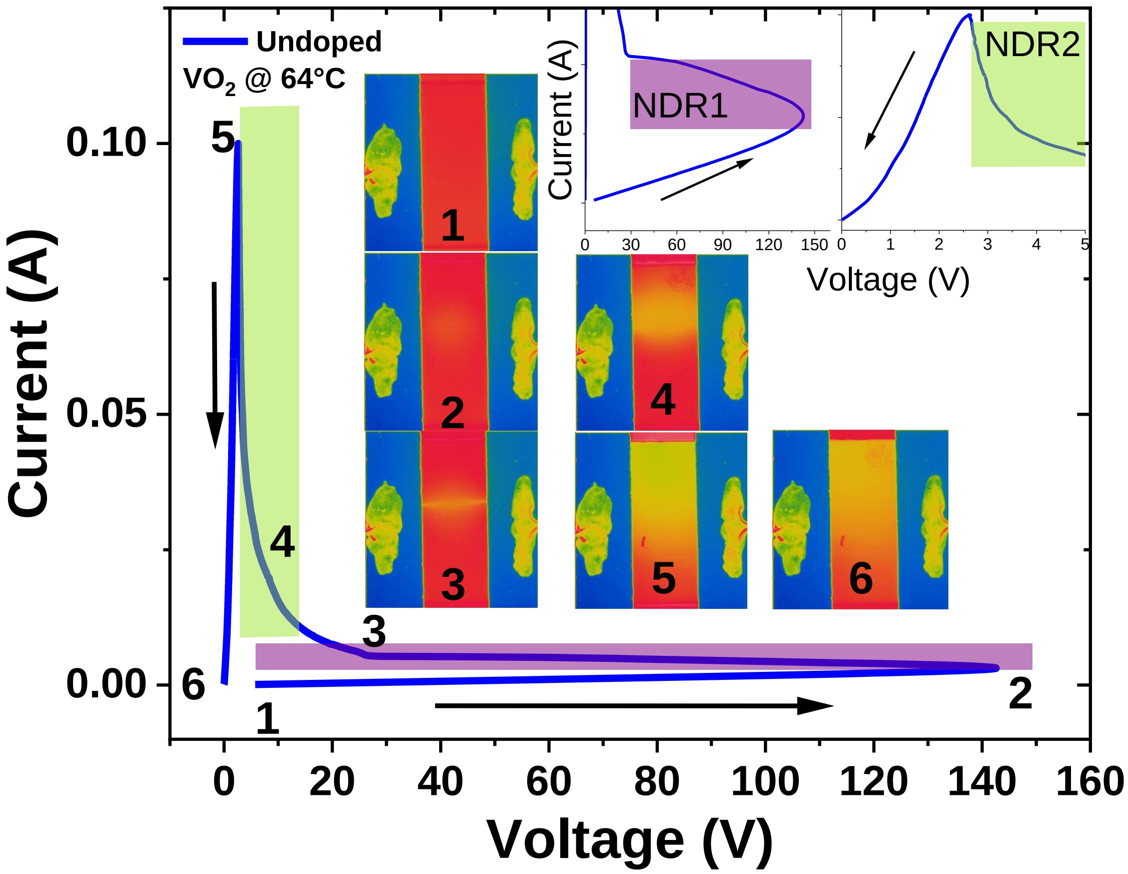

Figure 70. Combined IR thermal and I-V curve electrical measurements of the undoped D0 heated at 64°C highlighting the NDR zones and voltage thresholds and associated thermal images.

We now consider the case of the voltage-controlled electrical triggering of the MIT. The methodology consists in setting the current compliance (i.e. the maximum current value the source is able to reach for a range of voltage values) at a value larger than the supposed current threshold for the MIT. As the films are insulating, a small amount of current is flowing within the samples even for a relatively large voltage. The voltage of the source was gradually raised until it abruptly decreased, signifying the onset of the MIT. Afterwards, the current compliance was also gradually increased, to allow the further increase of the voltage values, at different increments, usually of 50 mA. At each current increment step, IR thermal imaging was used to visually assess the transition via the change in emissivity between the insulating and conductive phases.

Figure 71 and Figure 72 present the IR images for the undoped films before, during, and after the MIT. It can be seen in these figures that the transition is initiated when a conducting channel is formed between the electrodes, and reaches completion once the channel laterally grows to completely fill the gap between the electrodes. This behavior of filament formation and expansion with increasing current is similar to other reported studies such as [195,196].

In the case of the undoped film D0, similarly to the current-controlled transition, the sample had to be first heated to 64°C with the help of a Peltier heating element. In the first transition cycles the metallic channel appeared in different locations (Figure 71), but as the MIT was cycled through more times, the positions of the channel became more consistent, probably suggesting lasting changes in the film's structure. On average, it was found that MIT was triggered at around 75V and 9.5 mA.

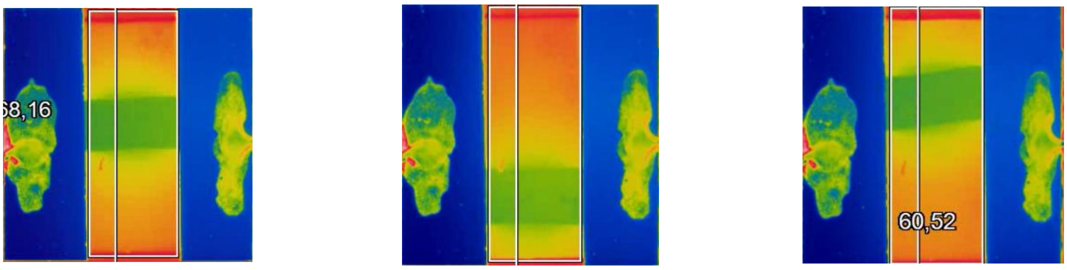

a) b) c)

Figure 71. IR images displaying the random position where the metallic channel initiates on the undoped VO_2 films (D0 sample, maintained at 64°C) at an average threshold voltage and current of 75 V and 9.5 mA.

Figure 72 shows the evolution of the D0 film with increasing current compliance. Once the channel had been triggered (Figure 72 b)) it was not unusual for the intensity of the color to slightly fade (Figure 72 c)) and then to re-appear as the current compliance increased, and finally to spread in a diffuse manner throughout the sample (Figure 72 d), e), f)). This fade in color intensity could be due to a redistribution of heat in the system, with the metallic phase spreading outside the initial strongly delimited path, or simply an artifact created by the IR camera detector’s delay in adjusting to the new channel’s color intensity. If the metallic channel appeared closer to an edge of the sample, as in Figure 71 b) and c), the smaller region to the film’s edge would be the first to transition to the metallic phase. To summarize, the main characteristics of the film during the transition is the formation of a clearly delimited channel at the onset of the transition followed by a diffuse spread of the metallic phase towards the edges.

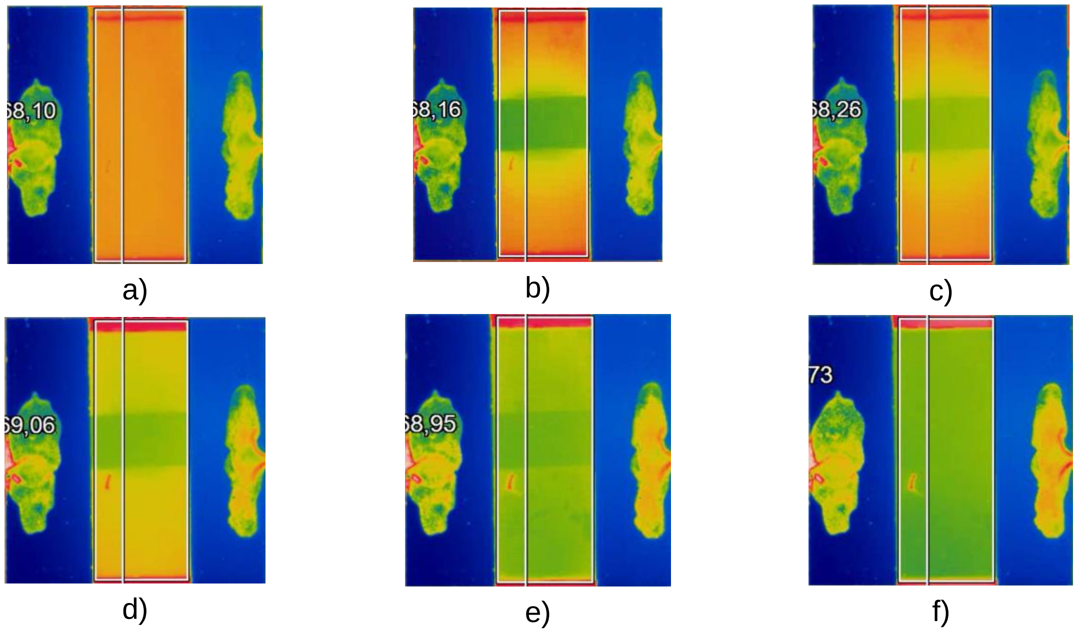
a) b) c)

d) e) f)

Figure 72. IR images of the undoped D0 film at a bias temperature of 64°C a) before MIT onset, b) initial channel creating. c), d), e), f) channel expansion with increasing current, until a maximum current of 305 mA.

The thermal activation images of D1 and D2 devices are not shown. For D1 the activation was explored at sample temperatures of 25, 50, and 55°C. It was observed that for 50 and 55°C the metallic channel had no abrupt onset, rather it started from the upper or lower edge of the device and expanded from there. At 25°C however, the onset of a small channel was observed. In the case of D2, two starting temperatures were explored, 25°C and 30°C, both temperatures giving similar results i.e. no clear channel onset was present, rather a diffuse metallic VO_2 phase beginning from the sample's edge and increasing with the current.

For the D3 sample, the Peltier heating element's temperature was set at 18°C, in order to be sure that the film is in the insulating state. The results of the activation, as recorded by the IR thermal imaging are similar to D2, in that there is no obvious channel formation but rather a gradient of temperature on the surface of the samples.

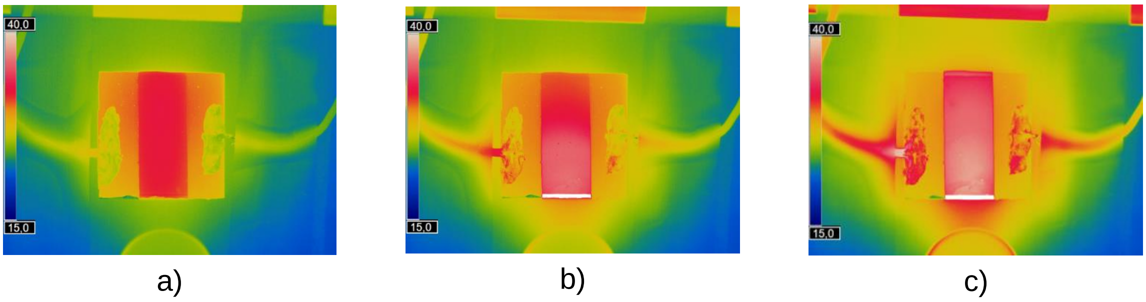

a) b) c)

Figure 73. IR thermal images of the D3 film (1.86 at% $W:VO_2$) held at a bias temperature of 18°C at a) 50 mA b) 100 mA and c) 200 mA current.

Summing up, in this chapter, current-controlled MIT exhibiting two NDR zones were presented. The first NDR zone corresponds to the initial onset of the MIT, while the second NDR zone is linked to the gradual expansion of the metallic channel. For the undoped VO_2 film, the MIT occurs rapidly, whereas for films with tungsten doping the transition becomes more gradual.

When performing the voltage control of the transition, a similar pattern is observed, but the films have now a much larger initial metallic channel, as attested by the IR thermal imaging. Not only this, but the channels are also more thoroughly metallic, as the contrast between the insulating and metallic phases is larger. As doping increases, this channel becomes more diffuse. At the highest doping level (1.86 at% W), only a temperature gradient is visible, suggesting that the emissivities are more similar in this case.

The initial current compliance as well as the W doping have an important effect on the size of the channel. For instance, IR thermal imaging measurements on samples D0 and D1 revealed that after the I-V threshold was passed, a metallic channel could be clearly distinguished, whereas for D2 and D3, the channel formation is much less obvious. Furthermore, the activation time of the highly doped sample (D3) under a current of 400 mA was measured by coupling an oscilloscope to the circuit. It was revealed that for this highly doped film, the activation time from the insulating to the metallic phase was 0.36 ms.

IV.5.2. Characterization of the structural phase transition

After a qualitative analysis of the phase transition through the utilization of the IR thermal camera, we may now consider the structural evolution of the films during the electrically activated transition. For this purpose, XRD measurements were performed along the W:VO_2 strips between the two electrodes of the devices. The following methodology was employed:

i. θ-2θ scans were performed on the films before and after the thermal MIT in order to extract the 020 M_1 and 200 R peak positions;

ii. the X-ray detector was fixed for the diffraction condition of the M_1 peak and measurements were performed while moving the x motor from one side to the other along the W:VO_2 strip (Figure 74);

iii. the measurement was repeated with the detector in the diffraction condition for the R phase;

iv. the measurement set was repeated for increasing current values injected in the device.

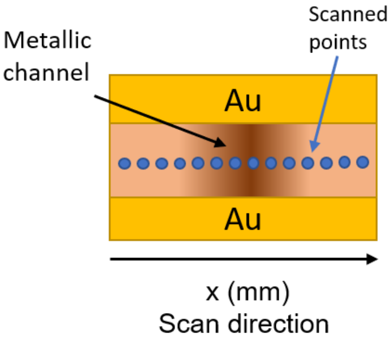

Figure 74. XRD measurement procedure for spatially evaluating the structural phase transition of the electrically activated W:VO_2 films. Every blue point represents a scan position.

The results of the scans for D0 and D1, the samples which presented clearly distinguishable metallic channels during the IR imaging, can be seen in Figure 75. Let us first discuss the case of the M_1 phase for sample D0 (Figure 75 a)). Without any current, the intensity of the M_1 peak is roughly constant along the direction parallel to the electrodes which is an expected behavior since the whole film is constituted of the M_1 phase, thus there should be no major variations in the diffracted intensity when sweeping the beam from one edge to the other. Some variation in intensity can occur, however, due to the change in the diffracting grains' strain or orientation. For the first current, a step is formed around 1 mm, indicating a decrease of the intensity of the XRD peak corresponding to the M1 phase, i.e. a decrease of the volume fraction of the M1 phase. For increasing currents, this step shifts towards lower x values pointing to an increase and eventual domination of the M_1-depleted region. The evolution of the R peak intensity has the exact complementary behavior. Without any current, the value from the R phase is very low and constant. Note that, strictly speaking, the intensity should be zero, but, because of the proximity of the peaks, especially at high doping levels, and the angular opening of the detector (0.01°), a non-zero value is obtained by integrating some photons diffracted from the M_1 phase. With increasing current, a step appears at the exact same location as for the M_1 peak, but with an increased intensity, pointing to an increased volume fraction of the R phase, i.e. the M_1 phase is transformed into the R phase at these particular positions on the film. This experiment allows to map the spatial distribution of the M_1 and R phases and, hence, to evidence that the conductive channel observed by IR imaging is unambiguously linked to the M_1/R transition.

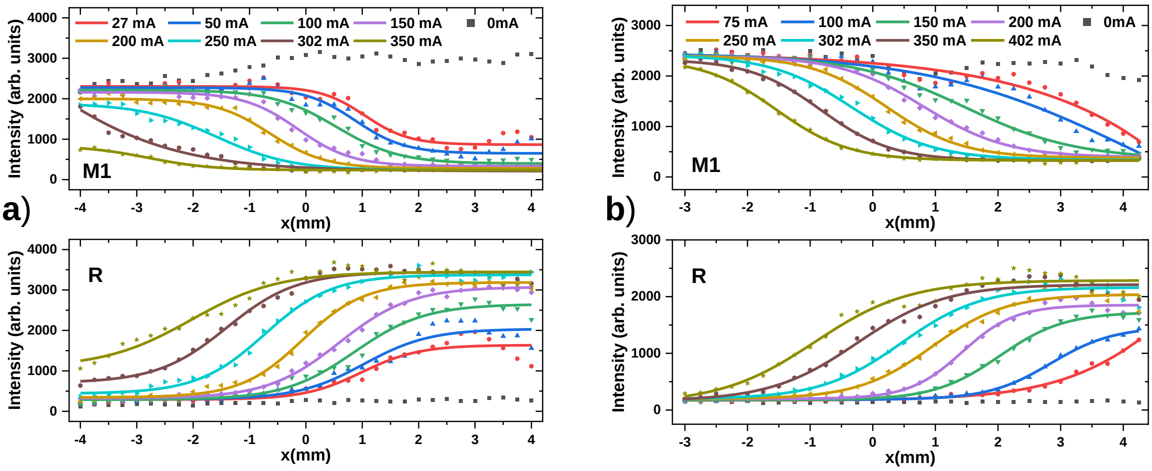

Figure 75. XRD scan along the VO_2 strip during the electrical activation of the MIT for different doping levels a) undoped D0 device at a temperature bias of 65°C and b) D1 device - 0.41 at% $W:VO_2$ at a temperature bias of 55°C.

A similar analysis is presented in Figure 76 for samples D2 and D3. From these analyses on the higher-doped samples it can be concluded that a similar behavior is observed for all doping levels, with two major evolutions:

i. the width of the spatial boundary between the M1 and R phase increases with increasing doping level (transition less abrupt from M1 to R). This is consistent with the IR imaging observation where a gradient-like distribution was observed for D2 and D3, instead of a marked step. In the case of sample D3, visual inspection, and even the XRD analysis, can barely detect the spatially step transition between the M1 and R phases.

ii. the intensity contrast across the step is progressively reduced. This is due to the fact that the M_1 and R peaks are getting closer to one another when increasing W content, hence reducing the ability to clearly separate both phases (as already explained above, Figure 61).

More quantitative results can be obtained by fitting the step-like curves with an (arbitrarily chosen) sigmoid function. We chose a function based on the complementary error function:

$$f(x) = A_1 + \frac{(A_2 - A_1)}{2} \times erfc\left[\frac{(x-\mu)}{\sigma\sqrt{2}}\right] \qquad (13)$$

Where A1 and A2 are the minimum and maximum intensity values, μ is the position of the step (between the high intensity and low intensity zones), and σ its width (standard deviation), while erfc is the complementary error function. From this analysis we can compute the average step width, corrected for the X-ray beam footprint. For this purpose, the computation is done only for those current values where the edge is clearly visible in the data to avoid fitting-induced error. As both the beam width and the step width are described by standard deviations, we can use the usual Gaussian deconvolution formula:

$$\sigma_c = \sqrt{\sigma^2 - w^2} \qquad (14)$$

Where w is the beam footprint, which for a Bragg angle of 39.7° equals 0.59 mm.

From this computation, the corrected step width σ_c evolves from 0.55 ± 0.09 mm, to 1.04 ± 0.06 mm, and to 1.3 ± 0.3 mm, for D0, D1, and D2 samples, respectively. For D3 we obtain a step value of 1.7 ± 1 mm, this error being too high for reliable evaluation. However, even without D3, these results show that for increasing the W content, the width of the boundary between the M_1 and R phase increases, in accordance with the qualitative observation above.

A tentative explanation for this behavior could be that for undoped samples a relatively high critical temperature is needed to initiate the transition. This, combined with the high angular difference between the peaks of the M_1 and R phases in the respective XRD spectra, results in an abrupt edge of the channel. On the contrary, for M_1 and R phases with higher structural similarities, the transition temperature threshold is lowered, so that the phase distribution follows more easily the temperature distribution around the conductive channel.

It is also worth noting that the difficulty in fitting the R phase of the sample D3 (Figure 76 b)) with a sigmoid stems from the above- mentioned effects of increasing similarity between the insulating and metallic phases, making data acquisition and treatment difficult at higher doping levels.

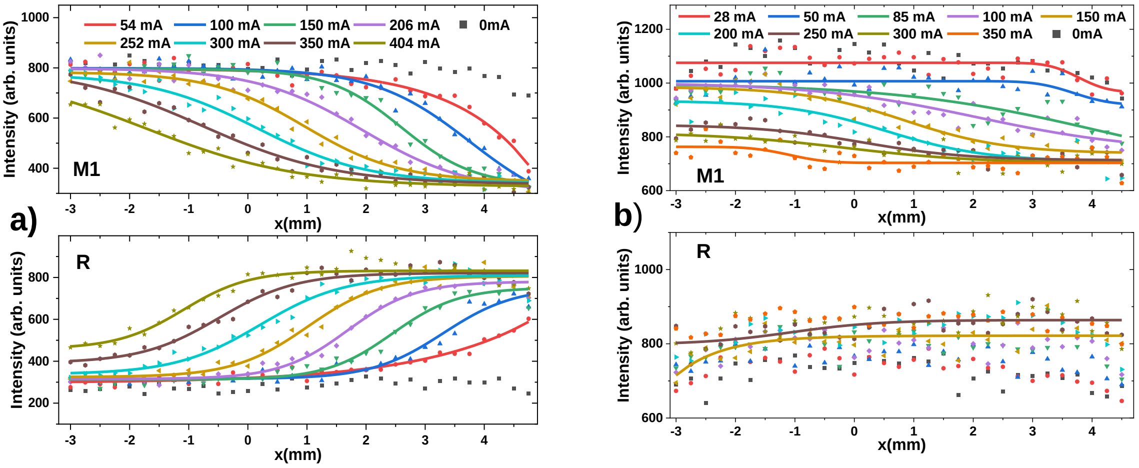

Figure 76. XRD scan along the VO_2 strip during the electrical activation of the MIT for samples with different doping levels a) D2- 1.16% W:VO_2 with a thermal bias of 25°C and b) D3- 1.86% W:VO_2 with a thermal bias of 24°C.

It can also be interesting to discuss the growth rate of the metallic channel with increasing current. As previously, we only consider electrical current values for which the step is clearly visible in the data. Figure 77 shows the linear evolution of the position of the M_1-R boundary for increasing current. From this figure, the slopes of the lines take the following values: 10.8 ± 0.4 µm/mA, 11.3 ± 0.2 µm/mA, 16.7 ± 0.9 µm/mA and 24 ± 14 µm/mA, for D0, D1, D2 and D3 samples, respectively. Disregarding the D3 value which has an error too high to be discussed, it appears that with increasing the W content the current induced mobility of the M_1/R boundary is also increasing, i.e. less current is needed to convert the whole VO_2 strip to the metallic state. Again, this feature can be traced back to increased structural similarity between the two phases.

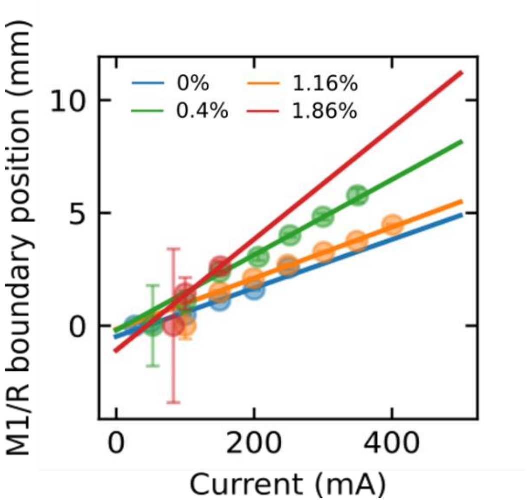

Figure 77. M_1-R boundary position at different injected currents in the devices.

After measuring the current-dependent XRD scans, current-dependent Raman measurements were performed in a similar fashion, with acquisitions performed at different points along the W:VO_2 strip. The measurements were performed on the two ends of the doping range i.e. no-doping (D0) and highest-doping (D3).

For performing the experiments on D0, the sample had to be first heated to 65°C prior to the measurements. The first measurement at 0 mA expectedly shows a scan that has M_1 Raman peaks throughout the sample. Increasing the current to 50 mA reveals a change in the intensity of the scans, indicating that the metallic channel has already been formed. This trend continues for every current step, at 100 and 200 mA.

Figure 78 shows the resulting Raman measurements scans for different positions along the W:VO_2 strip when applying a current of 100 mA on the device. This value has been chosen from the previous section where it was shown that, at 100 mA, the transition is already initiated in all samples. It can be seen that alongside a decrease in intensity as the scan position along the x direction reaches the metallic channel, a redshift of the 193, 223, and 613 cm^{-1} peaks can be seen, which is similar to the temperature-dependent Raman scans and is indicative of an intermediary M_2 phase. When comparing to the temperature-induced transition where the peaks are shifting and their intensity decreases rather abruptly, in the electrically-induced MIT the transition from the M_1 to R phase is gradual, thus the Raman features exhibit a continuous evolution towards the M_2/ R Raman modes. This gradual change has also been confirmed by the XRD scans in the previous section.

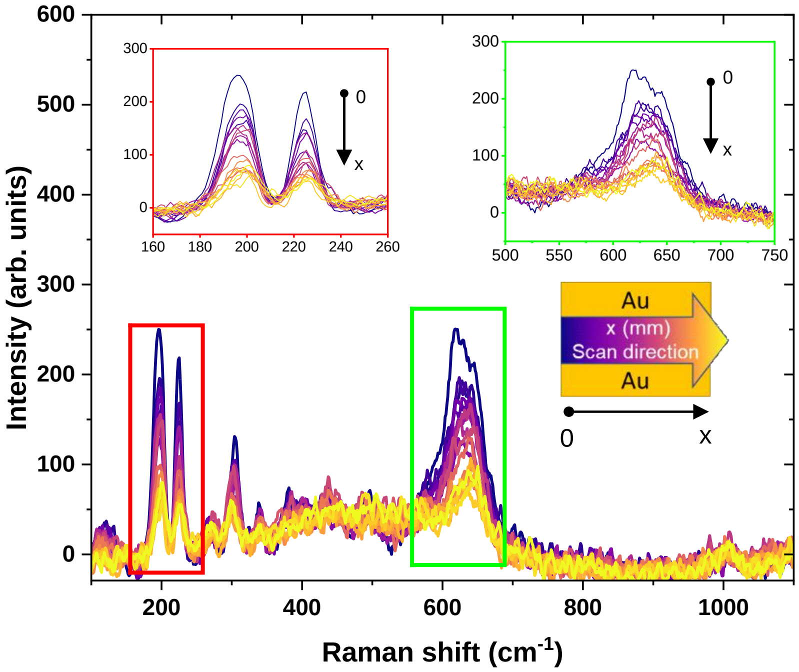

Figure 78. Raman spectra for the D0 film on which was applied a current of 100 mA, for different x positions along the VO_2 strip. Inset are the zooms on the double peaks at 195 and 223 cm^{-1} and at 613 cm^{-1} and a figure representing the scan direction, correlated with the colors of the spectra.

For D3, the sample was maintained at a constant temperature of 20°C during the electrically triggered MIT Raman experiments. As expected from the temperature-dependent Raman experiments, the peaks' intensities do not decrease for the different applied currents. The Raman shift evolution of this sample, for an applied current of 100 mA is represented in Figure 79, for different positions along the film strip. The lack of significant evolution demonstrates the structural similarity of the M_1 and R phases for this composition across the transition.

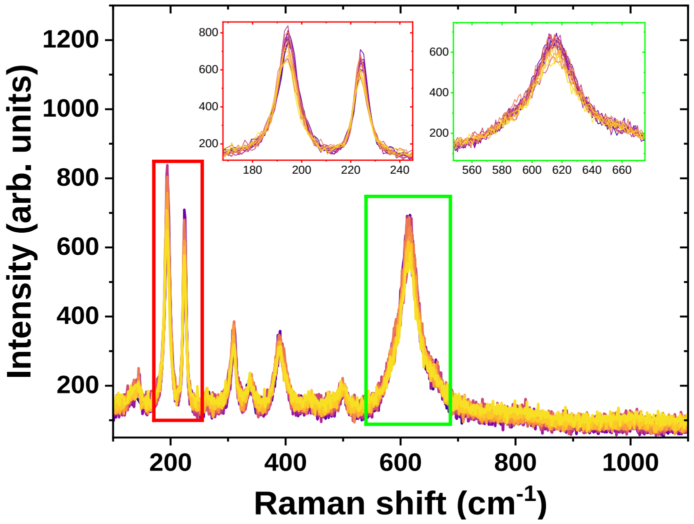

Figure 79. Raman shift evolution at different positions along sample D3 (1.86 at% W) at 100 mA.

I.1.1. Terahertz amplitude modulation

Current-dependent THz amplitude transmission measurements were also performed on the films in order to assess their THz modulating performances and compare them to the results from the thermal-activation. The setup used during the measurements is indicated in Figure 80. The sample is first mounted on the Peltier heating element with the hole in the middle to let the THz pulse through, and then the cables soldered on the electrodes are connected to the external current/ voltage source. The setup is very similar to the one for thermal activation.

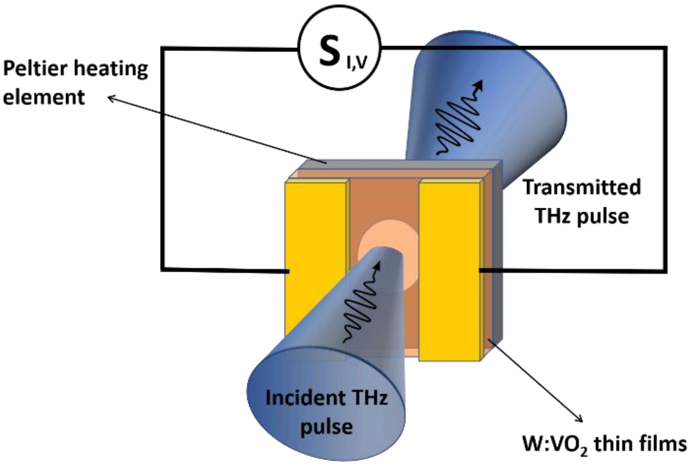

Figure 80. THz measuring setup with the W:VO$_2$ devices linked to a source that controls the electrical excitation. The samples are further mounted on a heating Peltier element with a circular hole in the center to control thermal activation and allow THz pulses to pass through.

Prior to measuring the THz transmission of the electrically activated films, a heating bias on the substrate was applied at 60°C for the undoped film, 55°C for D1, 27°C for D2, and 23°C for D3. As previously, the time-domain spectra are transformed into frequency-domain and averaged between the measured frequency of 0.2-2 THz. The hysteresis curves, shown in Figure 81, reveal the unusual behavior of some films. For example, the MIT of sample D1 seemingly occurred at a higher current than that of sample D0, and the THz transmission of sample D2 did not have a linear descent during the MIT, with a plateau occurring between 50 and 100 mA. Furthermore, the films' transmission in the metallic states did not seem to stabilize even at 250 mA. These effects can be ascribed to the position of the metallic channel's onset and evolution relative to the fixed THz pulse position as exemplified in Figure 82.

In this figure, a), b) and c) depict the scenario in which the metallic channel is initially formed beneath the position of the THz pulse (Figure 82 a)) and first expands in the opposite direction (Figure 82 b)) before finally shadowing the THz pulse with the increase in current (Figure 82 c)). In contrast, d), e), and f) show the case where the channel is formed initially covering half of the pulse, and subsequently expanding into it. It's difficult to say how the channel was formed during the THz measurements without an additional characterization technique performed simultaneously (such as thermal imaging). Either way, the control of this phenomenon could be achieved by adjusting the geometry of the electrodes. Specifically, the channel could be forced to nucleate at a given position by reducing the width and the length of the strip between the electrodes.

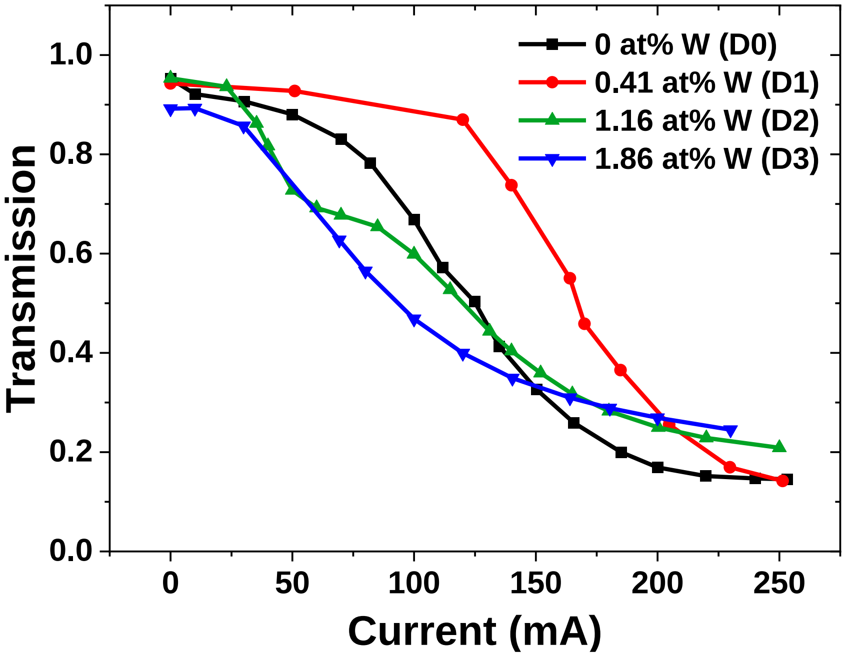

Figure 81. THz-transmission of electrically induced MIT averaged between 0.2 and 2 THz.

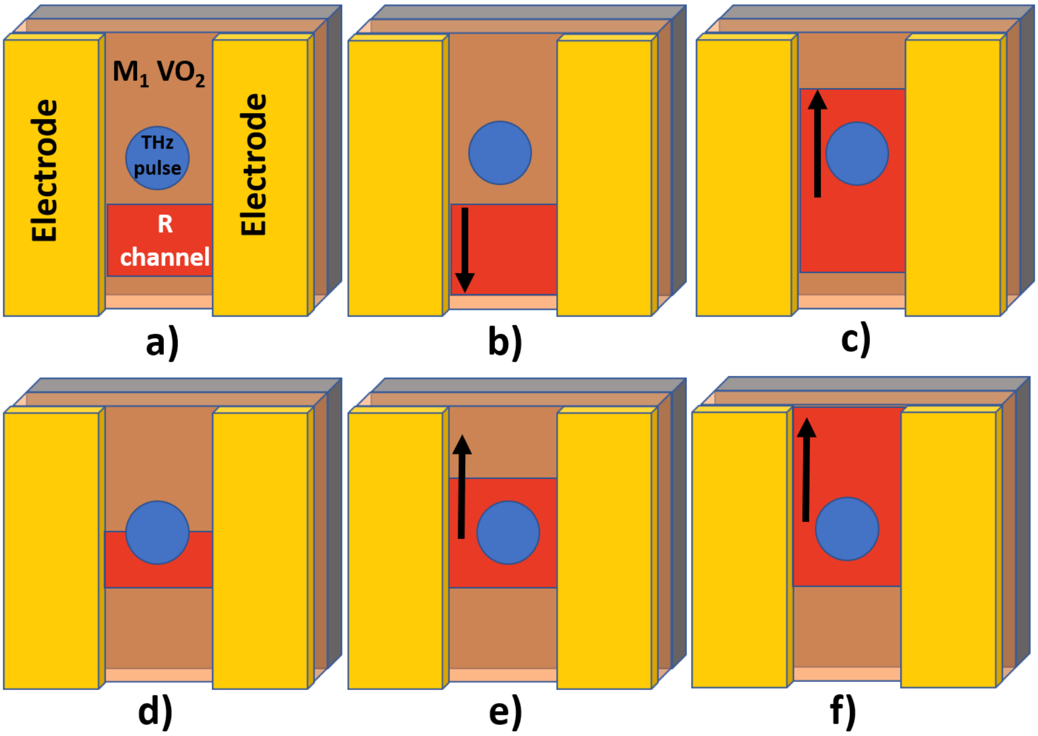

Figure 82. Electrical activation of VO_2. Possible metallic channel onset and evolution with increasing the applied current on the samples (represented by arrows) relative to the THz pulse (blue dot).

The THz modulation depths (MDs) can still be calculated and compared to the ones obtained for the thermally activated devices, as presented in Table 17. Overall, the MDs appear to be systematically lower in the case of electrical activation than in the case of thermal activation for the investigated films.

As observed in the section describing the current-dependent XRD scans, the signal coming from the M_1 peaks is persistent even at injected currents as high as 350 mA, which cannot fully be ascribed to the M_1 and R peak position's proximity. For the THz experiments, the maximum current used was 250 mA, thus a higher number of monoclinic phases can be expected to be still present in the films. This, combined with the relatively large THz pulse spot (more than ~3 mm diameter) and the uncertainty in the spatial onset of the metallic channel, leads to lower MDs.

W content (%)	MD electrical (%)	MD thermal (%)
0	84.7	96.3
0.41	84.9	88.9
1.16	78.1	85.7
1.86	72.5	79.7

Table 17. Modulation depth comparison between electrically and thermally activated W:VO2 films.

I.2. Optical activation of the W:VO_2 films

Optical activation of VO_2 is an interesting prospect for many applications, especially metamaterials for controlling the THz radiation (phase shifters [197] or modulators [198]). Activating the VO_2 films, however, requires either relatively high laser powers or has been demonstrated only on small-surface samples [199]. Tungsten doping the VO_2 films reduces the energy barrier required to trigger the MIT, thus the threshold fluences of the optical impulses are reduced [200]. As our devices have rather large areas, specific applications can be explored. For example, if the activation of the films is done near the onset of the MIT, at temperatures near and below T_{MIT}, then it is possible for the irradiated zone to remain in the metallic state after removing the optical excitation, due to the specific shape of the hysteresis curve of the VO_2 materials [201]. This allows for an optical patterning of the film made of insulating and conductive regions which behave as a sort of reconfigurable canvases, or "metacanvas" [201]. The process is illustrated in Figure 83. Initially, the films are heated up close to their T_{MIT}, with the extra energy needed to transition the film provided by the laser irradiation (operation points 1 and 2 of the hysteresis curve on Figure 83). When the laser is shut down, the irradiated region of the film remains in the metallic state due to the lower temperature of the reverse metallic-to-insulator transition (operation point 3 of the hysteresis curve on Figure 83). These changes can be seen with an optical camera, or in some cases even with the naked eye in the visible range, however, the best way to record the phenomena is by employing an IR thermal camera.

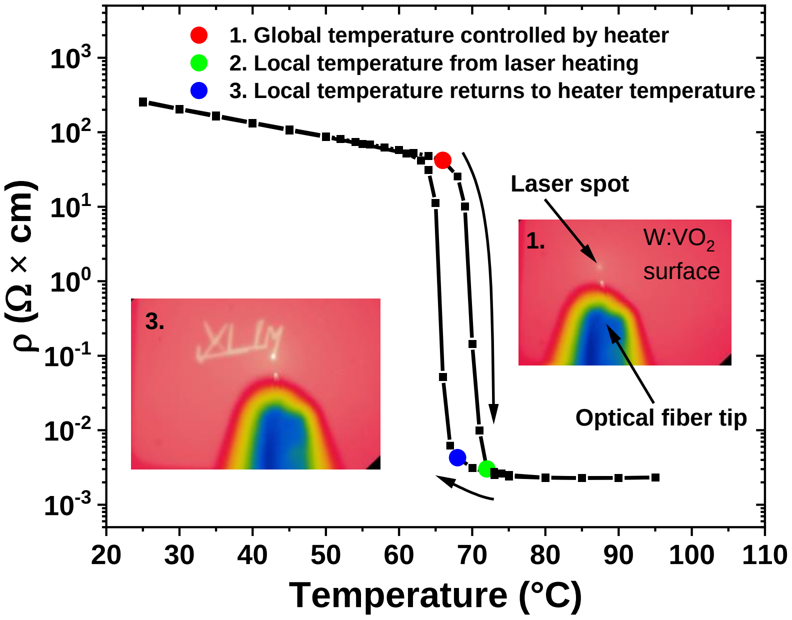

Figure 83. Mechanism of VO_2 “metacanvas” optical “writing” with inset figures exhibiting an example of manually writing XLIM word by scanning the tip of the optical fiber conveying the laser pulses on the VO_2 surface. In the example here, the sample is an undoped VO_2 film heated at 62°C irradiated with a laser operating with a power per pulse of ~1.2 W with lengths of 1 μs.

An interesting application worth exploring using this approach involves reconfigurable wire grid THz polarizers, which require thin parallel metallic wires in order to linearly polarize incident radiation. In this context, an investigation was conducted to validate this concept. For this purpose, sample D1 (0.41 at.% W), was employed as the experimental canvas for drawing.

The optical activation experiments for the $W:VO_2$ films utilized an ALPhANOV PDM2+ laser source operating at a wavelength of 980 nm. The laser source specifications include peak powers of up to 5 W, a repetition rate of up to 20 MHz, and an operational mode ranging from continuous wave down to 50 ns. As for our experiments the laser pulses lengths are set at 1 μs, and the optical triggering can be thought of as purely thermal through energy transfer from the laser to the films

Note that throughout the entirety of the study, sample D1 was held at a constant temperature of 56°C. The experimental setup (Figure 84) employed the laser operating with a power per pulse of ~0.1 W, with a repetition rate of 20 kHz, in order to manually draw parallel lines on the film surface (Figure 85 a)). The line widths were measured to be at ~100 μm, and the shortest separations between these lines were also around 100 μm. These line widths and separations are directly depending on the distance between the fiber tip and the sample surface and on the employed laser energy. It is important to note that since the lines were drawn manually, the distances between them might not be consistently uniform. After the pattern was drawn, it was left for 15 minutes in order to observe the fading behavior of the pattern while keeping the temperature at 56°C. Figure 85 b) reveals the drawn lines after this time and shows that while the lines are weaker in intensity, they are still clearly distinguished which indicates a good short-time stability of the films.

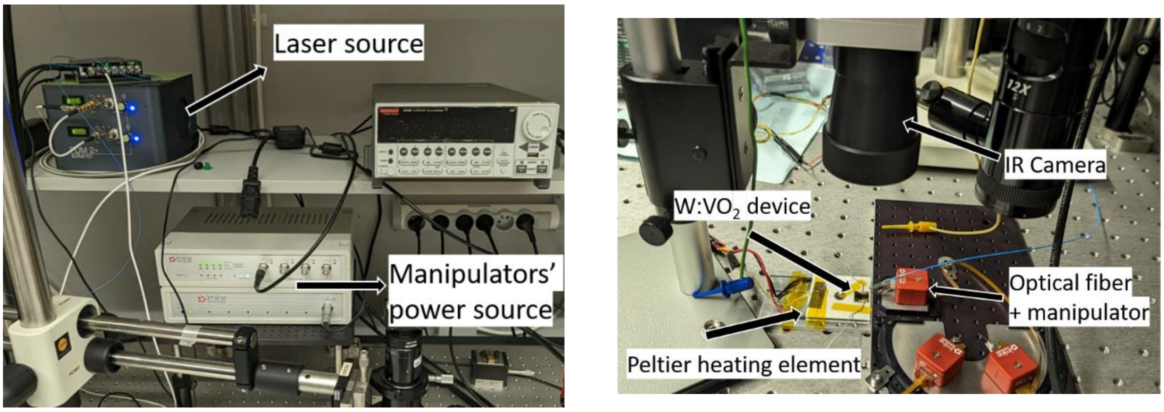

Figure 84. a) Image of the setup with the laser source and manipulator's power source and b) optical activation setup with all the elements.

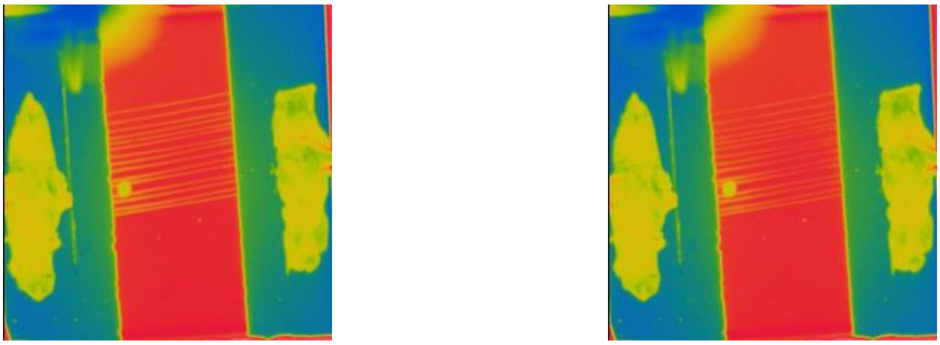
a) b)

Figure 85. IR thermal images recording the periodic lines optically drawn on sample D1 kept at 56°C a) initially b) 15 minutes after removing the optical irradiation.

Following the 15-minute period after removing the optical excitation for studying the fading behavior of the written lines, a current was applied through the metallic electrodes across the thin film in order to study the evolution and behavior of the written area under increasing applied current. This evolution is represented in Figure 86. Initially, at an injected current of 15 mA, the lines become more clearly distinguished and their intensity increased. This effect continued at 30 mA and, from the color change, it was deduced that the lines act as nucleation points for the rutile metallic phases. Rather interestingly, as the applied current was incrementally increased from 50 to 150 mA, a transformation to the metallic state was recorded to emerge from the edge of the sample forming a new conductive region (Figure 86 c)), while the lines do not seem to increase in width. Upon increasing current the lines started to be incorporated in the new metallic region (Figure 86 d)). It is still unclear why the overall metallic phase did not emerge directly from the already optically drawn patterns. Additional work needs to be performed in order to ensure that this effect is not specific to this sample, as the metallic channel formation for the D1 sample was seen emerging from the sides of the sample also in the normal electric activation, without laser patterning.

Decreasing the current reveals that the optically drawn lines are still somewhat visibly separated, indicating a "memory" effect of the sample. Reducing the temperature to 55°C (not shown here) successfully erases the lines and the films become fully insulating again. This "memory" effect could be explained by the fact that the film is still in the lower branch of the electrical-hysteresis curve, confirmed by the presence of various colors (different emissivity points) on the sample. The fact that the laser drawing remains visible could very well be due to the higher concentration (surface and bulk) of the R phases from the focused optical radiation.

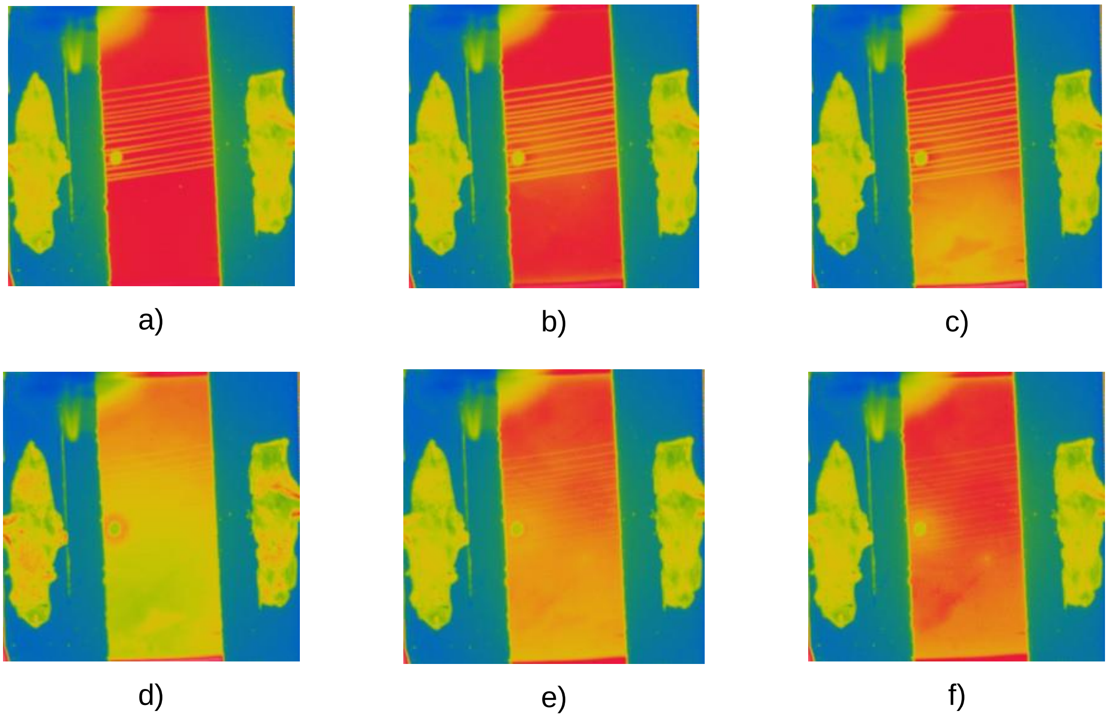

Figure 86. Thermal IR images of film D1 (0.41 at% W), maintained at a constant temperature bias of 56°C, showing periodic lines drawn by a laser, under various current conditions: (a) 15 mA, (b) 30 mA, (c) 50 mA, and (d) 150 mA for increasing current, and (e) 25 mA and (f) 0.01 mA for decreasing current.

This experiment holds promise for future devices utilizing reconfigurable surfaces, where optical triggering of the transition is more advantageous for controlling the MIT over electrical methods, particularly in large-area applications. Nevertheless, because of time constraints, some critical refinements are missing e.g. finding deposition and doping conditions that allow for an abrupt MIT transition at relatively low temperatures in order to allow low laser fluences to activate the film. Also, the minimum resolution of the width/ separation between the drawn lines would require characterization methods with greater precision than the IR camera used for this research (e.g. in-operando Raman spectroscopy, SNOM- scanning near field optical microscopy, conductive AFM, etc.)

Similar experiments were also performed on samples D0, D2, and D3. It was found that for D0 and D2 devices the required laser current/ frequency to activate the MIT strongly depended on the film temperature, fiber-laser tip distance from the substrate, and incidence angle of the laser beam with respect to the sample surface. These factors also influenced the fading and “memory” effect observed in the experiments. For the most W-doped sample, D3, the IR camera didn't pick up any changes (i.e. no pattern could be observed upon laser irradiation), regardless of the laser settings (pulse width, energy) or the sample’s temperature (between 10°C and 20°C). This is in line with the result obtained for the electrical activation of the transition, where no visible filament was formed during the transition.

I.3. Conclusion

In this chapter, we discussed the electrical and structural characteristics of tungsten-doped VO_2 films. The films were fabricated using reactive DC magnetron sputtering by placing W chips on the metallic vanadium target. By varying the chip size, the resulting W doping amount in the VO_2 layers could be controlled. A standard annealing step (550°C for 30 minutes) was subsequently applied on the films. The W amount inside each sample was measured by employing the RBS technique, revealing that the samples, named D0, D1, D2, and D3 for increasing W content, presented 0, 0,41, 1.16, and 1.86 at% W. Their temperature-dependent electrical resistance was measured using the four-point probe technique. It was shown that as the tungsten percentage increases, the T_{MIT} decreases with a slope of 18.9°C ± 2.9/ at% W, which is similar to reports in the available literature. The overall width and the hysteresis width of the transition, ΔT and ΔH, increased with the W doping level, which could be due to a decrease of grain size, possibly from the increased doping-related nucleation sites. The resistance ratio between the low and high temperature phases decreased heavily, from five orders of magnitude for D0 to only one for D3, mostly due to a decrease of resistivity in the insulating phase.

θ-2θ XRD scans on the samples revealed that as the doping amount increased, the 020 peaks shifted towards lower angles, signaling an increase of the lattice parameter relative to the undoped samples. Temperature-dependent XRD scans around the VO_2 020 peak revealed a decrease in spatial separation between the R and M_1 phases. This structural distortion of the M_1/ R phase was interpreted as the main reason for the T_{MIT} reduction in literature, as the energy needed to overcome the energy barrier between them is reduced.

Raman spectroscopy measurements revealed that at room temperature all films have peaks typical to the M_1 phase, regardless of doping. Temperature-dependent scans of samples D0 and D3 revealed that for sample D0 a peak shifting linked to the transition of the M_2 phase was seen around the T_{MIT}, and after the T_{MIT}, all the M1 features disappeared, typical to a transition to the metallic phase. In the case of D3, the film revealed typical M_1 signals well after its transition temperature, indicating that the high-temperature R phase had undergone a distortion towards a configuration resembling M_1.

THz-TDS was employed in order to assess the W-doping influence on the temperature-dependent THz amplitude transmission. It was revealed that even for D3 (1.86 at% W) the modulation depth (MD) was ~80%, averaged between 0.2 and 2 THz. This is a relatively high MD when compared to other bare-VO_2 films in literature proving the high quality of the films.

Furthermore, in order to study the electrical activation of the films, Au electrodes were fabricated on the W:VO_2 films leaving a 3.8 mm strip of material in the middle. Such large areas relative to other devices proposed in literature, were fabricated in order to allow electrically-triggered THz-TDS evaluation of films' performances.

The electrical activation of the films was observed using an IR thermal camera. It was revealed that the transition was characterized by the onset of a well-delimited metallic channel that increased in width with increasing the applied current. For the samples with higher W amounts, this metallic channel was not as obvious to detect from the IR thermal imaging. In order to better characterize the onset and evolution of the metallic channel, current-dependent XRD characterizations were employed by performing scans from end to end along the W:VO_2 strip for the diffraction conditions of the M_1 and R phases. These measurements allowed us to quantitatively characterize the conducting channel during the injection of electrical currents in the device. It was demonstrated that with increased doping, the spatial M_1/R boundary became more diffuse and that the metallic channel growth rate increased.

Current-dependent Raman scans were also performed in a similar fashion. In the case of D0, as the scan position approached the electrically-formed metallic channel, a gradual shifting of the specific Raman peaks (similar to the temperature-dependent scans) was observed. For D3, a similar but significantly smaller blue shift of approximately ~1 cm^{-1} was observed for the 193 and 223 cm^{-1} peaks.

Current-dependent THz amplitude transmission measurements revealed that the position of the channel onset, and subsequent evolution with current, heavily influenced the shape of the THz transmission modulation. The MDs were also generally lower than the temperature-dependent ones. Changing the form of the electrodes from parallel to other shapes that have reduced distances where the channel is desired to trigger should alleviate the THz transmission performances.

Finally, within this chapter, the optical activation behavior of the films was explored. Exploiting their temperature hysteresis behavior, the films were heated close to their T_C followed by localized heating using laser radiation. After the laser spot was removed, the area returned to the fixed temperature, however, due to the shape of the temperature hysteresis curve, the irradiated area remained in the metallic state.

In order to test possible applications of reconfigurable wire grid polarizers, relatively equidistant lines were drawn on D1 with ~100 μm widths and distances between the lines. The results show promise for building dynamic systems based only on optical writing, such as photonic circuitry or reconfigurable metasurfaces. Furthermore, multi-stimuli applications can be created utilizing these films i.e. using thermal + optical triggers to create patterns on the surface, and utilizing electrical current to maintain these patterns while removing the heating.

Chapter V. Niobium dioxide thin films: fabrication and characterization

In this work we made important progress on NbO_2 in order to reach a higher understanding of this high transition temperature metal-insulator transition material, as it is an interesting research topic alongside VO_2 and W-doped VO_2. However, due to the relatively limited body of existing literature on NbO_2, combined with some intriguing findings of our researches stemming from VO_2 and W:VO_2, which demanded considerable time to characterize and understand, there remains numerous unanswered questions regarding the fabrication process and its effects on material properties in our investigations of NbO_2. Despite these challenges, this chapter will provide an account of the progress achieved so far in the fabrication of thin layers of NbO_2 obtained by reactive magnetron sputtering, as well as their electrical and thermal characterization.

IV.1. Optimization of the fabrication process

The optimization process for obtaining high-quality NbO_2 films was performed in a similar fashion to the one used for the VO_2 films. The first step, before fabricating the films, was finding the optimal O_2 deposition flow for obtaining the desired NbO_2 stoichiometry. An oxygen poisoning curve, as described in chapter 3.1, was established for this purpose as well. To quickly recall, the oxygen flow within the overall flow of Ar+O_2 gasses mixture was increased continuously and the plasma voltage noted at each increment. Unlike the VO_2 experiments however, two different magnetron sputtering systems/ chambers were used to perform the NbO_2 deposition experiments. The first one (Plassys) was also used for performing the VO_2 thin film synthesis, the second one (PVD-6 from Vinci Technologies) was a new deposition system. This new system offers numerous advantages in comparison to the previous one. Notably, it incorporates separate shutters for the target and the substrate and the possibility to simultaneously perform RF, DC and pulsed DC magnetron sputtering. This double-shutter configuration enables the plasma to stabilize with the target shutter open and the substrate shutter closed, unlike the Plassys system. Thus, the plasma remains stable upon the initiation of the deposition process. Furthermore, the new system ensures uncontaminated chamber walls due to exclusive usage of niobium deposition (at the time the experiments were performed), preventing potential cross-contamination from other experiments. Still, as this second deposition system arrived towards the end of the thesis, additional work is needed in order to optimize the fabrication process and to analyze the films obtained under different experimental conditions.

The sputtering deposition conditions for the PVD-6 system involved a constant 50 sccm Ar flow with a variable oxygen flow to achieve a total chamber pressure of 2.25 mTorr. The Plassys system, on the other hand, used a constant 70 sccm Ar flow with a variable oxygen flow to maintain a total chamber pressure of 4 mTorr. In both systems, a sputtering power of 150 W was employed. The resulting oxygen poisoning curves for the two systems are presented in Figure 87. These curves are quite similar to each other, and it is also clear that, unlike the VO_2 targets (especially the T2 target), the poisoning curves for NbO_2 exhibit a more gradual evolution, with a large transition zone. This can prove useful in controlling the film stoichiometry without worrying about avalanche effects that would abruptly destabilize the plasma.

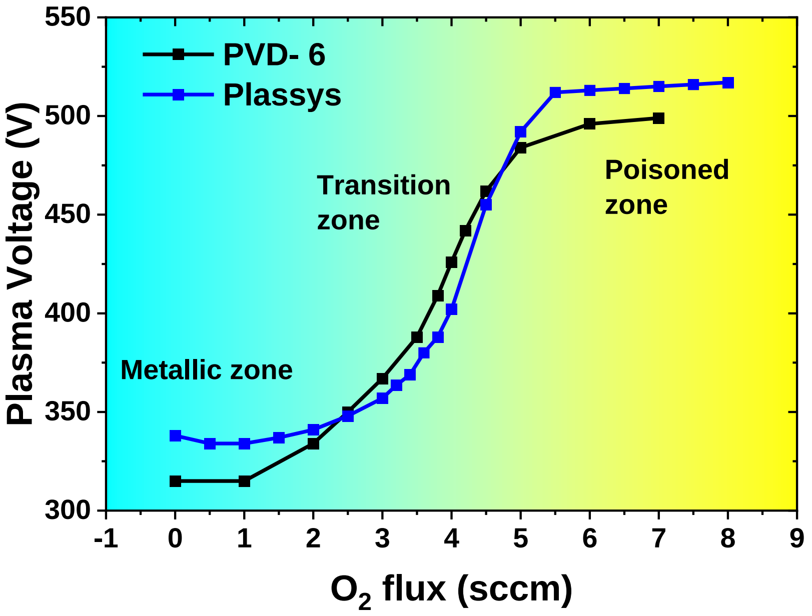

Figure 87. Oxygen poisoning curves of an Nb target for the two deposition systems (Plassys and PVD-6).

In the following sections, we will discuss the details of the NbO_2 fabrication optimization using the curves shown on Figure 87. Specifically, we will analyze the oxygen flow operation values associated with the endpoints and the transition zone of the curve for the Plassys system. For the PVD-6 system, our focus will be on exploring the operation values related to the transition zone.

IV.1.1. Deposition optimization using the Plassys system

The Plassys system was employed to deposit thin films on c-Al_2O_3 substrates. For all depositions an Ar flow of 70 sccm for a total chamber pressure of 4 mTorr, and a sputtering power of 150 W were utilized. The films were deposited at various oxygen flow rates, specifically 0, 3.8, 4.5, and 7 sccm of O_2, while maintaining a substrate temperature of 500°C. XRD θ-2θ scans of the as-deposited films are presented in Figure 88 a) between 15 and 95° and in b) between 32° and 40°, in order to focus on the NbO_x diffraction peaks.

In the case of the films fabricated at 0 sccm O_2, the observed diffraction peaks are attributed to the pure Nb phase with peaks present 38.52°, 69.46° and 82.69° corresponding to the (110), (211) and (220) Nb planes (PDF 00-034-0370). For the samples fabricated under 3.8, 4.5 and 7 sccm O_2 flow, similar patterns are observed, with peaks emerging at ~35° and ~37° corresponding to the (222) and (440) NbO_2 planes (PDF 04-005-4298). Increasing the oxygen flow from 3.8 to 4.5 sccm leads to more intense NbO_2 diffraction peaks, indicating an increased crystalline quality. The observed peak shift points to a variation in the level of strain or in the oxygen content of the film. Surprisingly the film fabricated at 7 sccm O_2 presented a diffraction pattern similar to the one at 3.8 sccm O_2. This sample also differs by its visual aspect, it has high transparency thus it can be speculated that alongside the NbO_2, an amorphous Nb_2O_5 phase is also present. This assumption is based on experiences with Nb-O films fabricated at high oxygen flow that showed no XRD peaks, thus amorphous.

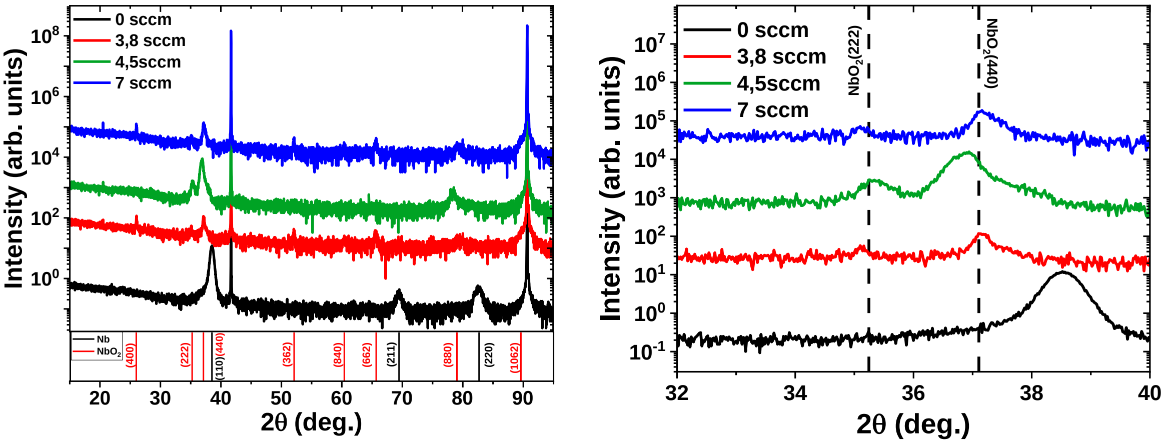

Figure 88. XRD θ-2θ scans of NbO_2 films deposited at different oxygen flows between a) 15° and 95° and b) 32° and 40°.

With the prospect of improving the stoichiometry and crystal orientation, a post-deposition annealing step was also performed with the same conditions used for VO_2 i.e. 550°C, 20 sccm O_2 for 30 minutes. As the sample at 7 sccm O_2 was already transparent, indicating a possible domination of the insulating Nb_2O_5 phase, XRD measurements were not pursued for this sample after the post-deposition annealing. The post-annealing θ-2θ scans of the other samples are presented in Figure 89. It can be seen that the film deposited at 0 sccm O_2, pure Nb deposition, underwent a phase transformation to NbO_2, indicating the successful incorporation of oxygen into the film. However, a very broad shoulder appearing at a lower angle, near the NbO_2 one, can also be seen, which could not be precisely attributed to any specific phase. For both the films deposited at 3.8 and 4.5 sccm O_2, the annealing step lead to increased peak intensity of the ones at 35° and 37°, signifying an increase of crystallinity and/ or orientation.

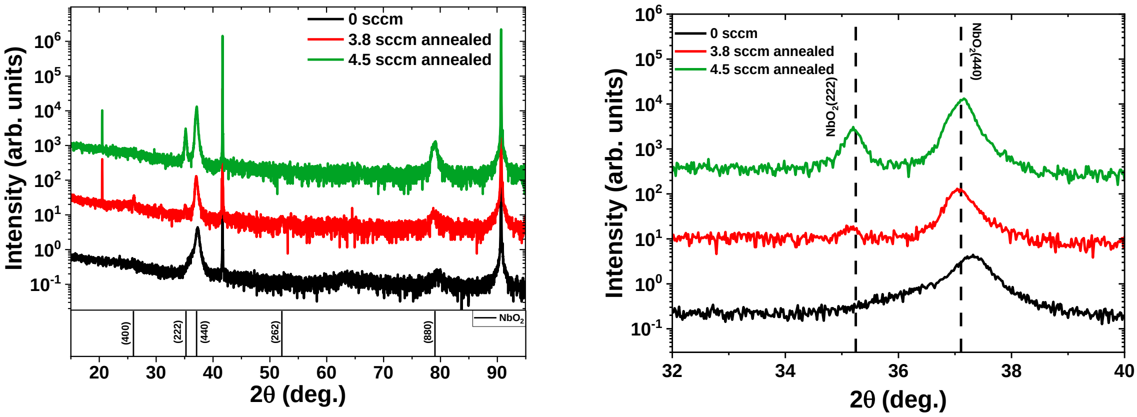

Figure 89. XRD θ-2θ scans of annealed samples a) between 15° and 95° and b) between 32° and 40°.

Grazing incidence XRD results are shown in Figure 90 a) for the as-deposited samples and b) after their annealing step. It can be seen that for the as-deposited films at 0 and 3.8 sccm of O_2 the data exhibits several diffraction peaks that can be attributed to Nb, NbO_2 or Nb_2O_5. This is an indication that these films are not oriented in a single direction. The samples deposited at 4.5 and 7 sccm O_2 lack any significant diffraction peaks in the GI-XRD data which shows either the appearance of an out-of-plane texture (as confirmed by the θ-2θ scan in Figure 89 for the 4.5 sccm case), or, in the case of the 7 sccm O_2 sample, a possible amorphization of the film, also due of the decreased intensity in the θ-2θ scans.

Following a post-annealing process, the phase transformation of the films is evident in the GI-XRD scan. In the case of the sample created at 0 sccm O_2 flow, the prominent peak observed at around 36.75 degrees may arise from the overlapping of two NbO_2 peaks. This overlap could be influenced by distorted grain structures, causing broadening of the peaks. The sample at 3.8 sccm O_2 showed less intense peaks than the as-deposited one, indicating that the annealing step helped with increasing the film's orientation. The film deposited at 4.5 sccm O_2 shows almost no peak in the GI-XRD data indicating the lack of any disoriented fraction, i.e. a good film orientation.

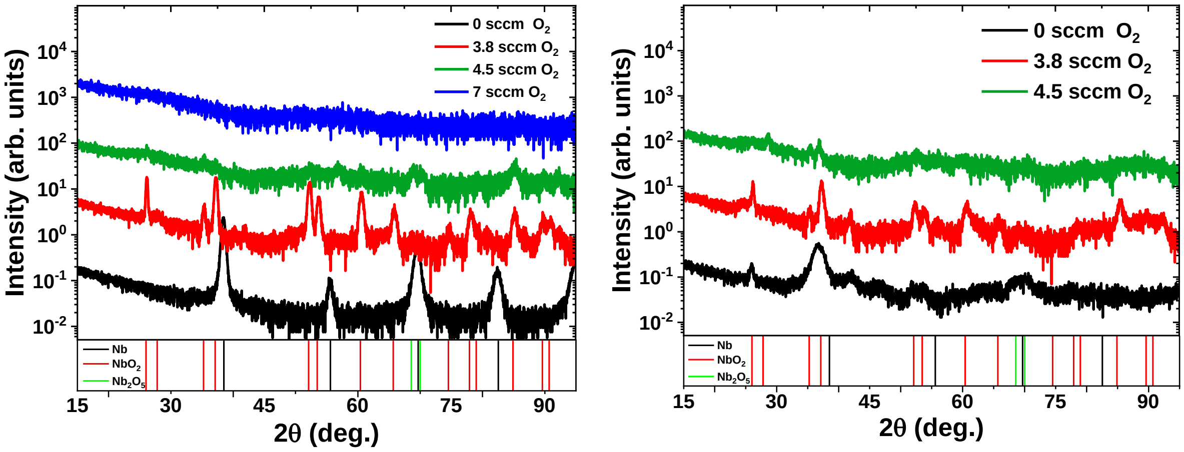

Figure 90. GI-XRD 2θ scans of the NbO_2 samples deposited at different oxygen flows for a) as-deposited films and b) oxygen annealed films.

IV.1.2. Deposition optimization of NbO_2 films using the PVD-6 system

For the PVD-6 system, the investigation focused on intermediate experimental conditions with regard of the oxygen flows, as the extreme cases (0 and 7 sccm O_2 flow) were studied in the previous section. Films were produced with oxygen flows of 2.5 and 3.5 sccm. For the PVD-6 system, the sputtering conditions were 50 sccm Ar, for a total pressure of 2.25 mTorr, and a sputtering power of 150 W. In this case, the deposition temperature was of 650°C and the post-annealing step was performed at 750°C, as it was noticed from other experiments (not shown here) that a higher deposition and annealing temperatures led to a higher degree of crystallinity of the obtained films i.e. more intense diffraction peaks in the θ-2θ scans.

The resulting XRD θ-2θ scans of the films obtained under these conditions are presented in Figure 91 a) for the as-deposited films and b) for the annealed ones. It can be seen that before the post-annealing step, both films present similar diffraction patterns with peaks appearing at ~36.39° and ~77.27°. With just the θ-2θ scan it's rather difficult to assign these peaks to any specific phase, as between 36-37° diffraction peaks from NbO, NbO_2 or Nb_2O_5 are present in the powder diffraction files. However, with the help of diffraction pattern of the 2θ GI scan, the assignment of the phases was made easier since most of the peaks (Figure 92 a)) superimposed satisfactorily with the ones from NbO. Thus, the peaks in θ-2θ scan could be attributed to the (111) and (222) NbO planes (PDF 00-042-1125).

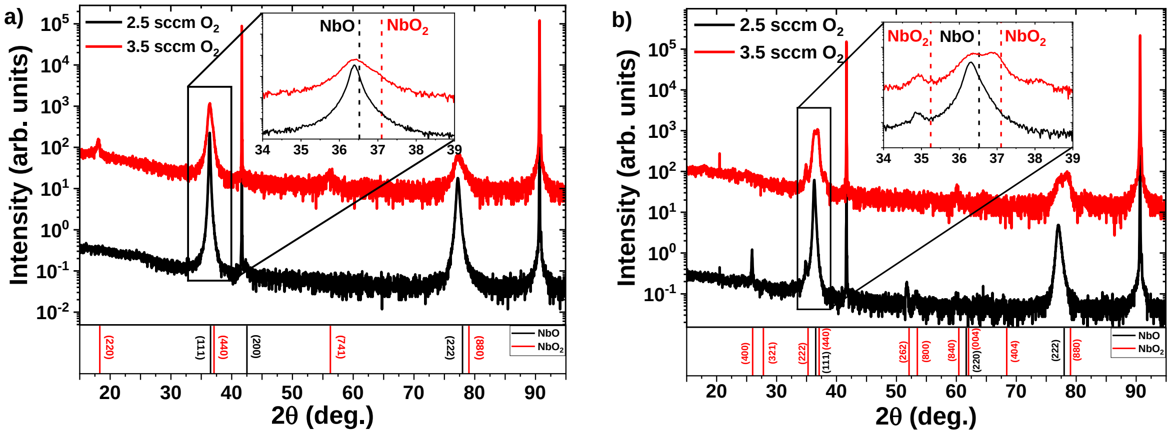

Figure 91. XRD θ-2θ scans of a) as-deposited and b) annealed films sputtered from a Nb target using the PVD-6 system.

The sample fabricated at 3.5 sccm O_2 shows additional peaks at 18.01° and 56.11°, the first one being assigned to the (220) NbO_2 plane, while the other one could not be confidently assigned to any phase, but, most probably comes from the (741) NbO_2 plane. Furthermore, for this oxygen flow, another peak at ~37°, slightly superimposed with the one of 111 NbO could be seen. This peak has been attributed to the (440) plane of NbO_2, showing that an as-deposited NbO_2 phase can be obtained at higher oxygen flows.

After performing the post-annealing step, it can be seen that both the θ-2θ (Figure 91 b)) and GI 2θ scans (Figure 92 b)) revealed peaks assigned to NbO_2 phase. Furthermore, it is interesting to note that while in the GI scans the post-annealing pattern of both films is similar to the one of the NbO_2 films deposited in the Plassys system, in the θ-2θ scans the 111 NbO peaks are barely shifted. It is possible that the oriented part of the NbO (i.e. the (110) plane family) did not transform under the post-annealing step, which might be due to the NbO being epitaxially grown on the substrate. Another point of interest is the (440) NbO_2 peak of the films grown at 3.5 sccm O_2 flow. In the as-deposited film, the intensity from this plane was quite weak. However, after annealing, it became as intense as the 111 NbO peak. This phenomenon might be attributed to the grains in this phase acting as nucleation centers for NbO_2 during the annealing process.

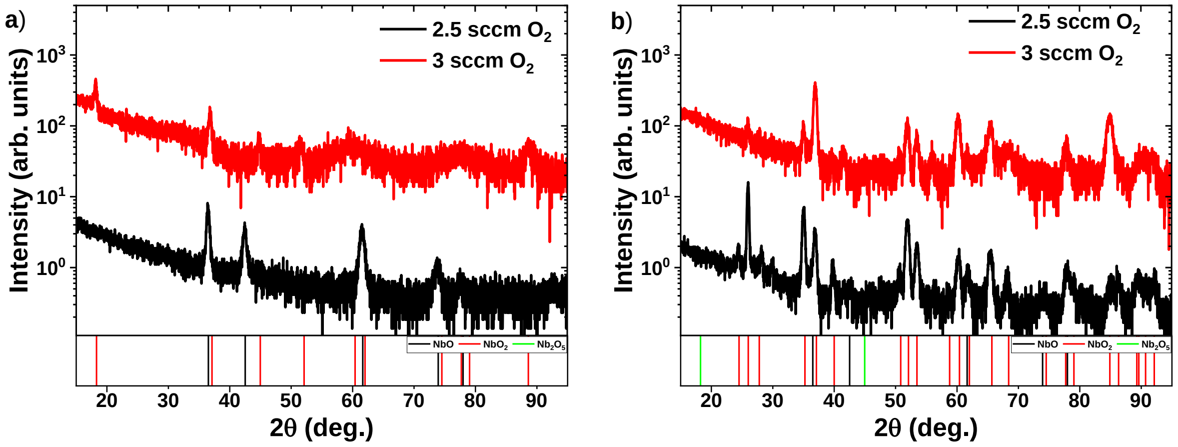

Figure 92. XRD 2θ (GI) scans of a) as-deposited and b) annealed films sputtered from a Nb target using the PVD-6 system.

The results presented in the previous sub-chapters have provided valuable insights into the fabrication process of NbO_2 thin films. While consistent steps have been taken in unraveling the optimization of NbO_2 deposition, further efforts are required especially for the PVD6 system which is a superior sputtering system in terms of capabilities (separate substrate and target shutters, possibility for co-deposition). The goal is to achieve mono-oriented films similar to those of VO_2 presented throughout this work. Additional directions for optimization include identifying better deposition and annealing temperature, optimizing the deposition oxygen flow, and even exploring the use of alternative substrates. These efforts will contribute to advancing the fabrication process of NbO_2 films.

IV.2. Electrically induced activation of the NbO_2 films

This section focuses on studying the electrical activation of the NbO_2 films fabricated using the Plassys system. Given that there is less ambiguity around the nature of the films deposited at an oxygen flow of 3.8 sccm O_2 (i.e. phase composition), this experimental condition was taken as the optimal one for the given time. In order to test the switching behavior of the material under an applied voltage/ current, we integrated NbO_2 in simple metal-insulator-metal (MIM) vertical devices.

The devices were fabricated by sputtering a Pt layer as bottom electrode on a c-cut sapphire substrate (20x20 mm^2). An NbO_2 layer of 269 nm was fabricated under normal deposition and annealing conditions on two thirds of the sample surface in order to give further electrical access to the lower electrode. Afterwards, a photolithography step was used in order to fabricate top electrodes with different dimensions made of Ti/ Au layers of 10/ 200 nm thicknesses, obtained by e-beam evaporation followed by lift-off. The fabricated MIM devices are schematically shown in Figure 93 a) and an image from the top showing different top-electrodes MIM device dimensions is depicted on Figure 93 b). The upper electrodes have square shapes with sides of 30, 40, 50, 60 and 70 µm. For the electrical probing, the devices were connected in series with current/ voltage measurement unit and a resistance of 220 Ω in order to prevent damaging them in the low resistive state. An oscilloscope could also be connected in parallel with the resistance in order to measure the film's response to the electrical activation or further, the onset of electrical oscillations.

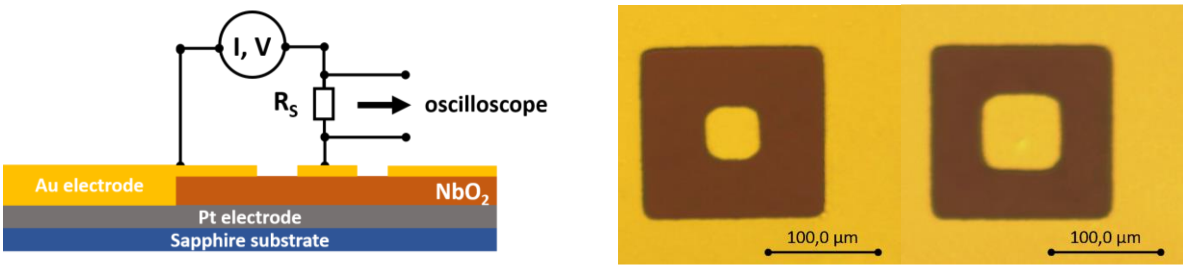

a) b)

Figure 93. Schematic of the metal-insulator-metal vertical NbO_2 device and the associated electrical setup for MIT activation and b) top view of an MIM device with upper electrodes of 50 µm (left) and 70 µm (right) lateral size.

Additionally, it is of interest to observe how NbO_2 grows on the Pt-covered c-sapphire substrate (experiments that may need further optimization on their own). Figure 94 presents the diffraction pattern of the NbO_2 film/ bottom Pt electrode/ substrate heterostructure. While the high-intensity peaks can be attributed to the Al_2O_3 substrate and Pt layer, the other peaks seem to result from the superposition of multiple Nb-O phases. Although, based on the other sputtered films at this oxygen flow value, it is safe to assume that the phase is indeed NbO_2 and that the largest peak comes from the (440) plane. Furthermore, from the GI XRD scan (not shown) we may confirm that Pt grows oriented on the sapphire substrate. Further insights into the nature of the film may be deduced from its electrical switching characteristics.

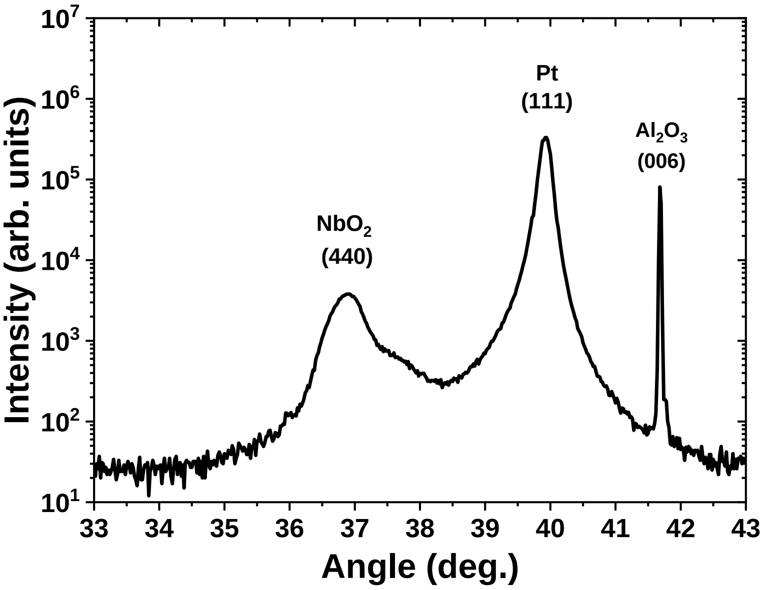

Figure 94. XRD θ-2θ pattern of a NbO_2 film grown at 3.8 sccm O_2 on a Pt-covered c-Al_2O_3 substrate.

The current-voltage (I-V) characteristics of a NbO_2-based MIM device with a top-electrode side dimension of 40 μm are presented in Figure 95 a) and b) for the voltage and current sweep modes, respectively. It can be seen that in both cases the film presents a threshold voltage/ current jump with corresponding NDRs, and a hysteresis when returning to the initial insulating state. Even though our films are most probably polycrystalline NbO_2 and no electroforming step was noticeable (as it was shown that electroforming may not necessarily appear for crystalline NbO_2 [93,202,203]), the resistance of the insulating state dropped after the first electrical switching event was performed, especially for the devices with larger top-electrodes (50 and 60 μm), as it can be seen in Figure 96.

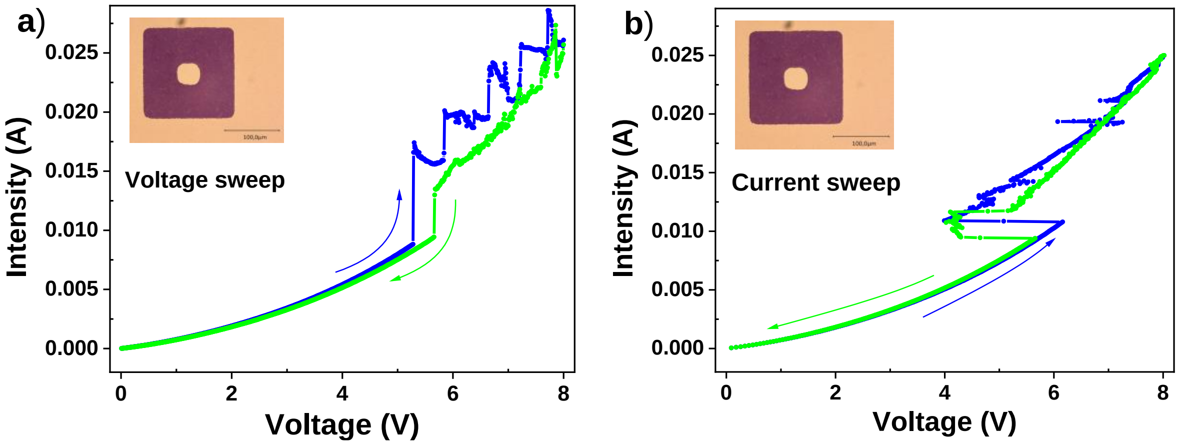

Figure 95. Current-voltage curves subsequent to a) voltage and b) current sweeps applied to the NbO_2 MIM device with an electrode side dimension of 40 µm.

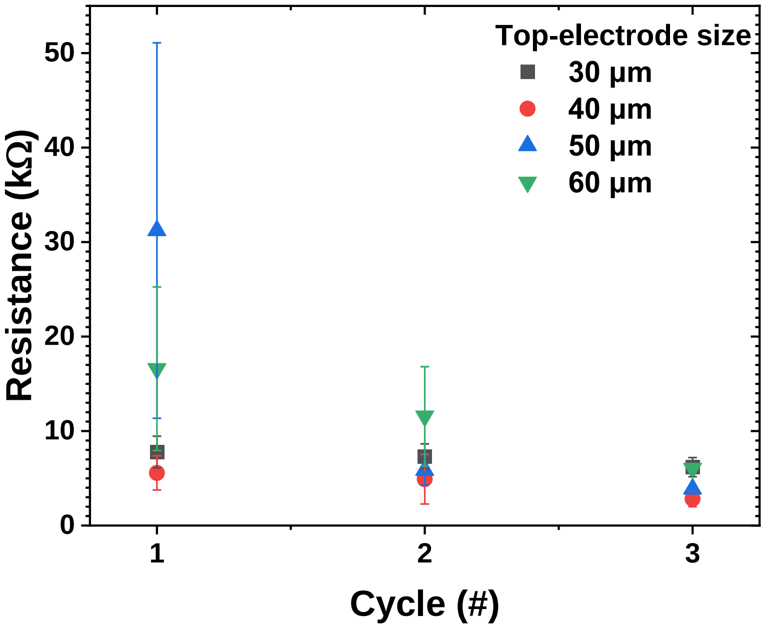

Figure 96. Initial resistance of NbO_2 MIM devices with different top-electrode sized for different cycles.

The resistive switching mechanism may occur either through a filamentary type switching, where a non-volatile conductive filament is formed in the films [204] or an interface type, where the charges are gathered near the metal electrode, in the film [205]. The filamentary type conduction is weakly depended on the electrode areas, while the interface type is heavily influenced by them. In volatile MIT materials this filament is created by grains switching into the metallic phase, as discussed in the previous chapter. In our case, the threshold current seems to be depended on the electrode size (as indicated in Figure 97). The fact that the device resistance decreased after the first measurement cycle could point to a combination of a permanent filament being formed (electroforming) and an MIT-induced switching. When measured immediately after fabrication, the switching could be obtained only on the top-electrodes with side dimensions from 30 to 60 µm, with the MIT on the 70 µm electrode not being possible.

It is reported in literature that NbO_x films can have two NDR regions when the MIT is electrically triggered [14,16]. The first one is related to a Poole-Frenkel conduction mechanism which gives and S-type NDR and is triggered at an equivalent temperature much lower than the expected MIT of NbO_2, namely ~400K. The second NDR is related to the MIT of NbO_2, defined by a snapback type mechanism/ abrupt jump, and is triggered at a temperature of ~1000K. Although the S-type NDR is usually seen in amorphous Nb_2O_5, NbO_x and NbO_2 films, Lee et al. reported the combined S-type and snapback NDR in crystalline NbO_2 when the bottom electrode sizes were over 520 nm [202]. Our films, as can be seen in Figure 95 and Figure 97, present only one NDR at around a voltage threshold of 6 V and show a large jump in voltage and a hysteretic behavior when returning to the insulating state. From this it can be deduced that this NDR is indeed due to the NbO_2 MIT, while the other mechanism was not seen in our films.

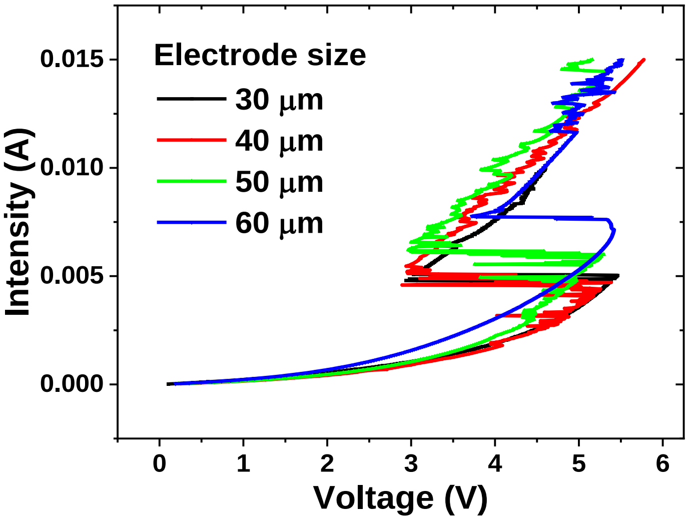

Figure 97. NbO_2-based MIM current-based electrical activation for different electrode side sizes.

After ~10 months, the MIM devices were measured again in order to evaluate the influence of aging on the films and evaluate the onset of the voltage oscillations behavior initiated when exciting the device with a constant current in the NDR region. It was found out that the switching characteristics of the devices were very different, with high level of fluctuations and low repeatability between measurements. Also, electrically induced MIT has occurred on all electrodes, even on the one with side dimensions of 70 µm. This could be due to the fact that for these experiments, the resistance connected in series had a value of 100 Ω. Figure 98 shows the current-induced switching characteristics of a device with electrode side sizes of 60 µm after two consecutive measurements. It can be seen that both the switching voltage and hysteresis shapes are different. Additional measurements on devices with different electrode sizes reveal similar unstable switching curves. Regardless, this proves that the film still exhibits an MIT even after 10 months of aging. Another effect that needs to be considered is the film oxidation. It is possible that, even though the films were kept under vacuum, oxidation of the film had taken place, with a thick Nb_2O_5 layer forming on the exposed surface. Although oxidation quickly happens, at low enough thicknesses of Nb_2O_5 the influence on the electrical switching can be minor [206]. However, it is not known how the electrical performances of the devices are affected if this oxidized/ dielectric layer becomes thicker. It could alter the functioning behavior by forming conductive filaments in the Nb_2O_5 and affecting the volume of NbO_2 that undergoes transition [207]. More understanding of this phenomenon could be gained by performing RBS analysis or cross-sectional electron diffraction analysis on fresh and aged NbO_2 devices, to reveal the composition at different distances from the surface.

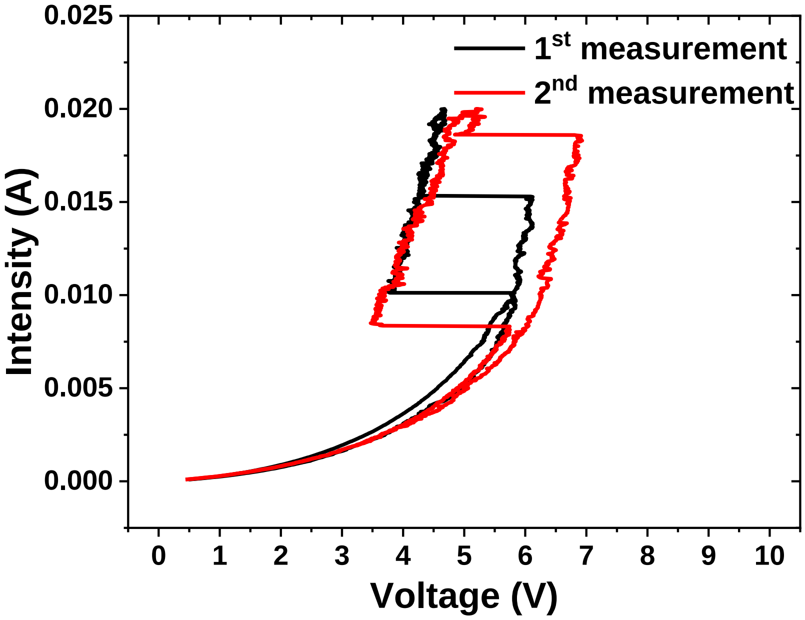

Figure 98. Current-induced switching of an NbO_2-based MIM device with a top electrode side sizes of 60 μm, showing differences between two consecutive measurements.

Figure 99 a) and b) shows the I-V characteristics of an MIM device with electrode size of 30 μm and respectively, the onset of periodic voltage oscillations with a frequency of ~ 23 kHz across the device when excited with a current of 6 mA corresponding to the values in the NDR region of the I-V characteristics. It must be mentioned that these oscillations occur in temporally periodic packages and a continuous oscillation regime could not be achieved. This was probably due to the instability of the I-V characteristic in time associated with the film's unstable NbO_2 phase.

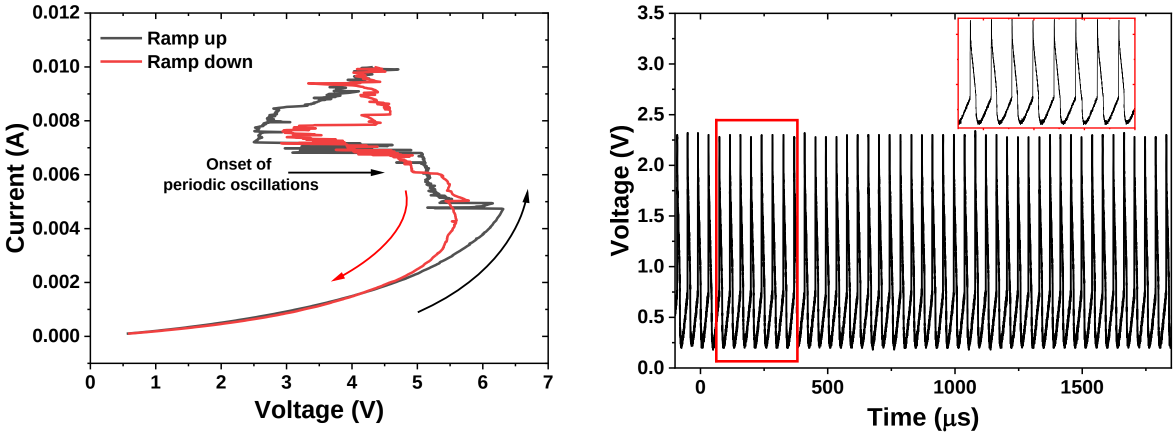

Figure 99. a) I-V characteristic and b) periodic induced voltage oscillations across a NbO_2 – MIM device with an electrode size of 30 μm when excited in the NDR zone with a constant current of 6 mA.

More effort needs to be dedicated to the understanding of the electrical switching mechanism and aging in NbO_2 devices. Some important directions that can be taken are the understanding of the exact chemical composition of the films for every oxygen flow used for their fabrication and evaluating the oscillating behavior of freshly fabricated NbO_2 devices.

IV.3. Temperature-dependent activation of the MIT in NbO_2 films

While electrically induced MIT of an NbO_2 integrated in a MIM device is the most reported activation scheme of the NbO_2 material, it is also necessary to understand the temperature-induced MIT transition in order to fully characterize the material. The difficulty in this case arises from the very high transition temperature resulting in the quick oxidation of the material when heated in air at high temperatures, as observed in the XRD θ-2θ scans shown in Figure 100. In this experiment, a sample deposited at 3.8 sccm O_2 flow, as described in the section discussing the thin film optimization using the Plassys system, was heated up to 800°C and then cooled back to room temperature. It can be seen that the film suffers an irreversible phase transition to a more thermally stable phase i.e. Nb_2O_5. The inset in in Figure 100 is showing the optical image of the sample after the heating XRD measurement.

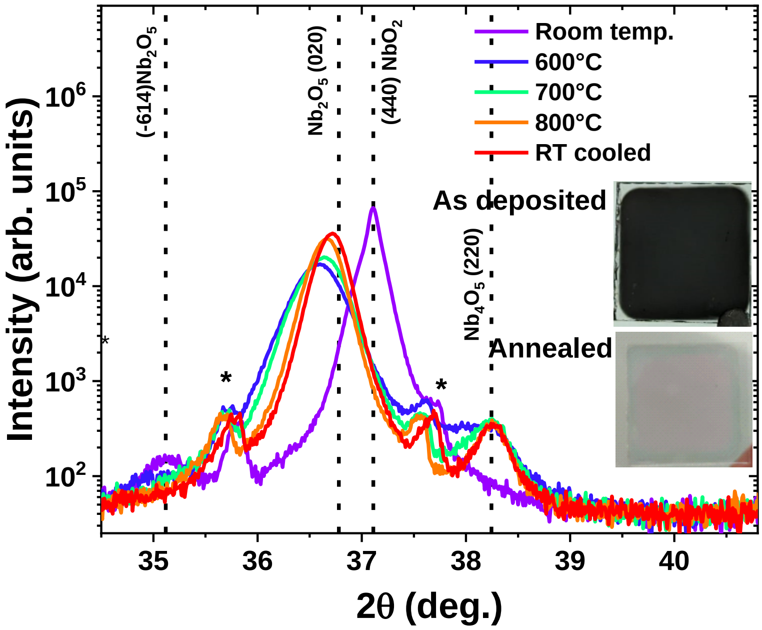

Figure 100. Temperature-dependent XRD scans of a sampled deposited at 3.8 sccm O_2 up to 800°C and after cooling down to room temperature. Inset are the images of the as-deposited sample and after the high-temperature annealing in ambient atmosphere. The asterisks represent diffraction peaks coming from the heating stage.

In order to prevent such high-temperature oxidation, protective measures for the NbO_2 surface must be taken. Some ways to achieve this is by covering the NbO_2 film with a capping layer, or performing the measurements in an inert Ar gas. Temperature-dependent XRD experiments, like the one in Figure 100, on an NbO_2 film covered with an alumina capping layer were performed but this layer did not successfully prevent the oxidation and thus are not shown. This could also be due that the fact that the capping layer was not fabricated in-situ, thus an Nb_2O_5 layer could have formed and acted as a seed for the irreversible phase transition. Further on, the temperature-dependent electrical characterization of NbO_2 layers was performing using two-point probes measurements in a special cell under an inert Ar flow atmosphere (TS 1000E-PB4 17/3 from Linkam covering the temperatures from ambient to 1000°C and allowing in-situ electrical probing).

The temperature-dependent resistance curves of the sample are reproduced on Figure 101, where the lines connecting the experimental recording points are only acting as guides to the eyes. With this sample, also fabricated at an oxygen flow of 3.8 sccm O_2 and 500 and 550°C deposition and annealing temperatures, the expected phenomenon of an MIT can be highlighted. The film behaves as an insulator as the temperature increases up until 800°C, after which the metal-insulator transition is triggered and the NbO_2's resistance increases as the temperature continues to increase, behaving like a metal. Interestingly, the drop-in resistance up to 800°C is about of six order of magnitude, while when returning to room temperature the difference is only five orders of magnitude. While we cannot disregard the fact that the films could have suffered an irreversible phase change due to the insufficient Ar flow, this may have also been the effect of the positioning of the electrical needle probes. The stability of the contact with the film during heating at temperatures as high as 950°C and subsequent cooling may have been affected by the probe positioning.

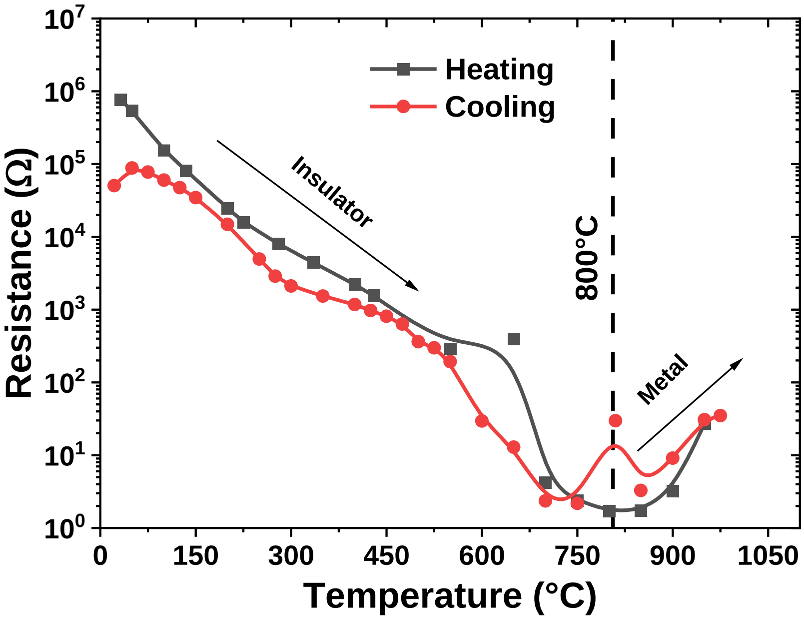

Figure 101. Temperature-dependent two-point resistance measurements of an NbO_2 film up to 950°C and subsequent cooling.

Several research directions can be further explored in the case of temperature activation of the films, such as testing different configurations of capping layers or establishing how the films' phase compositions affect the MIT performances. In a separate, two-probe temperature-dependent experiment of an NbO_2 sample displaying NbO and NbO_2 diffraction peaks (similar to the case presented in Figure 91), the film first increased in resistance up until 300°C, then started to decrease, and at 800°C it presented a sudden drop in the resistance. The ramp-down in temperature showed similar behavior, with the presence of a hysteresis. Thus, it could be interesting to understand how different phase-compositions influence the temperature switching behavior in these compositions.

IV.4. Conclusion

In this chapter the growth and thermal and electrical characterization of NbO_2 films was presented. Using a first deposition system, it was observed that depositions from $Ar+O_2$ gas mixtures flows at 0, 3.8, and 3.5 sccm O_2 exhibited randomly oriented polycrystalline films, while the film deposited from 7 sccm O_2 displayed a mono-oriented structure, as evidenced by the absence of peaks in the GI-XRD scans. However, it should be noted that the latter observation may be attributed to the films also containing amorphous Nb_2O_5 phases, as they exhibited a lighter color (which could also be due to a presumably lower thickness). Subsequent post-annealing of the films deposited at 0 sccm O_2 resulted in a phase transition to NbO_2, while for the other films, it led to an increase in crystallinity, as indicated by XRD investigations.

Using a more recent PVD-6 deposition system, films were fabricated at 2.5 and 3.5 sccm O_2 flows at a substrate temperature of 650°C and annealed at 750°C in full oxygen atmosphere. XRD measurements shown that for these oxygen flows, randomly-oriented polycrystalline films presenting peaks linked to the NbO phase were present before and after the post-annealing step. The post-annealing step however was successful in transforming the film into NbO_2.

Furthermore, we conducted electrical triggering of the MIT using vertical MIM devices consisting of an Al_2O_3/Pt/NbO_2/Au structure. These MIM devices featured square top-electrodes with varying side sizes of 30, 40, 50, 60, and 70 μm. Notably, the growth of NbO_2 on the Pt layer covering the sapphire substrate exhibited different orientations compared to the films grown directly on c-Al_2O_3. Our experiments demonstrated successful electrical and voltage switching capabilities of the NbO_2-based MIM devices having electrode sides dimensions ranging from 30 to 60 μm.

After a 10-month aging period, the electrical performances of the devices were evaluated. It was shown that measurement repeatability was not optimal, but the films nonetheless exhibited a marked MIT, allowing the onset of periodic oscillations with frequencies of ~23 kHz when excited in the NDR region of their I-V characteristics.

Lastly, the thermal-dependent resistance evolution of the film was measured inside a special measurement Linkam cell up to 950°C in a two-probe configuration. It was shown that up to 800°C the films decreased in resistance with temperature, similar to an insulator, while after this point their resistance started to increase, similar to a metal, allowing to identify the metal-insulator transition point.

The research conducted thus far has provided valuable insights into the performances of the fabricated NbO_2 films, but numerous questions remain unanswered. Further characterizations are required to establish a clearer understanding of the relationship between electrical and thermal switching behaviors and the growth parameters involved in NbO_2 films.

Conclusion

The central focus of this work was the fabrication of phase transition materials capable of a volatile solid-solid transition between an insulating and a metallic state, with a further focus on correlating between the structural, electrical and optical properties of the realized films. The fabrication technique employed was reactive DC magnetron sputtering, and the materials of interest included VO_2, tungsten-doped VO_2 ($W:VO_2$), and NbO_2. To this end, significant progress was achieved both in understanding how the fabrication parameters influence the films' properties, and in delimitating new directions of research that can be developed using these MIT-capable materials.

The original work presented in this manuscript can be neatly summarized into three parts, one part for each type of material/ composition that was investigated, i.e. VO_2, $W:VO_2$ and NbO_2:

In the first part of the thesis, an optimization process for sputtering VO_2 films was conducted. This involved depositing films with varying compositions, ranging from V_2O_3 to lower-quality VO_2, and combinations of VO_2 and V_2O_5 phases. Subsequent annealing was employed to enhance the quality and stoichiometry of the films. Through adjustments of the deposition and annealing parameters, high-quality VO_2 films were successfully fabricated, with state-of-the-art electrical performance, exhibiting more than five orders of magnitude change in resistance between insulating and metallic states, and excellent mono oriented, crystalline quality. The control of hysteresis and transition widths, and transition magnitudes was also achieved by adjusting the deposition and annealing parameters. The work performed in this part provides a clear and deep understating into customizing the fabrication process to meet specific application requirements. For example, a sharp transition with a small hysteresis width is useful for electrical/ optical switching applications, while a larger transition width can be achieved for a applications that require a finer modulation of the parameters of interest (THz transmission, resistance). This part also highlights the versatility of reactive magnetron sputtering into easily obtaining various V-O phases from a metallic V target in oxygen atmosphere.

In the second part of the thesis, utilizing the knowledge gained from fabricating the high-quality VO_2 films, the focus was shifted to the fabrication and overall characterization of tungsten-doped VO_2 films and devices. Tungsten doping is employed to lower the energy required to induce the transition in these films and further improve the domains where VO_2- based compositions can be employed. Films with three different doping levels, approximately 0.5%, 1%, and 2 at% W, were achieved, which successfully reduced the transition temperature of the doped VO_2 layers down to room temperature. These doped films have high crystalline quality and high modulation depths (MD) of transmission amplitude in the THz spectrum. The evaluated MD's were from ~96% for the undoped films, to 80% for the highest doped films. The research provided also valuable insights into the nature of the doping by studying the temperature-dependent XRD and Raman scans. Moreover, planar two electrode devices were fabricated to investigate the electrically driven metal-insulator transitions over distances larger than ever seen before (~3 mm interelectrode distance). These large inter-electrode distances are important to study for creating large area THz amplitude modulators, optically activated metacanvases for reconfigurable metamaterials and thermal/ electric switches. Insights into the electrically activated MIT through the formation of a metallic filament was also conducted by using infrared thermal imaging, X-ray diffraction, and Raman spectroscopy.

The third part of this thesis, reports the investigations on the optimization and characterization of NbO_2 thin films. Similar to the methodology applied for VO_2 films, their optimization involved adjusting the deposition and annealing parameters during the fabrication process. Although further research is needed to enhance the crystalline quality of NbO_2 films and gain a deeper understanding of the correlation between deposition parameters and film properties, this study is of significant contribution, particularly in the context of films deposited via reactive magnetron sputtering.

It's worth noting that the research on NbO_2 successfully demonstrated the ability to switch between the insulating and metallic phases using both thermal and electrical methods. Additionally, the influence of device aging on electrical switching and the oscillatory behavior of the films was investigated. This provided some insights into the nature of the switching mechanisms and highlights the possibility of NbO_2 –based metal-insulator–metal (MIM) devices to be used as a relaxation oscillator.

Some directions for the future research based on the work here should focus on improving the optical activation of the undoped and W-doped films, that is, for reconfigurable metasurfaces or for generating ultrafast responses at different interelectrode distances. Regarding NbO_2 films, more research should be dedicated on fabricating epitaxial films, especially on the PVD6 system, gaining a better understanding the electrically induced MIT for new and aged devices, and creating capping layers that are capable to resist high-temperature oxidation.

In summary, the work presented in this thesis provides a clearer understanding of how reactive magnetron sputtering deposition parameters affect film properties and opens up paths for the development of new devices using phase transition materials. These include large area terahertz modulators, electrical switches, relaxation oscillators and optically activated metacanvases. Furthermore, the materials used in this study exhibit improved structural electrical and optical characteristics, marking a promising direction for future research in various fields.

Bibliography

[1] Y. Zhou, S. Ramanathan, Correlated Electron Materials and Field Effect Transistors for Logic: A Review, Critical Reviews in Solid State and Materials Sciences. 38 (2013) 286–317. https://doi.org/10.1080/10408436.2012.719131.

[2] K. Liu, S. Lee, S. Yang, O. Delaire, J. Wu, Recent progresses on physics and applications of vanadium dioxide, Materials Today. 21 (2018) 875–896. https://doi.org/10.1016/j.mattod.2018.03.029.

[3] F.J. Morin, Oxides Which Show a Metal-to-Insulator Transition at the Neel Temperature, Phys. Rev. Lett. 3 (1959) 34–36. https://doi.org/10.1103/PhysRevLett.3.34.

[4] G. Bélanger, J. Destry, G. Perluzzo, P.M. Raccah, Electron Transport in Single Crystals of Niobium Dioxide, Can. J. Phys. 52 (1974) 2272–2280. https://doi.org/10.1139/p74-297.

[5] R. Shi, N. Shen, J. Wang, W. Wang, A. Amini, N. Wang, C. Cheng, Recent advances in fabrication strategies, phase transition modulation, and advanced applications of vanadium dioxide, Applied Physics Reviews. 6 (2019) 011312. https://doi.org/10.1063/1.5087864.

[6] L.E. Noskin, S.H. Ariel, D.G. Schlom, Growth of NbO2 by Molecular-Beam Epitaxy and Characterization of its Metal-Insulator Transition, MRS Advances. 2 (2017) 3031–3036. https://doi.org/10.1557/adv.2017.505.

[7] H.-T. Kim, B.-J. Kim, S. Choi, B.-G. Chae, Y.W. Lee, T. Driscoll, M.M. Qazilbash, D.N. Basov, Electrical oscillations induced by the metal-insulator transition in VO2, Journal of Applied Physics. 107 (2010) 023702. https://doi.org/10.1063/1.3275575.

[8] A. Beaumont, J. Leroy, J.-C. Orlianges, A. Crunteanu, Current-induced electrical self-oscillations across out-of-plane threshold switches based on VO_2 layers integrated in crossbars geometry, Journal of Applied Physics. 115 (2014) 154502. https://doi.org/10.1063/1.4871543.

[9] X. Liu, S. Li, S.K. Nandi, D.K. Venkatachalam, R.G. Elliman, V. Affiliations, Threshold switching and electrical self-oscillation in niobium oxide films, J. Appl. Phys. (2016) 11.

[10] Young-Sang Jeon, Hoe-Sung Yang, Sangwook Nam, A novel EER structure for reducing complexity using negative resistance amplifier, IEEE Microw. Wireless Compon. Lett. 14 (2004) 195–197. https://doi.org/10.1109/LMWC.2004.827845.

[11] G.A. Gibson, S. Musunuru, J. Zhang, K. Vandenberghe, J. Lee, C.-C. Hsieh, W. Jackson, Y. Jeon, D. Henze, Z. Li, R. Stanley Williams, An accurate locally active memristor model for S-type negative differential resistance in NbOx, Applied Physics Letters. 108 (2016) 023505. https://doi.org/10.1063/1.4939913.

[12] A. Crunteanu, J. Givernaud, J. Leroy, D. Mardivirin, C. Champeaux, J.-C. Orlianges, A. Catherinot, P. Blondy, Voltage- and current-activated metal–insulator transition in VO_2 -based electrical switches: a lifetime operation analysis, Science and Technology of Advanced Materials. 11 (2010) 065002. https://doi.org/10.1088/1468-6996/11/6/065002.

[13] C. Koughia, O. Gunes, C. Zhang, S.-J. Wen, R. Wong, Q. Yang, S.O. Kasap, Topology of conductive clusters in sputtered high-quality VO_2 thin films on the brink of percolation threshold during insulator-to-metal and metal-to-insulator transitions, Journal of Vacuum Science & Technology A. 38 (2020) 063401. https://doi.org/10.1116/6.0000443.

[14] S. Kumar, Z. Wang, N. Davila, N. Kumari, K.J. Norris, X. Huang, J.P. Strachan, D. Vine, A.L.D. Kilcoyne, Y. Nishi, R.S. Williams, Physical origins of current and temperature controlled negative differential resistances in NbO2, Nat Commun. 8 (2017) 658. https://doi.org/10.1038/s41467-017-00773-4.

[15] S. Slesazeck, H. Mähne, H. Wylezich, A. Wachowiak, J. Radhakrishnan, A. Ascoli, R. Tetzlaff, T. Mikolajick, Physical model of threshold switching in NbO $_2$ based memristors, RSC Adv. 5 (2015) 102318–102322. https://doi.org/10.1039/C5RA19300A.

[16] S. Nath, Filamentary Threshold Switching In Niobium Oxides, (2021). https://doi.org/10.25911/7SEA-A485.

[17] Y. Ran, Y. Pei, Z. Zhou, H. Wang, Y. Sun, Z. Wang, M. Hao, J. Zhao, J. Chen, X. Yan, A review of Mott insulator in memristors: The materials, characteristics, applications for future computing systems and neuromorphic computing, Nano Res. 16 (2023) 1165–1182. https://doi.org/10.1007/s12274-022-4773-9.

[18] J. Zaanen, G.A. Sawatzky, Systematics in band gaps and optical spectra of 3D transition metal compounds, Journal of Solid State Chemistry. 88 (1990) 8–27. https://doi.org/10.1016/0022-4596(90)90202-9.

[19] N.F. Mott, The Basis of the Electron Theory of Metals, with Special Reference to the Transition Metals, Proc. Phys. Soc. A. 62 (1949) 416–422. https://doi.org/10.1088/0370-1298/62/7/303.

[20] G. Stefanovich, A. Pergament, D. Stefanovich, Electrical switching and Mott transition in VO $_2$, J. Phys.: Condens. Matter. 12 (2000) 8837–8845. https://doi.org/10.1088/0953-8984/12/41/310.

[21] N.F. Mott, Metal-Insulator Transition, Rev. Mod. Phys. 40 (1968) 677–683. https://doi.org/10.1103/RevModPhys.40.677.

[22] T. Pruschke, M. Jarrell, J.K. Freericks, Anomalous Normal-State Properties of High-Tc Superconductors -- Intrinsic Properties of Strongly Correlated Electron Systems?, Advances in Physics. 44 (1995) 187–210. https://doi.org/10.1080/00018739500101526.

[23] G. Kotliar, D. Vollhardt, Strongly Correlated Materials: Insights From Dynamical Mean-Field Theory, Physics Today. 57 (2004) 53–59. https://doi.org/10.1063/1.1712502.

[24] S.B. Roy, Mott Insulators: Physics and applications, IOP Publishing, 2019. https://doi.org/10.1088/2053-2563/ab16c9.

[25] R.E. Peierls, Quantum theory of solids, Clarendon Press ; Oxford University Press, Oxford : New York, 2001.

[26] R.E. Peierls, More surprises in theoretical physics, Princeton University Press, Princeton, N.J, 1991.

[27] S.V. Streltsov, D.I. Khomskii, Orbital physics in transition metal compounds: new trends, (n.d.).

[28] E.-N. Sirjita, A. Boulle, J.-C. Orlianges, R. Mayet, A. Crunteanu, Structural and electrical properties of high-performance vanadium dioxide thin layers obtained by reactive magnetron sputtering, Thin Solid Films. 759 (2022) 139461. https://doi.org/10.1016/j.tsf.2022.139461.

[29] H. Qiu, M. Yang, Y. Dong, H. Xu, B. Hong, Y. Gu, Y. Yang, C. Zou, Z. Luo, C. Gao, The tetragonal-like to rutile structural phase transition in epitaxial VO_2/TiO_2 (001) thick films, New J. Phys. 17 (2015) 113016. https://doi.org/10.1088/1367-2630/17/11/113016.

[30] A. Mennai, A. Bessaudou, F. Cosset, C. Guines, D. Passerieux, P. Blondy, A. Crunteanu, High cut-off frequency RF switches integrating a metal-insulator transition material, in: 2015 IEEE MTT-S International Microwave Symposium, IEEE, Phoenix, AZ, USA, 2015: pp. 1–3. https://doi.org/10.1109/MWSYM.2015.7166910.

[31] V. Jonsson, L. Piazza, M. Månsson, J. Weissenrieder, O. Tjernberg, S. Khartsev, Y. Sassa, D.G. Mazzone, N. Gauthier, M. Muntwiler, C.S. Ong, D. Iuşan, P. Thunström, O. Eriksson, Photoelectron dispersion in metallic and insulating VO 2 thin films, Phys. Rev. Research. 3 (2021) 033286. https://doi.org/10.1103/PhysRevResearch.3.033286.

[32] A. D'Elia, C. Grazioli, A. Cossaro, B.W. Li, C.W. Zou, S.J. Rezvani, N. Pinto, A. Marcelli, M. Coreno, Strain mediated Filling Control nature of the Metal-Insulator Transition of VO2 and electron correlation effects in nanostructured films, Applied Surface Science. 540 (2021) 148341. https://doi.org/10.1016/j.apsusc.2020.148341.

[33] Z. Fang, S. Tian, B. Li, Q. Liu, B. Liu, X. Zhao, G. Sankar, VO2/ZnO bilayer films with enhanced thermochromic property and durability for smart windows, Applied Surface Science. 540 (2021) 148414. https://doi.org/10.1016/j.apsusc.2020.148414.

[34] S. Lee, C. Cheng, H. Guo, K. Hippalgaonkar, K. Wang, J. Suh, K. Liu, J. Wu, Axially Engineered Metal–Insulator Phase Transition by Graded Doping VO_2 Nanowires, J. Am. Chem. Soc. 135 (2013) 4850–4855. https://doi.org/10.1021/ja400658u.

[35] S.V. Mutilin, V.Ya. Prinz, V.A. Seleznev, L.V. Yakovkina, Growth of ordered arrays of vertical free-standing VO_2 nanowires on nanoimprinted Si, Appl. Phys. Lett. 113 (2018) 043101. https://doi.org/10.1063/1.5031075.

[36] J. Zhang, H. Jin, Z. Chen, M. Cao, P. Chen, Y. Dou, Y. Zhao, J. Li, Self-Assembling VO_2 Nanonet with High Switching Performance at Wafer-Scale, Chem. Mater. 27 (2015) 7419–7424. https://doi.org/10.1021/acs.chemmater.5b03314.

[37] X. Xiao, H. Cheng, G. Dong, Y. Yu, L. Chen, L. Miao, G. Xu, A facile process to prepare one dimension VO_2 nanostructures with superior metal–semiconductor transition, CrystEngComm. 15 (2013) 1095–1106. https://doi.org/10.1039/C2CE26262B.

[38] H.-Y. Li, X. Qiu, M. Dong, X. Li, Y. Zhang, B. Xie, Tuned hydrothermal synthesis of vanadium dioxide nanotubes, Ceramics International. 41 (2015) 13967–13973. https://doi.org/10.1016/j.ceramint.2015.07.007.

[39] B. Hu, Y. Zhang, W. Chen, C. Xu, Z.L. Wang, Self-heating and External Strain Coupling Induced Phase Transition of VO2 Nanobeam as Single Domain Switch, Adv. Mater. 23 (2011) 3536–3541. https://doi.org/10.1002/adma.201101731.

[40] C. Weber, D.D. O'Regan, N.D.M. Hine, M.C. Payne, G. Kotliar, P.B. Littlewood, Vanadium Dioxide: A Peierls-Mott Insulator Stable against Disorder, Phys. Rev. Lett. 108 (2012) 256402. https://doi.org/10.1103/PhysRevLett.108.256402.

[41] A.S. Belozerov, M.A. Korotin, V.I. Anisimov, A.I. Poteryaev, Monoclinic M 1 phase of VO 2 : Mott-Hubbard versus band insulator, Phys. Rev. B. 85 (2012) 045109. https://doi.org/10.1103/PhysRevB.85.045109.

[42] J.-Y. Miao, W.-X. Wang, Z.-Y. Jiang, X.-D. Zhang, J.-M. Zheng, A. Du, A theoretical study on pseudo Mott phase transition of vanadium dioxide, Phys. Chem. Chem. Phys. 25 (2023) 759–767. https://doi.org/10.1039/D2CP04763B.

[43] D. Plašienka, R. Martoňák, M.C. Newton, *Ab initio* molecular dynamics study of the structural and electronic transition in VO 2, Phys. Rev. B. 96 (2017) 054111. https://doi.org/10.1103/PhysRevB.96.054111.

[44] Z. Shao, X. Cao, H. Luo, P. Jin, Recent progress in the phase-transition mechanism and modulation of vanadium dioxide materials, NPG Asia Mater. 10 (2018) 581–605. https://doi.org/10.1038/s41427-018-0061-2.

[45] V.R. Morrison, Robert.P. Chatelain, K.L. Tiwari, A. Hendaoui, A. Bruhács, M. Chaker, B.J. Siwick, A photoinduced metal-like phase of monoclinic VO $_2$ revealed by ultrafast electron diffraction, Science. 346 (2014) 445–448. https://doi.org/10.1126/science.1253779.

[46] L. Vidas, D. Schick, E. Martínez, D. Perez-Salinas, A. Ramos-Álvarez, S. Cichy, S. Batlle-Porro, A.S. Johnson, K.A. Hallman, R.F. Haglund, S. Wall, Does Vo 2 Host a Transient Monoclinic Metallic Phase?, Phys. Rev. X. 10 (2020) 031047. https://doi.org/10.1103/PhysRevX.10.031047.

[47] J. Xu, D. Chen, S. Meng, Decoupled ultrafast electronic and structural phase transitions in photoexcited monoclinic VO $_2$, Sci. Adv. 8 (2022) eadd2392. https://doi.org/10.1126/sciadv.add2392.

[48] C. Xu, C. Jin, Z. Chen, Q. Lu, Y. Cheng, B. Zhang, F. Qi, J. Chen, X. Yin, G. Wang, D. Xiang, D. Qian, Transient dynamics of the phase transition in VO2 revealed by mega-electron-volt ultrafast electron diffraction, Nat Commun. 14 (2023) 1265. https://doi.org/10.1038/s41467-023-37000-2.

[49] U. Schwingenschloegl, V. Eyert, The vanadium Magneli phases VnO(2n-1), Annalen Der Physik. 516 (2004) 532–553. https://doi.org/10.1002/andp.200410099.

[50] H. Katzke, P. Tolédano, W. Depmeier, Theory of morphotropic transformations in vanadium oxides, Phys. Rev. B. 68 (2003) 024109. https://doi.org/10.1103/PhysRevB.68.024109.

[51] N. Bahlawane, D. Lenoble, Vanadium Oxide Compounds **:** Structure, Properties, and Growth from the Gas Phase, Chem. Vap. Deposition. 20 (2014) 299–311. https://doi.org/10.1002/cvde.201400057.

[52] M. Li, S. Magdassi, Y. Gao, Y. Long, Hydrothermal Synthesis of VO $_2$ Polymorphs: Advantages, Challenges and Prospects for the Application of Energy Efficient Smart Windows, Small. 13 (2017) 1701147. https://doi.org/10.1002/smll.201701147.

[53] B. Hong, J. Zhao, K. Hu, Y. Yang, Z. Luo, X. Li, C. Gao, Facile synthesis of various epitaxial and textured polymorphs of vanadium oxide thin films on the (0006)-surface of sapphire substrates, RSC Adv. 7 (2017) 22341–22346. https://doi.org/10.1039/C7RA00389G.

[54] P. Shvets, O. Dikaya, K. Maksimova, A. Goikhman, A review of Raman spectroscopy of vanadium oxides, J Raman Spectrosc. 50 (2019) 1226–1244. https://doi.org/10.1002/jrs.5616.

[55] D.B. McWhan, M. Marezio, J.P. Remeika, P.D. Dernier, X-ray diffraction study of metallic V O 2, Phys. Rev. B. 10 (1974) 490–495. https://doi.org/10.1103/PhysRevB.10.490.

[56] K. Okimura, J. Sakai, Changes in Lattice Parameters of VO $_2$ Films Grown on *c* -Plane Al $_2$ O $_3$ Substrates across Metal–Insulator Transition, Jpn. J. Appl. Phys. 48 (2009) 045504. https://doi.org/10.1143/JJAP.48.045504.

[57] S. Westman, I. Lindqvist, B. Sparrman, G.B. Nielsen, H. Nord, A. Jart, Note on a Phase Transition in VO2., Acta Chem. Scand. 15 (1961) 217–217. https://doi.org/10.3891/acta.chem.scand.15-0217.

[58] V. Eyert, The metal-insulator transitions of VO2: A band theoretical approach, Annalen Der Physik. 514 (2002) 650–704. https://doi.org/10.1002/1521-3889(200210)11:9<650::AID-ANDP650>3.0.CO;2-K.

[59] J.D. Budai, A. Tselev, J.Z. Tischler, E. Strelcov, A. Kolmakov, W.J. Liu, A. Gupta, J. Narayan, In situ X-ray microdiffraction studies inside individual VO2 microcrystals, Acta Materialia. 61 (2013) 2751–2762. https://doi.org/10.1016/j.actamat.2012.09.074.

[60] A. Zylbersztejn, N.F. Mott, Metal-insulator transition in vanadium dioxide, Phys. Rev. B. 11 (1975) 4383–4395. https://doi.org/10.1103/PhysRevB.11.4383.

[61] J.H. Park, J.M. Coy, T.S. Kasirga, C. Huang, Z. Fei, S. Hunter, D.H. Cobden, Measurement of a solid-state triple point at the metal–insulator transition in VO2, Nature. 500 (2013) 431–434. https://doi.org/10.1038/nature12425.

[62] J.B. Goodenough, The two components of the crystallographic transition in VO2, Journal of Solid State Chemistry. 3 (1971) 490–500. https://doi.org/10.1016/0022-4596(71)90091-0.

[63] N.B. Aetukuri, A.X. Gray, M. Drouard, M. Cossale, L. Gao, A.H. Reid, R. Kukreja, H. Ohldag, C.A. Jenkins, E. Arenholz, K.P. Roche, H.A. Dürr, M.G. Samant, S.S.P. Parkin, Control of the metal–insulator transition in vanadium dioxide by modifying orbital occupancy, Nature Phys. 9 (2013) 661–666. https://doi.org/10.1038/nphys2733.

[64] R. Lopez, T.E. Haynes, L.A. Boatner, L.C. Feldman, R.F. Haglund, Size effects in the structural phase transition of VO 2 nanoparticles, Phys. Rev. B. 65 (2002) 224113. https://doi.org/10.1103/PhysRevB.65.224113.

[65] V.A. Klimov, I.O. Timofeeva, S.D. Khanin, E.B. Shadrin, A.V. Ilinskii, F. Silva-Andrade, Hysteresis loop construction for the metal-semiconductor phase transition in vanadium dioxide films, Tech. Phys. 47 (2002) 1134–1139. https://doi.org/10.1134/1.1508078.

[66] S. Fan, L. Fan, Q. Li, J. Liu, B. Ye, The identification of defect structures for oxygen pressure dependent VO2 crystal films, Applied Surface Science. 321 (2014) 464–468. https://doi.org/10.1016/j.apsusc.2014.10.057.

[67] J. Narayan, V.M. Bhosle, Phase transition and critical issues in structure-property correlations of vanadium oxide, Journal of Applied Physics. 100 (2006) 103524. https://doi.org/10.1063/1.2384798.

[68] J. Jian, W. Zhang, C. Jacob, A. Chen, H. Wang, J. Huang, H. Wang, Roles of grain boundaries on the semiconductor to metal phase transition of VO2 thin films, Applied Physics Letters. 107 (2015) 102105. https://doi.org/10.1063/1.4930831.

[69] R.A. Aliev, V.N. Andreev, V.M. Kapralova, V.A. Klimov, A.I. Sobolev, E.B. Shadrin, Effect of grain sizes on the metal-semiconductor phase transition in vanadium dioxide polycrystalline thin films, Phys. Solid State. 48 (2006) 929–934. https://doi.org/10.1134/S1063783406050180.

[70] Y. Gao, H. Luo, Z. Zhang, L. Kang, Z. Chen, J. Du, M. Kanehira, C. Cao, Nanoceramic VO2 thermochromic smart glass: A review on progress in solution processing, Nano Energy. 1 (2012) 221–246. https://doi.org/10.1016/j.nanoen.2011.12.002.

[71] J. Houska, Design and reactive magnetron sputtering of thermochromic coatings, Journal of Applied Physics. 131 (2022) 110901. https://doi.org/10.1063/5.0084792.

[72] M. Jiang, X. Xu, F. Hu, H. Du, L. Zhang, Y. Zou, Low-Voltage Triggered VO $_2$ Hybrid Metasurface Used for Amplitude Modulation of Terahertz Orthogonal Modes, J. Lightwave Technol. 40 (2022) 156–162. https://doi.org/10.1109/JLT.2021.3120730.

[73] T.M. Nguyen, D.L. Vu, T.Q.H. Nguyen, J.-M. Kim, Reconfigurable broadband metasurfaces with nearly perfect absorption and high efficiency polarization conversion in THz range, Sci Rep. 12 (2022) 18779. https://doi.org/10.1038/s41598-022-23536-8.

[74] S. Chen, X. Yi, H. Ma, T. Xiong, H. Wang, C. Ke, Phase Transition VO $_2$ Thin Films for Optical Switches, International Journal of Infrared and Millimeter Waves. 25 (2004) 157–163. https://doi.org/10.1023/B:IJIM.0000012771.09884.61.

[75] C. Lu, Q. Lu, M. Gao, Y. Lin, Dynamic Manipulation of THz Waves Enabled by Phase-Transition VO2 Thin Film, Nanomaterials. 11 (2021) 114. https://doi.org/10.3390/nano11010114.

[76] W. Liang, G. Li, Q. Zhou, Z. Zhang, S. Zhang, T. Ning, P. Zhang, Y. Deng, C. Zhang, C. Ge, K. Jin, Resonance dependence of electrically reconfigurable VO $_2$ -based THz metadevice for memory information processing, Appl. Phys. Lett. 122 (2023) 071702. https://doi.org/10.1063/5.0137168.

[77] K. Nemoto, R. Takeuchi, M. Baba, M. Takeda, N. Yamada, Output power leveling of on-chip thermoelectric generator using a solid–solid phase change material, Journal of Energy Storage. 56 (2022) 106119. https://doi.org/10.1016/j.est.2022.106119.

[78] D. Zhang, B. Wu, H. Liu, B. Yang, Y. Sun, X. Wu, Spacecraft smart radiation device with variable emission and low absorption based on phase change material VO2, International Journal of Thermal Sciences. 185 (2023) 108039. https://doi.org/10.1016/j.ijthermalsci.2022.108039.

[79] M.A. Kats, R. Blanchard, S. Zhang, P. Genevet, C. Ko, S. Ramanathan, F. Capasso, Vanadium Dioxide as a Natural Disordered Metamaterial: Perfect Thermal Emission and Large Broadband Negative Differential Thermal Emittance, Phys. Rev. X. 3 (2013) 041004. https://doi.org/10.1103/PhysRevX.3.041004.

[80] K. Liu, C. Cheng, Z. Cheng, K. Wang, R. Ramesh, J. Wu, Giant-Amplitude, High-Work Density Microactuators with Phase Transition Activated Nanolayer Bimorphs, Nano Lett. 12 (2012) 6302–6308. https://doi.org/10.1021/nl303405g.

[81] F. Fatani, M. Vaseem, Z. Akhter, R.M. Bilal, A. Shamim, Remote Monitoring of Skin Temperature Through a Wristband Employing a Printed VO Sensor <sub/>, IEEE Sensors J. 23 (2023) 169–180. https://doi.org/10.1109/JSEN.2022.3223947.

[82] E. Strelcov, Y. Lilach, A. Kolmakov, Gas Sensor Based on Metal−Insulator Transition in VO $_2$ Nanowire Thermistor, Nano Lett. 9 (2009) 2322–2326. https://doi.org/10.1021/nl900676n.

[83] D. Ruzmetov, G. Gopalakrishnan, C. Ko, V. Narayanamurti, S. Ramanathan, Three-terminal field effect devices utilizing thin film vanadium oxide as the channel layer, J. Appl. Phys. (2010) 114516. https://doi.org/10.1063/1.3408899.

[84] Q. Tricas, P. Besnier, X. Castel, C. Le Paven, P. Foutrel, VO $_2$ Thin Film as a Temperature Activated Electromagnetic Shield, in: 2021 IEEE International Joint EMC/SI/PI and EMC Europe Symposium, IEEE, Raleigh, NC, USA, 2021: pp. 38–43. https://doi.org/10.1109/EMC/SI/PI/EMCEurope52599.2021.9559174.

[85] P. Hu, P. Hu, T.D. Vu, M. Li, S. Wang, Y. Ke, X. Zeng, L. Mai, Y. Long, Vanadium Oxide: Phase Diagrams, Structures, Synthesis, and Applications, Chem. Rev. (2023) acs.chemrev.2c00546. https://doi.org/10.1021/acs.chemrev.2c00546.

[86] S. Bhupathi, S. Wang, Y. Ke, Y. Long, Recent progress in vanadium dioxide: The multi-stimuli responsive material and its applications, Materials Science and Engineering: R: Reports. 155 (2023) 100747. https://doi.org/10.1016/j.mser.2023.100747.

[87] K. Kulmus, S. Gemming, M. Schreiber, D. Pashov, S. Acharya, Theoretical evidence for the Peierls transition in NbO 2, Phys. Rev. B. 104 (2021) 035128. https://doi.org/10.1103/PhysRevB.104.035128.

[88] C.N.R. Rao, G.R. Rao, G.V.S. Rao, Semiconductor-Metal Transitions in NbO, and Nb, -,V,O, (n.d.).

[89] K.T. Jacob, C. Shekhar, M. Vinay, Y. Waseda, Thermodynamic Properties of Niobium Oxides, J. Chem. Eng. Data. 55 (2010) 4854–4863. https://doi.org/10.1021/je1004609.

[90] T. Joshi, E. Cirino, S.A. Morley, D. Lederman, Thermally induced metal-to-insulator transition in Nb O 2 thin films: Modulation of the transition temperature by epitaxial strain, Phys. Rev. Materials. 3 (2019) 124602. https://doi.org/10.1103/PhysRevMaterials.3.124602.

[91] A. O'Hara, A.A. Demkov, Nature of the metal-insulator transition in Nb O 2, Phys. Rev. B. 91 (2015) 094305. https://doi.org/10.1103/PhysRevB.91.094305.

[92] G.J. Páez Fajardo, S.A. Howard, E. Evlyukhin, M.J. Wahila, W.R. Mondal, M. Zuba, J.E. Boschker, H. Paik, D.G. Schlom, J.T. Sadowski, S.A. Tenney, B. Reinhart, W.-C. Lee, L.F.J. Piper, Structural Phase Transitions of NbO_2: Bulk versus Surface, Chem. Mater. 33 (2021) 1416–1425. https://doi.org/10.1021/acs.chemmater.0c04566.

[93] M.J. Wahila, G. Paez, C.N. Singh, A. Regoutz, S. Sallis, M.J. Zuba, J. Rana, M.B. Tellekamp, J.E. Boschker, T. Markurt, J.E.N. Swallow, L.A.H. Jones, T.D. Veal, W. Yang, T.-L. Lee, F. Rodolakis, J.T. Sadowski, D. Prendergast, W.-C. Lee, W.A. Doolittle, L.F.J. Piper, Evidence of a second-order Peierls-driven metal-insulator transition in crystalline NbO 2, Phys. Rev. Materials. 3 (2019) 074602. https://doi.org/10.1103/PhysRevMaterials.3.074602.

[94] M.R. Beebe, J.M. Klopf, Y. Wang, S. Kittiwatanakul, J. Lu, S.A. Wolf, R.A. Lukaszew, Time-resolved light-induced insulator-metal transition in niobium dioxide and vanadium dioxide thin films, Opt. Mater. Express. 7 (2017) 213. https://doi.org/10.1364/OME.7.000213.

[95] R. Rana, J.M. Klopf, J. Grenzer, H. Schneider, M. Helm, A. Pashkin, Nonthermal nature of photoinduced insulator-to-metal transition in NbO 2, Phys. Rev. B. 99 (2019) 041102. https://doi.org/10.1103/PhysRevB.99.041102.

[96] T. Joshi, P. Borisov, D. Lederman, Structural and electrical characterization of polycrystalline NbO_2 thin film vertical devices grown on TiN-coated SiO_2/Si substrates, Journal of Applied Physics. 124 (2018) 114502. https://doi.org/10.1063/1.5038837.

[97] T. Hadamek, A.B. Posadas, A. Dhamdhere, D.J. Smith, A.A. Demkov, Spectral identification scheme for epitaxially grown single-phase niobium dioxide, Journal of Applied Physics. 119 (2016) 095308. https://doi.org/10.1063/1.4942834.

[98] J.C. Lee, W.W. Durand, Electrically stimulated optical switching of NbO_2 thin films, Journal of Applied Physics. 56 (1984) 3350–3352. https://doi.org/10.1063/1.333863.

[99] F.J. Wong, N. Hong, S. Ramanathan, Orbital splitting and optical conductivity of the insulating state of NbO 2, Phys. Rev. B. 90 (2014) 115135. https://doi.org/10.1103/PhysRevB.90.115135.

[100] J.H. Lee, E.J. Cha, Y.T. Kim, B.K. Chae, J.J. Kim, S.Y. Lee, H.S. Hwang, C.G. Park, A study of threshold switching of NbO2 using atom probe tomography and transmission electron microscopy, Micron. 79 (2015) 101–109. https://doi.org/10.1016/j.micron.2015.07.015.

[101] D. Music, P. Schmidt, S. Mráz, Adsorption of film-forming species on NbO and NbO_2 surfaces, Journal of Vacuum Science & Technology A: Vacuum, Surfaces, and Films. 35 (2017) 061512. https://doi.org/10.1116/1.4995492.

[102] D. Music, A.M. Krause, P.A.T. Olsson, Theoretical and Experimental Aspects of Current and Future Research on NbO2 Thin Film Devices, (2021) 13.

[103] C. Nico, T. Monteiro, M.P.F. Graça, Niobium oxides and niobates physical properties: Review and prospects, Progress in Materials Science. 80 (2016) 1–37. https://doi.org/10.1016/j.pmatsci.2016.02.001.

[104] R.A. Rani, A.S. Zoolfakar, A.P. O'Mullane, M.W. Austin, K. Kalantar-Zadeh, Thin films and nanostructures of niobium pentoxide: fundamental properties, synthesis methods and applications, J. Mater. Chem. A. 2 (2014) 15683–15703. https://doi.org/10.1039/C4TA02561J.

[105] H.-D. Kim, M.J. Yun, T.G. Kim, Self-selection bipolar resistive switching phenomena observed in NbON/NbN bilayer for cross-bar array memory applications, Appl. Phys. Lett. 105 (2014) 213510. https://doi.org/10.1063/1.4902969.

[106] R.P. Elliot, COLUMBIUM-OXYGEN SYSTEM, Trans. Am. Soc. Metals. (1960).

[107] Adrian.A. Bolzan, C. Fong, Brendan.J. Kennedy, C.J. Howard, A Powder Neutron Diffraction Study of Semiconducting and Metallic Niobium Dioxide, (1994).

[108] D. Mélissa, X-ray investigation of Nb/O interfaces, (n.d.).

[109] V. Eyert, The metal-insulator transition of NbO_2: An embedded Peierls instability, Europhys. Lett. 58 (2002) 851–856. https://doi.org/10.1209/epl/i2002-00452-6.

[110] W.H. Brito, M.C.O. Aguiar, K. Haule, G. Kotliar, Dynamic electronic correlation effects in NbO 2 as compared to VO 2, Phys. Rev. B. 96 (2017) 195102. https://doi.org/10.1103/PhysRevB.96.195102.

[111] A. Fakih, Current Controlled Negative Differential Resistance in Niobium Dioxide, Unpublished, 2019. http://rgdoi.net/10.13140/RG.2.2.14609.17765 (accessed April 4, 2023).

[112] Y. Zhao, Z. Zhang, Y. Lin, Optical and dielectric properties of a nanostructured NbO_2 thin film prepared by thermal oxidation, J. Phys. D: Appl. Phys. 37 (2004) 3392–3395. https://doi.org/10.1088/0022-3727/37/24/006.

[113] D. Music, Y.-T. Chen, P. Bliem, R.W. Geyer, Amorphous-crystalline transition in thermoelectric NbO_2, J. Phys. D: Appl. Phys. 48 (2015) 275301. https://doi.org/10.1088/0022-3727/48/27/275301.

[114] M. Backhaus-Ricoult, J. Rustad, L. Moore, C. Smith, J. Brown, Semiconducting large bandgap oxides as potential thermoelectric materials for high-temperature power

generation?, Appl. Phys. A. 116 (2014) 433–470. https://doi.org/10.1007/s00339-014-8515-z.

[115] D. Music, P. Schmidt, A. Saksena, Experimental and theoretical exploration of mechanical stability of Pt/NbO $_2$ interfaces for thermoelectric applications, J. Phys. D: Appl. Phys. 50 (2017) 455502. https://doi.org/10.1088/1361-6463/aa8daf.

[116] P. Zhang, S. Li, Y. Bo, X. Liu, Collective dynamics of capacitively coupled oscillators based on NbO $_2$ memristors, Journal of Applied Physics. 126 (2019) 125112. https://doi.org/10.1063/1.5116777.

[117] D.S. Jeon, T.D. Dongale, T.G. Kim, Low power Ti-doped NbO2-based selector device with high selectivity and low OFF current, Journal of Alloys and Compounds. 884 (2021) 161041. https://doi.org/10.1016/j.jallcom.2021.161041.

[118] P. Chen, X. Zhang, Q. Liu, M. Liu, NbO2-based locally active memristors: from physical mechanisms to performance optimization, Appl. Phys. A. 128 (2022) 1113. https://doi.org/10.1007/s00339-022-06258-6.

[119] P. Wang, A.I. Khan, S. Yu, Cryogenic behavior of NbO $_2$ based threshold switching devices as oscillation neurons, Appl. Phys. Lett. 116 (2020) 162108. https://doi.org/10.1063/5.0006467.

[120] J. Sun, W. Sun, L. Du, C. Du, Y. Gao, G. Yin, Tailored NbO $_2$ Modified Pt/Graphene as Highly Stable Electrocatalyst Towards Oxygen Reduction Reaction, Fuel Cells. 18 (2018) 360–368. https://doi.org/10.1002/fuce.201700191.

[121] Y. Wang, R.B. Comes, S.A. Wolf, J. Lu, Threshold Switching Characteristics of Nb/NbO $_2$ /TiN Vertical Devices, IEEE J. Electron Devices Soc. 4 (2016) 11–14. https://doi.org/10.1109/JEDS.2015.2503922.

[122] J.M. Ang, P.A. Dananjaya, S.C.W. Chow, G.J. Lim, C.S. Seet, W.S. Lew, Enhancement of temperature-modulated NbO $_2$ -based relaxation oscillator via interfacial and bulk treatments, Nanotechnology. 34 (2023) 185202. https://doi.org/10.1088/1361-6528/acb778.

[123] A. Chen, Z. Zhang, G. Ma, N. Liu, C.-Y. Lin, W.-C. Chen, T.-C. Chang, H. Wang, Comprehensive Regulation of the Threshold Oscillation for Neuromorphic Systems Based on Cryogenic Performance of NbO_2 Device, IEEE Electron Device Lett. 42 (2021) 692–695. https://doi.org/10.1109/LED.2021.3068823.

[124] D. Koch, M. Chaker, The Origin of the Thermochromic Property Changes in Doped Vanadium Dioxide, ACS Appl. Mater. Interfaces. 14 (2022) 23928–23943. https://doi.org/10.1021/acsami.2c02070.

[125] Y. Xue, S. Yin, Element doping: a marvelous strategy for pioneering the smart applications of VO2, (2022) 45.

[126] Y. Wu, L. Fan, S. Chen, S. Chen, F. Chen, C. Zou, Z. Wu, A novel route to realize controllable phases in an aluminum (Al3+)-doped VO2 system and the metal–insulator transition modulation, Materials Letters. 127 (2014) 44–47. https://doi.org/10.1016/j.matlet.2014.04.094.

[127] J.-L. Victor, M. Gaudon, G. Salvatori, O. Toulemonde, N. Penin, A. Rougier, Doubling of the Phase Transition Temperature of VO $_2$ by Fe Doping, J. Phys. Chem. Lett. 12 (2021) 7792–7796. https://doi.org/10.1021/acs.jpclett.1c02179.

[128] A. Krammer, O. Bouvard, A. Schüler, Study of Si doped VO 2 thin films for solar thermal applications, Energy Procedia. 122 (2017) 745–750. https://doi.org/10.1016/j.egypro.2017.07.390.

[129] X. Tan, W. Liu, R. Long, X. Zhang, T. Yao, Q. Liu, Z. Sun, Y. Cao, S. Wei, Symmetry-Controlled Structural Phase Transition Temperature in Chromium-Doped Vanadium Dioxide, J. Phys. Chem. C. 120 (2016) 28163–28168. https://doi.org/10.1021/acs.jpcc.6b08586.

[130] Z. Liang, L. Zhao, W. Meng, C. Zhong, S. Wei, B. Dong, Z. Xu, L. Wan, S. Wang, Tungsten-doped vanadium dioxide thin films as smart windows with self-cleaning and energy-saving functions, Journal of Alloys and Compounds. 694 (2017) 124–131. https://doi.org/10.1016/j.jallcom.2016.09.315.

[131] T.J. Hanlon, J.A. Coath, M.A. Richardson, Molybdenum-doped vanadium dioxide coatings on glass produced by the aqueous sol–gel method, Thin Solid Films. 436 (2003) 269–272. https://doi.org/10.1016/S0040-6090(03)00602-3.

[132] S. Guan, M. Souquet-Basiège, O. Toulemonde, D. Denux, N. Penin, M. Gaudon, A. Rougier, Toward Room-Temperature Thermochromism of VO_2 by Nb Doping: Magnetic Investigations, Chem. Mater. 31 (2019) 9819–9830. https://doi.org/10.1021/acs.chemmater.9b03906.

[133] Q. Gu, A. Falk, J. Wu, L. Ouyang, H. Park, Current-Driven Phase Oscillation and Domain-Wall Propagation in $W_x V_{1-x} O_2$ Nanobeams, Nano Lett. 7 (2007) 363–366. https://doi.org/10.1021/nl0624768.

[134] S. Chen, L. Dai, J. Liu, Y. Gao, X. Liu, Z. Chen, J. Zhou, C. Cao, P. Han, H. Luo, M. Kanahira, The visible transmittance and solar modulation ability of VO2 flexible foils simultaneously improved by Ti doping: an optimization and first principle study, Phys. Chem. Chem. Phys. 15 (2013) 17537. https://doi.org/10.1039/c3cp52009a.

[135] T. Huang, T. Kang, Y. Li, J. Li, L. Deng, L. Bi, Metal-insulator phase transition in Hf-doped VO_2 (M) thin films: a study on the structural, electrical, optical and infrared radiation properties, Opt. Mater. Express. 8 (2018) 2300. https://doi.org/10.1364/OME.8.002300.

[136] N.R. Mlyuka, G.A. Niklasson, C.G. Granqvist, Mg doping of thermochromic VO2 films enhances the optical transmittance and decreases the metal-insulator transition temperature, Appl. Phys. Lett. 95 (2009) 171909. https://doi.org/10.1063/1.3229949.

[137] Y. Gao, C. Cao, L. Dai, H. Luo, M. Kanehira, Y. Ding, Z.L. Wang, Phase and shape controlled VO2 nanostructures by antimony doping, Energy Environ. Sci. 5 (2012) 8708. https://doi.org/10.1039/c2ee22290f.

[138] D.S. Jeon, T.D. Dongale, T.G. Kim, Low power Ti-doped NbO2-based selector device with high selectivity and low OFF current, Journal of Alloys and Compounds. 884 (2021) 161041. https://doi.org/10.1016/j.jallcom.2021.161041.

[139] W. Sun, J. Sun, L. Du, C. Du, Y. Gao, G. Yin, Synthesis of Nitrogen-doped Niobium Dioxide and its co-catalytic effect towards the electrocatalysis of oxygen reduction on platinum, Electrochimica Acta. 195 (2016) 166–174. https://doi.org/10.1016/j.electacta.2016.02.122.

[140] R.M. Pallares, X. Su, S.H. Lim, N.T.K. Thanh, Optimization of metal-to-insulator phase transition properties in polycrystalline VO2 films for terahertz modulation applications by doping, J. Mater. Chem. C. 4 (2016) 53–61. https://doi.org/10.1039/C5TC02426A.

[141] S.S. Maklakov, V.I. Polozov, S.A. Maklakov, A.D. Mishin, I.A. Ryzhikov, A.L. Trigub, V.A. Amelichev, K.I. Maslakov, V.N. Kisel, Post-deposition annealing of thin RF magnetron sputter-deposited VO2 films above the melting point, Journal of Alloys and Compounds. 763 (2018) 558–569. https://doi.org/10.1016/j.jallcom.2018.06.014.

[142] E.-N. Sirjita, A. Boulle, J.-C. Orlianges, R. Mayet, A. Crunteanu, Structural and electrical properties of high-performance vanadium dioxide thin layers obtained by reactive magnetron sputtering, Thin Solid Films. (2022) 8.

[143] V. Théry, A. Boulle, A. Crunteanu, J.C. Orlianges, A. Beaumont, R. Mayet, A. Mennai, F. Cosset, A. Bessaudou, M. Fabert, Structural and electrical properties of large area epitaxial VO $_2$ films grown by electron beam evaporation, Journal of Applied Physics. 121 (2017) 055303. https://doi.org/10.1063/1.4975117.

[144] N.F. Quackenbush, H. Paik, M.J. Wahila, S. Sallis, M.E. Holtz, X. Huang, A. Ganose, B.J. Morgan, D.O. Scanlon, Y. Gu, F. Xue, L.-Q. Chen, G.E. Sterbinsky, C. Schlueter, T.-L. Lee, J.C. Woicik, J.-H. Guo, J.D. Brock, D.A. Muller, D.A. Arena, D.G. Schlom, L.F.J. Piper, Stability of the M2 phase of vanadium dioxide induced by coherent epitaxial strain, Phys. Rev. B. 94 (2016) 085105. https://doi.org/10.1103/PhysRevB.94.085105.

[145] Y. Matamura, M. Kimura, T. Ikenoue, M. Miyake, T. Hirato, Formation of Uniquely Oriented VO $_2$ Thin Films by Topotactic Oxidation of V $_2$ O $_3$ Epitaxial Films on R-Plane Al $_2$ O $_3$, Crystal Growth & Design. 22 (2022) 3190–3197. https://doi.org/10.1021/acs.cgd.2c00042.

[146] Z. Shao, L. Wang, T. Chang, F. Xu, G. Sun, P. Jin, X. Cao, Controllable phase-transition temperature upon strain release in VO $_2$ /MgF $_2$ epitaxial films, Journal of Applied Physics. 128 (2020) 045303. https://doi.org/10.1063/5.0011423.

[147] G.J. Kovács, D. Bürger, I. Skorupa, H. Reuther, R. Heller, H. Schmidt, Effect of the substrate on the insulator–metal transition of vanadium dioxide films, Journal of Applied Physics. 109 (2011) 063708. https://doi.org/10.1063/1.3563588.

[148] F.J. Wong, Y. Zhou, S. Ramanathan, Epitaxial variants of VO2 thin films on complex oxide single crystal substrates with 3m surface symmetry, Journal of Crystal Growth. 364 (2013) 74–80. https://doi.org/10.1016/j.jcrysgro.2012.11.054.

[149] R. Molaei, R. Bayati, F. Wu, J. Narayan, A microstructural approach toward the effect of thickness on semiconductor-to-metal transition characteristics of VO $_2$ epilayers, Journal of Applied Physics. 115 (2014) 164311. https://doi.org/10.1063/1.4872030.

[150] V. Théry, Étude de la microstructure et des transitions de phases électroniques et cristallines de couches épitaxiales de VO2 déposées sur différents substrats., UNIVERSITÉ DE LIMOGES, 2017.

[151] K. Okimura, Y. Suzuki, Epitaxial Growth of V $_2$ O $_3$ Thin Films on *c* -Plane Al $_2$ O $_3$ in Reactive Sputtering and Its Transformation to VO $_2$ Films by Post Annealing, Jpn. J. Appl. Phys. 50 (2011) 065803. https://doi.org/10.1143/JJAP.50.065803.

[152] Y.D. Ji, T.S. Pan, Z. Bi, W.Z. Liang, Y. Zhang, H.Z. Zeng, Q.Y. Wen, H.W. Zhang, C.L. Chen, Q.X. Jia, Y. Lin, Epitaxial growth and metal-insulator transition of vanadium oxide thin films with controllable phases, Appl. Phys. Lett. 101 (2012) 071902. https://doi.org/10.1063/1.4745843.

[153] Y. Wang, R.B. Comes, S. Kittiwatanakul, S.A. Wolf, J. Lu, Epitaxial niobium dioxide thin films by reactive-biased target ion beam deposition, Journal of Vacuum Science &

Technology A: Vacuum, Surfaces, and Films. 33 (2015) 021516. https://doi.org/10.1116/1.4906143.

[154] K. Shibuya, A. Sawa, Epitaxial growth and polarized Raman scattering of niobium dioxide films, AIP Advances. 12 (2022) 055103. https://doi.org/10.1063/5.0087610.

[155] Y. Wang, Metal-Insulator Transition in Niobium Dioxide Thin Films, University of Virginia, 2017. https://doi.org/10.18130/V3TS7B.

[156] A.A. Demkov, J.G. Ekerdt, Growth of Niobium Oxide thin films by Molecular Beam Epitaxy, (n.d.).

[157] J.T. Gudmundsson, Physics and technology of magnetron sputtering discharges, Plasma Sources Sci. Technol. 29 (2020) 113001. https://doi.org/10.1088/1361-6595/abb7bd.

[158] D. Maurya, A. Sardarinejad, K. Alameh, Recent Developments in R.F. Magnetron Sputtered Thin Films for pH Sensing Applications—An Overview, Coatings. 4 (2014) 756–771. https://doi.org/10.3390/coatings4040756.

[159] K. Strijckmans, R. Schelfhout, D. Depla, Tutorial: Hysteresis during the reactive magnetron sputtering process, Journal of Applied Physics. 124 (2018) 241101. https://doi.org/10.1063/1.5042084.

[160] P.P. Ewald, Zur Begründung der Kristalloptik, Ann. Phys. 359 (1917) 519–556. https://doi.org/10.1002/andp.19173592305.

[161] F. Conchon, Défauts et déformations au sein de couches d’oxydes épitaxiées : étude par diffraction des rayons X en haute-résolution, n.d.

[162] A. Boulle, *DxTools* : processing large data files recorded with the Bruker D8 diffractometer, J Appl Crystallogr. 50 (2017) 967–974. https://doi.org/10.1107/S1600576717005192.

[163] V. Théry, A. Boulle, A. Crunteanu, J.C. Orlianges, A. Beaumont, R. Mayet, A. Mennai, F. Cosset, A. Bessaudou, M. Fabert, Role of thermal strain in the metal-insulator and structural phase transition of epitaxial VO 2 films, Phys. Rev. B. 93 (2016) 184106. https://doi.org/10.1103/PhysRevB.93.184106.

[164] M. Pan, J. Liu, H. Zhong, S. Wang, Z. Li, X. Chen, W. Lu, Raman study of the phase transition in VO2 thin films, Journal of Crystal Growth. 268 (2004) 178–183. https://doi.org/10.1016/j.jcrysgro.2004.05.005.

[165] F. Ureña-Begara, A. Crunteanu, J.-P. Raskin, Raman and XPS characterization of vanadium oxide thin films with temperature, Applied Surface Science. 403 (2017) 717–727. https://doi.org/10.1016/j.apsusc.2017.01.160.

[166] A. Boulle, R. Guinebretière, A. Dauger, Phenomenological analysis of heterogeneous strain fields in epitaxial thin films using x-ray scattering, J. Phys. D: Appl. Phys. 38 (2005) 3907–3920. https://doi.org/10.1088/0022-3727/38/21/012.

[167] E. Erdoğan, M. Kundakçı, Influence of substrate and substrate temperature on the structural, optical and surface properties of InGaN thin films prepared by RFMS method, Microelectronic Engineering. 207 (2019) 15–18. https://doi.org/10.1016/j.mee.2018.12.010.

[168] V. Théry, A. Boulle, A. Crunteanu, J.C. Orlianges, Combined strain and composition-induced effects in the metal-insulator transition of epitaxial VO $_2$ films, Appl. Phys. Lett. 111 (2017) 251902. https://doi.org/10.1063/1.5010147.

[169] T. Petrișor, A. Meledin, A. Boulle, R.B. Moș, M.S. Gabor, L. Ciontea, T. Petrișor, Ordered misfit dislocations in epitaxial Gd doped CeO 2 thin films deposited on (001)YSZ single crystal substrates, Applied Surface Science. 433 (2018) 668–673. https://doi.org/10.1016/j.apsusc.2017.09.202.

[170] V.M. Kaganer, K.K. Sabelfeld, X-ray diffraction peaks from partially ordered misfit dislocations, Phys. Rev. B. 80 (2009) 184105. https://doi.org/10.1103/PhysRevB.80.184105.

[171] A.V. Ivanov, A.Yu. Tatarenko, A.A. Gorodetsky, O.N. Makarevich, M. Navarro-Cía, A.M. Makarevich, A.R. Kaul, A.A. Eliseev, O.V. Boytsova, Fabrication of Epitaxial W-Doped VO_2 Nanostructured Films for Terahertz Modulation Using the Solvothermal Process, ACS Appl. Nano Mater. 4 (2021) 10592–10600. https://doi.org/10.1021/acsanm.1c02081.

[172] G. Karaoglan-Bebek, M.N.F. Hoque, M. Holtz, Z. Fan, A.A. Bernussi, Continuous tuning of W-doped VO_2 optical properties for terahertz analog applications, Appl. Phys. Lett. 105 (2014) 201902. https://doi.org/10.1063/1.4902056.

[173] R.M. Pallares, X. Su, S.H. Lim, N.T.K. Thanh, Optimization of metal-to-insulator phase transition properties in polycrystalline VO2 films for terahertz modulation applications by doping, J. Mater. Chem. C. 4 (2016) 53–61. https://doi.org/10.1039/C5TC02426A.

[174] Y. Zhao, C. Chen, X. Pan, Y. Zhu, M. Holtz, A. Bernussi, Z. Fan, Tuning the properties of VO_2 thin films through growth temperature for infrared and terahertz modulation applications, Journal of Applied Physics. 114 (2013) 113509. https://doi.org/10.1063/1.4821846.

[175] G. Zhou, P. Dai, J. Wu, B. Jin, Q. Wen, G. Zhu, Z. Shen, C. Zhang, L. Kang, W. Xu, J. Chen, P. Wu, Broadband and high modulation-depth THz modulator using low bias controlled VO_2-integrated metasurface, Opt. Express. 25 (2017) 17322. https://doi.org/10.1364/OE.25.017322.

[176] C. Han, E.P.J. Parrott, G. Humbert, A. Crunteanu, E. Pickwell-MacPherson, Broadband modulation of terahertz waves through electrically driven hybrid bowtie antenna-VO2 devices, Sci Rep. 7 (2017) 12725. https://doi.org/10.1038/s41598-017-13085-w.

[177] Y. Zhao, J. Hwan Lee, Y. Zhu, M. Nazari, C. Chen, H. Wang, A. Bernussi, M. Holtz, Z. Fan, Structural, electrical, and terahertz transmission properties of VO_2 thin films grown on c-, r-, and m-plane sapphire substrates, Journal of Applied Physics. 111 (2012) 053533. https://doi.org/10.1063/1.3692391.

[178] M. Mayer, SIMNRA, a simulation program for the analysis of NRA, RBS and ERDA, in: AIP Conference Proceedings, AIP, Denton, Texas (USA), 1999: pp. 541–544. https://doi.org/10.1063/1.59188.

[179] X. Tan, T. Yao, R. Long, Z. Sun, Y. Feng, H. Cheng, X. Yuan, W. Zhang, Q. Liu, C. Wu, Y. Xie, S. Wei, Unraveling Metal-insulator Transition Mechanism of VO2 Triggered by Tungsten Doping, SCIENTIFIC REPORTS. (n.d.) 6.

[180] C.E. Wilson, A.E. Gibson, P.M. Cuillier, C.-H. Li, P.H.N. Crosby, E.B. Trigg, S. Najmr, C.B. Murray, J.R. Jinschek, V. Doan-Nguyen, Local structure elucidation of tungsten-substituted vanadium dioxide (V$$_{1-x}$$W$$_x$$O$$_2$$), Sci Rep. 12 (2022) 14767. https://doi.org/10.1038/s41598-022-18575-0.

[181] T. Sun, Classical Size Effect In Copper Thin Films: Impact Of Surface And Grain Boundary Scattering On Resistivity, (n.d.).

[182] I. Bakonyi, V.A. Isnaini, T. Kolonits, Zs. Czigány, J. Gubicza, L.K. Varga, E. Tóth-Kádár, L. Pogány, L. Péter, H. Ebert, The specific grain-boundary electrical resistivity of Ni, Philosophical Magazine. 99 (2019) 1139–1162. https://doi.org/10.1080/14786435.2019.1580399.

[183] M. Azmat, J. Haibo, K. Naseem, C. Ling, J. Li, A comparative study uncovering the different effect of Nb, Mo and W dopants on phase transition of vanadium dioxide, Journal of Physics and Chemistry of Solids. 180 (2023) 111439. https://doi.org/10.1016/j.jpcs.2023.111439.

[184] X. Tan, T. Yao, R. Long, Z. Sun, Y. Feng, H. Cheng, X. Yuan, W. Zhang, Q. Liu, C. Wu, Y. Xie, S. Wei, Unraveling Metal-insulator Transition Mechanism of VO2Triggered by Tungsten Doping, Sci Rep. 2 (2012) 466. https://doi.org/10.1038/srep00466.

[185] Y. Wu, L. Fan, W. Huang, S. Chen, S. Chen, F. Chen, C. Zou, Z. Wu, Depressed transition temperature of $W_x V_{1-x} O_2$: mechanistic insights from the X-ray absorption fine structure (XAFS) spectroscopy, Phys. Chem. Chem. Phys. 16 (2014) 17705. https://doi.org/10.1039/C4CP01661K.

[186] P. Schilbe, Raman scattering in VO2, Physica B: Condensed Matter. 316–317 (2002) 600–602. https://doi.org/10.1016/S0921-4526(02)00584-7.

[187] K. Okimura, N. Hanis Azhan, T. Hajiri, S. Kimura, M. Zaghrioui, J. Sakai, Temperature-dependent Raman and ultraviolet photoelectron spectroscopy studies on phase transition behavior of VO_2 films with M1 and M2 phases, Journal of Applied Physics. 115 (2014) 153501. https://doi.org/10.1063/1.4870868.

[188] B. Rajeswaran, A.M. Umarji, Effect of W addition on the electrical switching of VO_2 thin films, AIP Advances. 6 (2016) 035215. https://doi.org/10.1063/1.4944855.

[189] Y. Bleu, F. Bourquard, V. Barnier, A.-S. Loir, F. Garrelie, C. Donnet, Towards Room Temperature Phase Transition of W-Doped VO2 Thin Films Deposited by Pulsed Laser Deposition: Thermochromic, Surface, and Structural Analysis, Materials. 16 (2023) 461. https://doi.org/10.3390/ma16010461.

[190] K. Mulchandani, A. Soni, K. Pathy, K.R. Mavani, Structural transformation and tuning of electronic transitions by W-doping in VO2 thin films, Superlattices and Microstructures. 154 (2021) 106883. https://doi.org/10.1016/j.spmi.2021.106883.

[191] W. Xu, Z. Wu, Z. Xiang, J. Gou, X. Dong, J. Wang, Y. Jiang, Vanadium oxide thin films with extremely narrow thermal hysteresis loop width were obtained by Ta doping for THz modulation applications, Optical Materials. 117 (2021) 111142. https://doi.org/10.1016/j.optmat.2021.111142.

[192] M. Pattanayak, M.N.F. Hoque, Y.-C. Ho, W. Li, Z. Fan, A.A. Bernussi, Ultrahigh tunability of resistive switching in strongly correlated functional oxide, Applied Materials Today. 30 (2023) 101642. https://doi.org/10.1016/j.apmt.2022.101642.

[193] S. Carapezzi, C. Delacour, A. Plews, A. Nejim, S. Karg, A. Todri-Sanial, Role of ambient temperature in modulation of behavior of vanadium dioxide volatile memristors and oscillators for neuromorphic applications, Sci Rep. 12 (2022) 19377. https://doi.org/10.1038/s41598-022-23629-4.

[194] D. Li, A.A. Sharma, N. Shukla, H. Paik, J.M. Goodwill, S. Datta, D.G. Schlom, J.A. Bain, M. Skowronski, ON-state evolution in lateral and vertical VO_2 threshold switching devices, Nanotechnology. 28 (2017) 405201. https://doi.org/10.1088/1361-6528/aa882f.

[195] H. Madan, M. Jerry, A. Pogrebnyakov, T. Mayer, S. Datta, Quantitative Mapping of Phase Coexistence in Mott-Peierls Insulator during Electronic and Thermally Driven Phase Transition, ACS Nano. 9 (2015) 2009–2017. https://doi.org/10.1021/nn507048d.

[196] S. Kumar, M.D. Pickett, J.P. Strachan, G. Gibson, Y. Nishi, R.S. Williams, Local Temperature Redistribution and Structural Transition During Joule-Heating-Driven Conductance Switching in VO_2, Adv. Mater. 25 (2013) 6128–6132. https://doi.org/10.1002/adma.201302046.

[197] Y. Zhao, Y. Zhang, Q. Shi, S. Liang, W. Huang, W. Kou, Z. Yang, Dynamic Photoinduced Controlling of the Large Phase Shift of Terahertz Waves via Vanadium Dioxide Coupling Nanostructures, ACS Photonics. 5 (2018) 3040–3050. https://doi.org/10.1021/acsphotonics.8b00276.

[198] Z.-H. Zhai, H.-F. Zhu, Q. Shi, S.-C. Chen, J. Li, Z.-R. Li, H. Schneider, L.-G. Zhu, Enhanced photoresponses of an optically driven VO2-based terahertz wave modulator near percolation threshold, Applied Physics Letters. 113 (2018) 231104. https://doi.org/10.1063/1.5050681.

[199] A. Crunteanu-Stanescu, J.-C. Orlianges, A. Bessaudou, Fast optical activation of insulator-to-metal transition in vanadium dioxide (VO2) phase changed materials, in: F.H. Teherani, D.C. Look, D.J. Rogers (Eds.), Oxide-Based Materials and Devices XI, SPIE, San Francisco, United States, 2020: p. 53. https://doi.org/10.1117/12.2544767.

[200] N. Émond, A. Ibrahim, B. Torriss, A. Hendaoui, I. Al-Naib, T. Ozaki, M. Chaker, Impact of tungsten doping on the dynamics of the photo-induced insulator-metal phase transition in VO2 thin film investigated by optical pump-terahertz probe spectroscopy, Applied Physics Letters. 111 (2017) 092105. https://doi.org/10.1063/1.4995245.

[201] K. Dong, S. Hong, Y. Deng, H. Ma, J. Li, X. Wang, J. Yeo, L. Wang, S. Lou, K.B. Tom, K. Liu, Z. You, Y. Wei, C.P. Grigoropoulos, J. Yao, J. Wu, A Lithography-Free and Field-Programmable Photonic Metacanvas, Adv. Mater. 30 (2018) 1703878. https://doi.org/10.1002/adma.201703878.

[202] J. Lee, J. Kim, T. Kim, H. Sohn, Negative Differential Resistance Characteristics in Forming-Free NbO_x with Crystalline NbO_2 Phase, Phys. Status Solidi RRL. 15 (2021) 2000610. https://doi.org/10.1002/pssr.202000610.

[203] T. Joshi, T.R. Senty, P. Borisov, A.D. Bristow, D. Lederman, Preparation, characterization, and electrical properties of epitaxial NbO_2 thin film lateral devices, J. Phys. D: Appl. Phys. 48 (2015) 335308. https://doi.org/10.1088/0022-3727/48/33/335308.

[204] R. Waser, M. Aono, Nanoionics-based resistive switching memories, Nature Mater. 6 (2007) 833–840. https://doi.org/10.1038/nmat2023.

[205] A. Sawa, Resistive switching in transition metal oxides, Materials Today. 11 (2008) 28–36. https://doi.org/10.1016/S1369-7021(08)70119-6.

[206] M. Kang, S. Yu, J. Son, Voltage-induced insulator-to-metal transition of hydrogen-treated NbO_2 thin films, J. Phys. D: Appl. Phys. 48 (2015) 095301. https://doi.org/10.1088/0022-3727/48/9/095301.

[207] X. Liu, S.K. Nandi, D.K. Venkatachalam, K. Belay, S. Song, R.G. Elliman, Reduced Threshold Current in NbO_2 Selector by Engineering Device Structure, IEEE Electron Device Lett. 35 (2014) 1055–1057. https://doi.org/10.1109/LED.2014.2344105.

Appendices

Elaboration et corrélation structure/ propriétés optiques et électriques dematériaux oxydes à transition de phase (VO2, VO2 dopé avec W et NbO2)

Cette thèse vise la réalisation et la caractérisation structurale, optique et électrique de couches minces de matériaux oxydes ayant des propriétés de transition isolant-métal (MIT), plus particulièrement des oxydes de vanadium (VO_2 et VO_2 dopé avec W) et du dioxyde de niobium (NbO_2). Le dépôt de ces couches minces a été effectué par pulvérisation magnétron réactive dans une atmosphère Ar/ O_2. Le processus d'optimisation des films minces a permis d'obtenir des informations précieuses sur les effets du processus de fabrication sur les caractéristiques structurelles, optiques et électriques. En outre, les films ont été intégrés dans divers dispositifs tels que des modulateurs THz activés thermiquement/électriquement, des métacanvases reconfigurables optiquement et des dispositifs oscillants. Les informations fournies dans ce manuscrit sont d'un grand intérêt pour l'intégration de films de VO_2 et de VO_2 dopé avec W dans des dispositifs pouvant fonctionner dans différents domaines. Ce travail permet également d'approfondir notre compréhension des films de NbO_2, un domaine relativement moins étudié mais particulièrement intéressant pour les applications nécessitant une plus grande stabilité à la température.

Mots-clés : oxydes, dioxyde de vanadium, dioxyde de niobium, pulvérisation réactive, transition métal-isolant

Elaboration and correlation of structure/optical and electrical properties of phase transition oxide materials (VO_2, W-doped VO_2 and NbO_2)

This thesis aims at the realization and structural, optical, and electrical characterization of thin films of oxide materials with insulator-to-metal transition (MIT) properties, more specifically vanadium oxides (VO_2 and W-doped VO_2) and niobium dioxide (NbO_2). The deposition of these thin films was performed using reactive magnetron sputtering in an Ar/ O_2 atmosphere. During the optimization process of the thin films, valuable insights were gained into the effects the fabrication process has over the structural, optical and electrical characteristics. Furthermore, the films were integrated into various devices such as thermally/ electrically activated THz modulators, optically reconfigurable metacanvases and oscillating devices. The information provided in this manuscript is of high interest for the integration of VO_2 and W-doped VO_2 films into devices that can operate in various fields. This work also deepens our understanding of NbO_2 films, an area with comparatively less research but of particular interest for applications requiring higher temperature stability.

Keywords: oxides, vanadium dioxide, niobium dioxide, reactive sputtering, metal-to-insulator transition